Morphology, Magnetism and Superconductivity of Iron Layers on Niobium

Dissertation

zur Erlangung des Doktorgrades

des Department Physik

der Universität Hamburg

vorgelegt von

Julia Jirapon Goedecke

aus München

Hamburg

2023

Gutachter der Dissertation:	Prof. Dr. Roland Wiesendanger PD Dr. Jens Wiebe
Zusammensetzung der Prüfungskommission:	Prof. Dr. Roland Wiesendanger PD Dr. Jens Wiebe Prof. Dr. Michael Potthoff Prof. Dr. Michael Rübhausen Prof. Dr. Alexander Lichtenstein
Vorsitzender der Prüfungskommission:	Prof. Dr. Michael Potthoff
Datum der Disputation:	27.04.2023
Vorsitzender Fach-Promotionsausschuss PHYSIK:	Prof. Dr. Günter H. W. Sigl
Leiter des Fachbereichs PHYSIK:	Prof. Dr. Wolfgang J. Parak
Dekan der Fakultät MIN:	Prof. Dr.-Ing. Norbert Ritter

Zusammenfassung

Bei der Entwicklung von Quantencomputern werden derzeit topologische Quantensysteme als vielversprechende Kandidaten für die Realisierung von Qubits diskutiert. Diese Quantensysteme basieren insbesondere auf Majorana-Nullmoden, welche in Hybriden aus Festkörpern vorhergesagt werden, die BCS-artige Supraleitung mit Magnetismus und starker Spin-Bahnwechselwirkung oder chiralen Spinstrukturen kombinieren.

In dieser Arbeit werden solche physikalischen Systeme daraufhin untersucht, ob sie als Grundlage für topologische Quantencomputer dienen können und insbesondere ob sie für die Realisierung topologisch nicht-trivialer elektronischer Zustände, einschließlich Majorana-Nullmoden, geeignet sind.

Im ersten Teil dieser Arbeit wurde daher Niob(111) untersucht, da dessen Oberfläche eine vielversprechende grundlegende Plattform für die Realisierung von 2D-Magnet-Supraleiter-Hybridstrukturen darstellt. Nach der Aufbringung von magnetischem Material könnte die dreizählige Oberflächensymmetrie von Nb(111) zu magnetischer Frustration führen, welche die Ausbildung von chiralen Spinstrukturen wie Skyrmionen begünstigen könnte. Solche Systeme können theoretisch Majorana-Nullmoden beherbergen. Da für die Aufbringung von magnetischem Material auf Nb(111) die Oberfläche frei von Verunreinigungen sein sollte und es im Gegensatz zu Nb(110) noch kein etabliertes Verfahren zur Reinigung der Oberfläche gibt, wurde in dieser Arbeit zunächst eine Reinigungsmethode für die (111)-Oberfläche entwickelt. Anschließend konnte die atomare Struktur der sauberen Nb(111)-Oberfläche erstmals mit Hilfe der Rastertunnelmikroskopie (RTM) sichtbar gemacht und untersucht werden. Dabei zeigte sich eine Rekonstruktion, deren Auftreten theoretisch durch ein sogenanntes Vorschmelzen der Oberfläche erklärt werden kann.

Parallel zur Untersuchung von Nb(111) wurde auch mit der Präparation und Untersuchung von Nb(110) begonnen. Es zeigte sich dabei, dass sich die Nb(110) Oberfläche deutlich besser eignet, um darauf dünne Schichten magnetischen Materials wie Eisen aufzubringen, was der nächste Schritt zur Konstruktion eines topologischen Supraleiters wäre.

Im zweiten Teil dieser Arbeit wurde daher der Ansatz verfolgt, zweidimensionale Inseln, welche aus ein- bis zwei atomaren magnetischen Lagen bestehen auf der Oberfläche von Nb(110) zu präparieren (Shiba-Gitter). Nach der experimentellen Realisierung eines solchen Systems durch Eisenlagen auf Niob(110) konnte die atomare Struktur der drei gefundenen Rekonstruktionen aufgelöst werden. Außerdem wurde die elektronische und magnetische Struktur der verschiedenen Monolagen (ML) und der Doppellage (DL) mittels konventioneller und spinpolarisierter Rastertunnelmikroskopie bestimmt. Für die drei Typen von Rekonstruktionen wurden ferromagnetische Monodomänenstrukturen mit einer Magnetisierung senkrecht zur Ebene (out-of-plane) und unterschiedlichen Koerzitivfeldstärken gefunden, wobei die DL die gleiche Koerzitivfeldstärke wie die zugrunde liegende ML aufwies. Darüber hinaus wurden die sogenannten Shiba-Bänder, die für die künstliche Erzeugung von topologischen Supraleitern

essientiell sind, durch spektroskopische Messungen bei niedriger Energie untersucht.

Es zeigen sich Unordnungen in der ortsabhängigen und energetischen Lage der Shibabänder, welche energetisch in der Größenordnung der Substratlückenenergie liegen. Der Einfluss dieser Unordnungen auf die Ausbildung von Majorana-Moden wurde in dieser Arbeit untersucht, mit dem Ergebnis, dass höchstwahrscheinlich die Rekonstruktionen in diesem System die Ausbildung von topologischer Supraleitung und Majorana-Moden verhindern. Untersuchungen der Shiba-Bänder von DL-Eisen auf Niob(110) ergaben hingegen Anzeichen von Randzuständen in der Nähe der Fermi-Energie, wenngleich in dieser Arbeit nicht eindeutig geklärt werden konnte, ob es sich dabei um mögliche Hinweise auf topologische Supraleitung handelt oder nicht.

Zusammenfassend lässt sich sagen, dass diese Arbeit wesentliche Schritte für die Entwicklung eines künstlichen zwei-dimensionalen topologischen Supraleiters aufzeigt. Insbesondere wird dabei auch auf die Schwierigkeiten eingegangen, die bei diesem Entwicklungsprozess auftreten können. Die Ergebnisse zeigen aber auch eine Reihe von vielversprechenden Möglichkeiten für weitere Entwicklungen auf, die schließlich die Grundlage für zwei-dimensionale topologische Supraleitung mit Majorana-Nullmoden bilden könnten.

Abstract

Topological quantum systems, are currently being discussed as promising candidates for the realization of qubits in the development of quantum computers. In particular, these quantum systems are based on Majorana zero modes which are predicted in hybrids of solids that combine BCS-like superconductivity with magnetism and strong spin-orbit interaction or chiral spin structures.

In this work, such physical systems are investigated to evaluate whether they can serve as a basis for topological quantum computing and in particular, whether they are suitable for the realization of topologically nontrivial electronic states, including Majorana zero modes.

In the first part of this work, niobium(111) was investigated, as its surface provides a promising fundamental platform for the realization of 2D magnet-superconductor hybrid structures. After the deposition of magnetic material, the threefold surface symmetry of Nb(111) could lead to magnetic frustration, which could favor the formation of chiral spin structures such as skyrmions. Such systems could theoretically host Majorana zero modes. Since the surface should be free of impurities for the deposition of magnetic material on Nb(111) and, unlike Nb(110), there is still no established method for cleaning the surface, a cleaning method for the (111) surface was first developed in this work. Subsequently, using scanning tunneling microscopy (STM), the atomic structure of the clean Nb(111) surface could be visualized and studied for the first time. This revealed a reconstruction whose occurrence can be theoretically explained by a so-called premelting of the surface.

Parallel to the investigation of Nb(111), the preparation and investigation of Nb(110) was also started. It was found that the Nb(110) surface is much more suitable for depositing thin films of magnetic material such as iron on it, which would be the next step in the construction of a topological superconductor.

Therefore, in the second part of this work the approach was to deposit two-dimensional islands consisting of one to two atomic magnetic layers on the surface of Nb(110) (Shiba lattice). After the experimental realization of such a system by iron layers on niobium(110), the atomic structure of the three reconstructions that were found could be resolved. Moreover, the electronic and magnetic structure of the different monolayers (ML) and the double layer (DL) was determined by conventional and spin-polarized scanning tunneling microscopy. Ferromagnetic monodomain structures with out-of-plane magnetization and different coercive field strengths were found for the three types of reconstructions, with the DL exhibiting the same coercive field strength as the underlying ML. In addition, the so-called Shiba bands, which are essential for the artificial engineering of topological superconductors, were investigated by spectroscopic measurements at low energy. Disorder in the spacial and energetic locations of the Shiba bands were found, which are energetically of the order of the substrate gap energy. The influence of this disorder on the formation of Majorana modes has been investigated in this work, with the result that most likely the reconstructions in this system prevent

the formation of topological superconductivity and Majorana modes. Investigations of the Shiba bands of DL iron on niobium(110), on the other hand, revealed evidence of edge states near the Fermi energy, although this work did not fully clarify whether or not they may be regarded as an indication for topological superconductivity.

In summary, this work reveals essential measures for the development of an artificial two-dimensional topological superconductor. In particular, it also addresses the difficulties that can be encountered in this development process. However, the results also reveal a number of promising possibilities for further developments that could eventually form the basis for two-dimensional topological superconductivity with Majorana zero modes.

Contents

Chapter 1

Motivation and Introduction

Quantum computers are likely to be one of the next major world-changing technologies. In addition to the original motivation for quantum computing by Shor's algorithm for factoring large numbers [1, 2], a variety of promising application options have since emerged, such as in the development of artificial intelligence [3, 4] or medication [5, 6]. Another significant breakthrough that would be possible with the help of quantum computers is the simulation of quantum mechanical systems [7], as it would provide an enormous contribution to their understanding and thus to the development of technologies at the atomic level. However, even though more and more potential applications are now being imagined, the full extent of the potential associated with quantum computing is probably not yet foreseeable.

In order to perform computations, quantum computers are using such quantum mechanical phenomena as superpositions of quantum states, interference and entanglement [1, 2]. Most concepts of quantum computers are based on the quantum bit, or "qubit", analogous to the bit in classical computers. However, quantum bits can take on not only the classical values 0 and 1 during computational operations, but also a superposition of these. Nevertheless, when the value of a qubit is measured, it is always 0 or 1, with the probability of either outcome depending on the quantum state of the qubit immediately before the measurement.

Currently available quantum computers are based on relatively few qubits (of the order of a few hundred [8]), but scalability is not a major concern.

One of the main problems is that the qubits in current systems are extremely sensitive to perturbations, so they have to be isolated very well, which is increasingly problematic for large quantum systems. The problem of decoherence, i.e. the loss of superposition of a quantum state due to the influence of the environment, is here of particular importance and subject of current research. However, there are novel approaches to realize qubits using quantum states with topological properties that are significantly more robust and accordingly could solve the decoherence problem [9–12]. One of these approaches is based on the use of so-called Majorana bound-states or Majorana zero modes (MM), which are highly non-local quasiparticles with the property of being their own antiparticle, and which can therefore carry neither spin nor electric charge [13, 14]. These properties make them resistant to disturbances caused by local or global electric and magnetic fields.

Majorana bound states are not only interesting because of their protection against the perturbations mentioned above, but also because of their possible use for information processing, as there are predictions that Majorana states in 2D are anyons which obey non-Abelian statistics [15]. This means that if two Majorana states are locally exchanged (also known as braiding), a phase other than ±1 can be obtained. In fact, the exchange process (i.e. the specific geometry of the exchange path) is insensitive to the final state of the exchange of two Majoranas. Thus, the use of Majorana states implies that not only the qubit itself, but also the information processing itself is protected [13]. Therefore, topologically protected Majorana states seem to be perfect building blocks for qubits (and thus for quantum computers), as they are not affected by the local perturbations mentioned above and are consequently robust to decoherence effects.

However, such exotic Majorana states are not easily realized in solid state systems. Theoretical calculations have predicted Majorana states in topological superconductors [14, 16]. So far, however, topological superconductors have not been found in nature (although Sr_2RuO_4 is one promising candidate [17]). That is why experimental attempts are being made to realize topological superconductors artificially [18–27].
To do so, one can follow a recipe developed by theorists [13]: By proximity-coupling a semiconductor nanowire with large spin-orbit-coupling to a conventional s-wave superconductor, and additionally applying a magnetic field in an appropriate direction, one should obtain the desired artificial topological superconductor (see Sec. 2.4 for details). Rather than using a semiconductor nanowire and applying an external magnetic field, the wire can instead be constructed of magnetic atoms on a superconductor with strong spin-orbit coupling, which should automatically provide the required B field. The desired Majorana states should then appear as bound states at zero energy and are predicted to be located at the ends of the chain [10]. This concept can also be extended to two-dimensional magnetic islands, where one expects Majorana modes delocalized over the entire edge. In contrast to the one-dimensional chain, however, one can not only have a discrete state at $E = 0$, but DOS at energies close to zero [16, 28–30].
Those states should be detectable by the powerful scanning tunneling microscopy (STM) techniques, using low-energy spectroscopy measurements, which is the method of investigation in this work.
There are also other related approaches that eliminate the need for strong spin-orbit coupling and propose the use of noncollinear spin structures [31–33], in particular skyrmions [34–37] coupled to s-wave superconductors.

Huge efforts have already been made to realize Majorana states on different platforms including (quasi) 1D [18–24] and 2D [25–27, 38] systems. However, the experimental evidence for the existence of Majorana states is still very controversial [39–42].

Motivated to continue the work on this interesting topic, this thesis, in the first main part of Chapter 4, is devoted to the exploration of a new substrate, namely Nb(111) that could serve for the preparation of new Majorana platforms.
Niobium is a natural choice for the construction of a topological superconductor, since elemental niobium becomes conventionally BCS-superconducting at a relatively high temperature of 9.2 K and has the largest energy gap of all elemental superconductors. Moreover, although Nb is a comparatively light element, it has been shown to provide sufficiently strong spin-orbit coupling to support the emergence of p-wave gaps in 1D magnetic wires [43, 44]. While Nb(110) with its twofold symmetry has already provided promising experimental results as a substrate for the realization of magnetic 1D chains [45], Nb(111) could prove particularly useful for the realization of 2D magnetic structures. This is due to the threefold surface symmetry of Nb(111), which (after the

deposition of magnetic material) could favor the formation of chiral spin structures such as skyrmions, which in turn could theoretically host Majorana zero modes. However, niobium surfaces are usually contaminated with oxygen, and unlike Nb(110), there is still no established method for cleaning the surface of Nb(111). Therefore, a method for cleaning the (111) surface was first developed in this work, and the clean surface was then subsequently investigated using scanning tunneling microscopy, as described in Sec. 4.1.

In the second part of this work, the focus lies entirely on thin iron layers deposited on Nb(110) (denoted in the following as Fe/Nb(110)). In this system, all pre-requirements for topological superconductivity seem to be fulfilled, i.e. a spin-orbit-coupled substrate with *s*-wave SC [43] which is proximitized to ferromagnetic Fe layers leading to Shiba-band formation.
In Sec. 4.2 and Sec. 4.3, the growth and structure of the Fe layers on Nb(110) will be investigated, followed by the determination of their magnetic properties in Sec. 4.4, which is essential for further investigation. In Sec. 4.5, the Shiba bands are investigated, which are necessary to realize Majorana states. At the very end of Chapter 4, interesting insights into the DL of Fe/Nb(110) are given and the findings are discussed. In Chapter 5, after a summary of the results, an outlook is given, concluding this work.

Chapter 2

Theoretical Background

In this chapter we will explore the theoretical background for this thesis. This is done by describing the principle of a scanning tunneling microscope and the underlying theory in Sec. 2.1. Subsequently, in Sec. 2.2, we will discuss the magnetism of thin films, the superconductivity in Sec. 2.3, while the merging of both topics leads to the Sec. 2.4

2.1 Scanning Tunneling Microscopy

In this section, we will focus on the description of a scanning tunneling microscope (STM) which can be considered to belong to the category of scanning probe microscopes.

Scanning probe microscopy is a powerful tool for the examination of surfaces. There are various types of scanning probe microscopy methods that can be used to investigate different properties of a surface, such as its electronic, topographic, or magnetic properties, depending on the probes used and the associated measurement principles. The underlying concept is quite simple to explain: A probe tip raster-scans a surface line by line and measures the interaction between probe and surface. Once the measured interactions are then combined line by line, an image of the surface is created, which represents the measured interactions. To name just two examples: In atomic force microscopy (AFM) [46], the probe is a tip mounted on a spring and its deflection due to force interactions can be measured. This can be used to study non-conductive surfaces. Then there is scanning near-field optical microscopy (SNOM) [47] in which, as the name implies, optical methods are used to study the surface. There are many others, but in the following we will discuss the scanning tunneling microscope that has been used for the measurements in this work and which is still one of the methods with the best resolution in real space.

Scanning tunneling microscopy was invented in the 1980s by G. Binnig and H. Rohrer [48], for which both were awarded the Nobel Prize in 1986. A sketch of an STM is shown in Fig. 2.1. Here the probe, a sharp conductive (ideally atomically sharp) tip, scans a conductive sample surface. As shown in Fig. 2.1 **a**, the tip is mounted at the bottom of a tube scanner which can bend in the x-y direction by applying a voltage to the piezoelectric elements on the sides (p_x, p_y), and can expand or contract in the z-direction by the piezoelectric element p_z inside the tube scanner. The sample shown in gray in Fig. 2.1 is located directly above or below the tip, depending on the setup, with the distance s between the tip and the surface being only a few Å. As a result of this, the wave functions of the electrons of the tip and sample can overlap, allowing

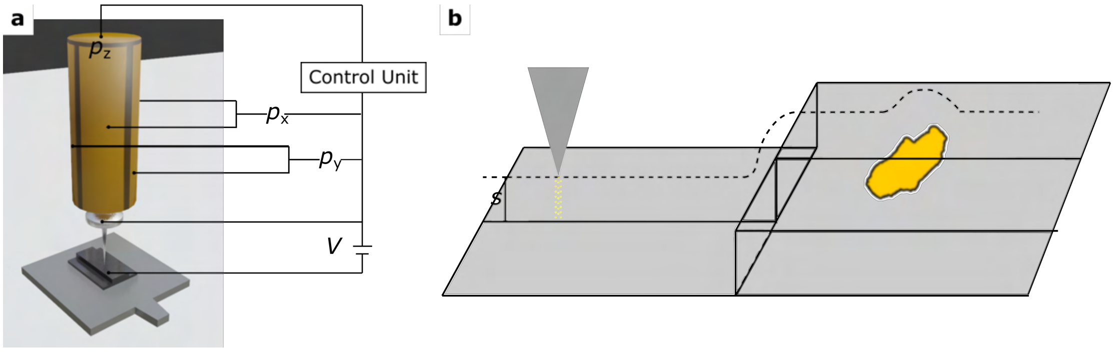

Figure 2.1: In **a** the schematic representation of an STM is shown with a tube scanner and the piezoelectric elements p_x and p_y on the sides, while p_z can be seen inside the tube. Furthermore, a tip is attached at the bottom of the tube scanner. A voltage V is applied between the tip and the sample to allow tunneling of electrons. The control unit controls the constant tip height via an appropriate voltage adjustment on the piezo's z-electrode, while the tip moves along the dashed line shown in the schematic sketch in **b**. The principle of the STM is described in detail in the main text.

electrons to tunnel from the tip to the sample or vice versa (see Sec. 2.1.1 and Fig. 2.1 **b**). Usually, a net current I is then measured by applying a voltage V between the tip and the sample. Due to the rather small tunnel current (a few hundred pA up to a few nA), which depends exponentially on the distance s, it is amplified by a current-to-voltage amplifier. This voltage is passed on to a control unit, which compares these values with a reference value and by using an appropriate voltage adjustment on the piezo's z-electrode so that the tunnel current and thus also the distance between the sample and tip are kept constant (constant current mode). The topography of the surface can therefore be extracted from the vertical change in position of the tip (Fig. 2.1 **b**). However, the recorded signal is a convolution of the electronic structure of the tip and the sample and therefore the image cannot be taken as a pure topographic image of the sample surface. In STM, the "constant height" mode can also be selected to scan the surface. Here, as the name suggests, the tip is fixed at a constant height during scanning. However, this mode carries the risk of the tip hitting irregularities and is usable only when the surface to be scanned is known beforehand.

In addition to imaging, the STM can also be used for spectroscopic measurements by changing the bias voltage during the measurement. This is described in more detail in section 2.1.3. Furthermore, there are many variants of scanning tunneling microscopy. Of particular importance is spin-polarized scanning tunneling microscopy (SP-STM) [49] (see Sec. 2.1.4), where insights into magnetism and spin structures at the nanoscale can be obtained by combining the atomic resolution of an STM with spin-sensitive measurements.

2.1.1 Tunneling Process (1D)

The tunneling process is a quantum mechanical phenomenon that cannot be described classically. If an electron hits a potential barrier, it would be reflected classically if its energy E is smaller than that of the potential barrier V_0. However, since electrons have such a small mass, there is a probability that an electron hitting the potential barrier can penetrate or cross it. This effect is called *tunneling process* [50]. If we consider an electron propagating from the left to the potential barrier (see Fig. 2.2), its wave function ψ must satisfy the following time-independent Schrödinger equation [50, 51]:

$$-\frac{\hbar^2}{2m}\frac{d^2}{dz^2}\psi(z) + V(z)\psi(z) = E\psi(z), \tag{2.1}$$

with the mass m of an electron and $\hbar$, the Planck constant divided by 2π.

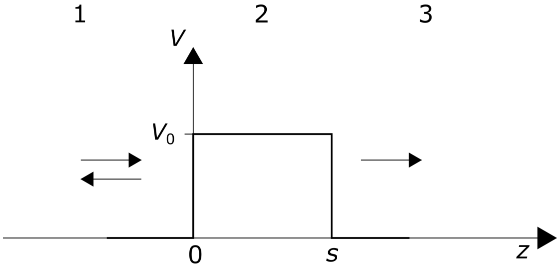

Figure 2.2: One-dimensional tunneling barrier with a rectangular potential V_0 of width s. Here three areas for the different ansatz of the wave functions can be distinguished. The lateral axis indicates the distance z and the vertical axis indicates the potential.

According to Fig. 2.2, three regions ($z < 0$, $0 \leq z \leq s$, and $z > s$) in which a different ansatz for the wave function has to be considered can be distinguished. For the range $z < 0$ the wave function ψ_1 is given by

$$\psi_1 = e^{ikz} + Ae^{-ikz}, \tag{2.2}$$

where the amplitudes of the incoming and reflected waves are normalized to 1 and A, respectively.
In the range $0 \leq z \leq s$, i.e., within the potential barrier, the wave function ψ_2 is

$$\psi_2 = Be^{\kappa z} + Ce^{-\kappa z}, \tag{2.3}$$

with B being the amplitude of the wave propagating to the right and C the amplitude of the reflected wave.
Finally, in the last section, $z > s$, the transmitted wave function with amplitude D is

$$\psi_3 = De^{ikz}. \tag{2.4}$$

Solving the Schrödinger equation (2.1) with the ansatz given by the equations Eq. (2.2)-(2.4), one obtains $k^2 = \frac{2mE}{\hbar^2}$ and $\kappa^2 = \frac{2m(V_0-E)}{\hbar^2}$. Hence, it is now possible to determine the transmission coefficient, which is the ratio between the transmitted and incident current density

$$T = \frac{I_t}{I_i} = \frac{|D|^2}{|1|^2} = \left[1 + \left(\frac{k^2+\kappa^2}{2k\kappa}\right)^2 \sinh^2(\kappa s)\right]^{-1}. \tag{2.5}$$

This equation describes the probability that an electron will cross the potential barrier it encounters. Assuming a very high and wide barrier, i.e. $\kappa s >> 1$, and thus $\sinh(2\kappa s) \cong \frac{1}{2}e^{2\kappa s} >> 1$, equation (2.5) can be simplified to

$$T \propto e^{-4\sqrt{2m(V_0-E)}\,\frac{s}{\hbar}}. \tag{2.6}$$

The exponential decrease of the transmission probability with the width s of the potential barrier becomes clear from equation (2.6).

2.1.2 Bardeen's Theory of Tunneling and the Tersoff-Hamann Model

In 1960 Bardeen [52] extended the theory of the tunneling process described in section 2.1.1. For this purpose, he calculated the tunneling current of a system consisting of two planar electrodes A and B and included the electronic structure of the electrodes in the calculation.

To do so, he divided the system into two subsystems and solved the stationary Schrödinger equation for each of them. Thus the linear combination [50] Ψ,

$$\Psi = \psi_\mu e^{-\frac{iE_\mu t}{\hbar}} + \sum_{\nu=1}^{\infty} c_\nu(t)\psi_\nu e^{-\frac{iE_\nu t}{\hbar}}, \tag{2.7}$$

of the individual solutions ψ_μ and ψ_ν with the eigenenergies E_ν (E_μ), respectively, of ψ_ν (ψ_μ) with the coefficient c_ν to be determined, is then used as an ansatz for the time-dependent Schrödinger equation of the combined system,

$$i\hbar\frac{\partial\Psi}{\partial t} = \left[-\frac{\hbar^2}{2m}\frac{\partial^2}{\partial z^2} + V_\mathrm{A} + V_\mathrm{B}\right]\Psi. \tag{2.8}$$

Here, V_A and V_B denote the potential of the electrodes A and B, respectively. Solving equation (2.8), the quadratic modulus of the coefficient $c_\nu(t)$ yields

$$|c_\nu(t)|^2 = \frac{2\pi}{\hbar}|M_{\nu\mu}|^2\,\delta\left(E_\mu - E_\nu\right), \tag{2.9}$$

which gives the probability that an electron tunnels from the μth state (electrode A) to the νth state (electrode B) at time t. $M_{\nu\mu}$ is the so-called *tunnel matrix element*

$$M_{\nu\mu} = -\frac{\hbar^2}{2m}\int dS\left(\psi_\mu^*\,\Delta\psi_\nu - \psi_\nu\Delta\psi_\mu^*\right) \tag{2.10}$$

and can only be solved knowing the explicit wavefunctions ψ_ν and ψ_μ of the electrodes, where the integral over the entire surface of electrode B must be evaluated. The delta function δ in equation (2.9) ensures energy conservation ($E_\nu = E_\mu$), i.e., electrons in this model can tunnel only between states of the same energy, known as elastic tunneling.

So far, only the tunneling probability of single states μ and ν has been considered. In fact, however, each of them contains a whole spectrum of states which have to be considered. The Fermi distribution $f(E_\mu)$ gives the probability that the state μ in electrode A is occupied. It is clear that electrons can only tunnel from an occupied state to an unoccupied state. The probability that the state μ in electrode A is occupied while the state ν in electrode B is unoccupied is given by $f(E_\mu)(1 - f(E_\nu + eV))$ for an applied voltage V (where e is the elementary charge). Considering also the case where electrons can tunnel from the occupied state ν of electrode B to the unoccupied state μ of electrode A, and summing over all possible states, one obtains the following equation for the net tunneling current [53]:

$$I = \frac{2\pi e}{\hbar}\sum_{\mu\nu}\left\{f(E_\mu)[1 - f(E_\nu + eV)] - f(E_\nu + eV)\,[1 - f(E_\mu)]\right\}|M_{\mu\nu}|^2\,\delta(E_\nu - E_\mu). \tag{2.11}$$

Tersoff and Hamann [54] applied Bardeen's theory to a system consisting of a planar electrode and an electrode of spherical geometry, which describes an STM experiment

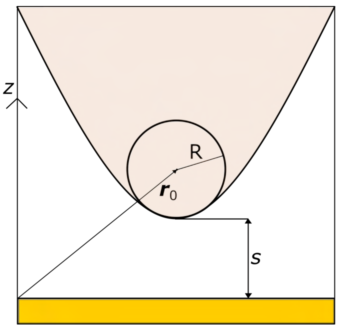

Figure 2.3: Tersoff-Hamann model of the tip.

in a better way. Thus, they made an s-wave function approach of the type $\psi_\mu = \frac{1}{R}\, e^{-\kappa R}$ for the tip. Fig. 2.3 shows the assumed geometry for their calculations. Here R is the effective radius of the tip, $\boldsymbol{r}_0$ is the vector pointing to the center of the curvature of the tip and s is the distance between tip and sample. Assuming low temperatures ($T \leq T_{\mathrm{RT}}$)[1] and low voltages ($\sim$ 10 meV) (implying that only electrons in the vicinity of the Fermi energy are involved in the tunneling process, this requirement will be later lifted), the expression for the current from equation (2.11) can be simplified to

$$I \propto V \rho_{\mathrm{t}}(E_{\mathrm{F}}) \rho_{\mathrm{s}}\left(E_{\mathrm{F}}, \boldsymbol{r}_0\right). \tag{2.12}$$

Here, $\rho_{\mathrm{t}}(E_{\mathrm{F}})$ is the density of states (DOS) at the Fermi level of the tip and $\rho_{\mathrm{s}}\left(E_{\mathrm{F}}, \boldsymbol{r}_0\right)$ is the local density of states (LDOS), evaluated at the point $\boldsymbol{r}_0$

$$\rho_{\mathrm{s}}\left(E_{\mathrm{F}}, \boldsymbol{r}_0\right) = \sum_\nu \left|\psi_\nu(\boldsymbol{r}_0)\right|^2 \delta\left(E_\nu - E_{\mathrm{F}}\right). \tag{2.13}$$

An exponential decay in the z-direction is assumed for the sample wave function ψ_ν, i.e. $|\Psi_\nu(\boldsymbol{r})| \propto e^{-\kappa z}$.
Based on this model and equation (2.12), STM images taken at low voltages and constant tunneling current can be interpreted as maps of constant contours of the local density of states at the Fermi energy evaluated at the point $\boldsymbol{r}_0$.

For higher voltages the model has to be extended. Most generally, it can result in a change/disturbance of the states ψ_μ and ψ_ν as well as their respective eigenenergies E_μ and E_ν. This would lead to very complicated calculations, so usually only a shift of the energy of the unperturbed states by the amount eV is assumed. However, for tunnel voltages in the range up to 1 eV and metallic tips and samples, these perturbations are usually negligible. Then, a generalization of the equation (2.12) gives [50, 51, 55]

$$I \propto \int^{eV} \rho_{\mathrm{t}}(\pm eV \mp E)\ \rho_{\mathrm{s}}(E, \boldsymbol{r}_0)\ T(E, eV)\ dE, \tag{2.14}$$

with energies given relative to the Fermi energy. The upper signs correspond to positive sample bias and the lower signs to negative sample bias. The transmission coefficient T is given by [51, 55]

$$T(E, eV) = \exp\left\{-2(s+R)\left[\frac{2m}{\hbar^2}\left(\frac{\phi_{\mathrm{t}} + \phi_{\mathrm{s}}}{2} + \frac{eV}{2} - E\right)\right]^{\frac{1}{2}}\right\}. \tag{2.15}$$

---

[1] RT = room temperature.

It should be noted (compared to equation (2.6)) that the transmission coefficient T now takes into account the applied voltage V as well as the work function of the tip ϕ_t and the sample ϕ_s, which describe the material-specific energy required for an electron with the Fermi energy to leave the material and enter the vacuum.

2.1.3 Scanning Tunneling Spectroscopy

When a positive voltage is applied according to equation (2.14), electrons tunnel from occupied states of the tip to unoccupied states of the sample and vice versa for negative voltage. It is possible to select the electronic states that mostly contribute to the tunneling current by varying the applied voltage. For example, the tunneling current increases sharply when the applied voltage allows the electrons to tunnel to the next higher unoccupied energy state. This makes it possible, in principle, to measure the local electronic density of states.
Therefore, to a first approximation, the LDOS can be measured by the *differential conductance* $\mathrm{d}I/\mathrm{d}V$, which is obtained by the following equation [2], assuming that the density of states of the tip is constant [50, 51, 55]

$$\frac{dI}{dV}\left(V,\boldsymbol{r}_0\right) \propto e\rho_\mathrm{t}\left(0\right)\rho_\mathrm{s}\left(eV,\boldsymbol{r}_0\right)T\left(eV,eV\right) + \int_0^{eV}\rho_\mathrm{t}\left(\pm eV \mp E\right)\rho_\mathrm{s}\left(E\right)\frac{dT(E,eV)}{dV}dE. \tag{2.16}$$

Such spectroscopy measurement is performed in the experiment by positioning the tip above the point to be measured (point spectroscopy) and fixing it at a certain height by switching off the feedback loop. Next, a high frequency, low amplitude additional sinusoidal voltage modulation is applied to the bias voltage V between the tip and the sample. In this way, the change of the tunnel current with the modulated voltage is measured while the bias voltage is swept through a certain interval.
Since point spectroscopy provides an approximately continuous spectrum, the resonances of the LDOS can ideally be read directly from the graphs with energies corresponding to those of the electronic states.

Besides point spectroscopy, also spatially resolved spectroscopy, so-called $\mathrm{d}I/\mathrm{d}V$ maps, can be obtained. Again, an additional voltage modulation with a frequency f is applied, however with a constant bias voltage. In this mode, the feedback loop is switched on, but the frequency of the modulation is significantly higher than the cutoff frequency of the feedback loop, which means that the tip and thus the tunnelling current is not following this high-frequency modulation. Thus, one nevertheless receives images where the dc-tunneling current remains constant and therefore a spatially resolved spectroscopic image can be measured simultaneously with the topography.
It should be noted that the interpretation of the images with spatially resolved spectroscopy ($\mathrm{d}I/\mathrm{d}V$ maps) is not that trivial. At constant tunnel current and thus constant distance between tip and sample, the voltage dependence of the transmission coefficient is only small (and only slightly monotonically increasing with increasing voltage), so that the effect of LDOS dominates. However, if there is a laterally changing LDOS, this has also an effect on the current and on the stabilization distance between tip and sample. Thereby, the LDOS changes, which we would like to measure, could be partially suppressed or enhanced in a $\mathrm{d}I/\mathrm{d}V$ map.
To interpret the $\mathrm{d}I/\mathrm{d}V$ data as a function of location (x, y), one can consider an analogous experiment for measuring the local tunnel barrier height ϕ. If one modulates the

---

[2] The upper signs correspond to positive sample bias and the lower signs to negative sample bias.

tip distance s between sample and tip by a small value Δs so fast that the feedback loop cannot readjust, a tunnel current with a small modulation in phase with the modulation of Δs is obtained. A topography image can then be obtained from the measured data and a map for the change in tunnel current can be calculated using the distance modulation Δs [51]

$$\frac{\Delta \ln(I)}{\Delta s} = -\frac{2(2m)^{1/2}}{\hbar}\phi^{1/2}. \tag{2.17}$$

Now, keeping in mind that at atomic resolution the apparent barrier height of a local topographic protrusion is larger than the apparent barrier height of a local topographic depression (which can be easily made plausible by considering the frequencies of the electron states), then by equation (2.17) it is evident that the contrast of the map is inverted by the negative proportionality to the apparent barrier height.

Like the measurement of local tunnel barrier height, $\mathrm{d}I/\mathrm{d}V$ maps show the effect of inversion of topography, as the apparent barrier height of a local topographic protrusion is larger than the apparent barrier height of a local topographic depression. Therefore, the spatial variations of the $\mathrm{d}I/\mathrm{d}V$ maps in constant current mode actually contain a superposition of the topography and the electronic structure of the sample, as can also be seen from equation (2.16).

2.1.4 Spin-Polarized Scanning Tunneling Microscopy

According to the Stoner Model [56], which is briefly discussed in Sec. 2.2.3, magnetic materials exhibit spontaneous spin splitting of the density of states. To be more specific, this means that in 3d materials that fulfill the Stonder criterion the bands are spin-dependently split into energetically favorable electron bands (which host the majority of the electrons, i.e. majority electrons) and energetically less favorable electron bands (minority electrons). In spin-polarized scanning tunneling microscopy (SP-STM), this property is exploited, thus empowering the STM to detect magnetic properties of the sample. The principle will be briefly explained with reference to Fig. 2.4, assuming no spin flip: Tip and sample are magnetic and have a spin-split DOS. If both have the same magnetization direction, i.e. are aligned parallel relative to each other, many spin down electrons can tunnel to free spin down states of the sample. This is indicated in Fig. 2.4 **a**. If the magnetization of the sample is now flipped, i.e. one assumes an antiparallel configuration relative to the tip, only a few spin down states of the sample are available as final states after tunneling of the many spin down electrons at the Fermi edge of the tip. In summary, this means that a larger tunnel current I_p flows in the left scenario (see Fig. 2.4 **a**) than in the right scenario (see Fig. 2.4 **b**).

In addition to the previously described polarized spin current I_p, the total current I detected by the STM naturally also contains an unpolarized contribution I_0 ($I = I_0 + I_\mathrm{p}$), which can dominate the total current. Thus, in order to obtain a strong contrast in the images through spin-polarization P (see Eq. (2.20) for the definition), differential conductance measurements have proven to be beneficial, where the voltage can be chosen such that there is an overlap of strongly spin-polarized DOSs of tip and sample [57]. The differential conductance is given by:

$$\frac{\mathrm{d}I}{\mathrm{d}V}(\mathbf{r}_0, V) \propto \rho_\mathrm{t}\rho_\mathrm{s}(\mathbf{r}_0, E_\mathrm{F} + eV) + \mathbf{M}_\mathrm{t}\mathbf{M}_\mathrm{s}(\mathbf{r}_0, E_\mathrm{F} + eV), \tag{2.18}$$

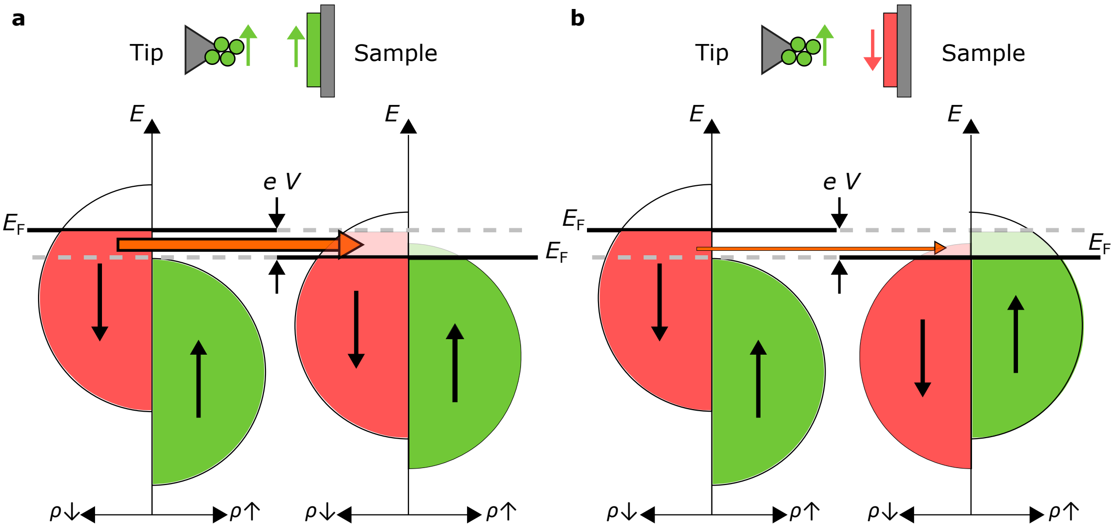

Figure 2.4: Illustration of the principle of SP-STM for a parallel **a** and antiparallel **b** alignment of tip and sample. Schematically, the spin-dependent DOSs are plotted against the energy of tip and sample. For simplicity, it is assumed that the tip DOS is fully spin-polarized in the energy range around the Fermi energy which is relevant for tunneling. The description of the process can be found in the main text.

where $\mathbf{r}_0$ is the position of the tip, $\mathbf{M}_\mathrm{t}$ ($\mathbf{M}_\mathrm{s}$) is the magnetization of the tip (sample) with $\mathbf{M} = (\rho_\uparrow - \rho_\downarrow)\,\mathbf{e}_\mathrm{M}$ where $\mathbf{e}_\mathrm{M}$ denotes the unit vector of magnetization. Relation (2.18) can be simplified to

$$\frac{\mathrm{d}I}{\mathrm{d}V} \propto \rho_\mathrm{t}(E_\mathrm{F})\rho_\mathrm{s}(E_\mathrm{F}+eV,\mathbf{r}_0)(1 + P_\mathrm{t}(E_\mathrm{F})P_\mathrm{s}(E_\mathrm{F}+eV,\mathbf{r}_0)\cos(\theta)), \qquad (2.19)$$

with θ the angle between the magnetization direction of the tip and the sample (at position of the tip). The spin polarization P is defined as

$$P = \frac{\rho_\uparrow - \rho_\downarrow}{\rho_\uparrow + \rho_\downarrow}. \qquad (2.20)$$

It should be noted that depending on the situation, i.e. whether $\rho_\uparrow > \rho_\downarrow$ or $\rho_\uparrow < \rho_\downarrow$ is true, the spin polarization P can be positive or negative, respectively. So, in principle, SP-STM is based on the tunnel magnetoresistance (TMR) effect which describes a similar system, namely the tunneling between two magnetic electrodes through a medium. TMR was first discovered and practically realized by M. Jullière in 1975 using Fe/Ge-O/Co contacts at 4.2 K [58]. In 1990, the TMR effect was successfully transferred to STM for the first time by R. Wiesendanger, whose work revealed the predicted antiferromagnetic properties of Cr(001) [59].

2.1.5 Superconductor-Superconductor Tunneling

For spin-averaged measurements in the low-energy regime, a pure Nb bulk tip has been used because it increases the energy resolution at higher temperatures beyond the Fermi-Dirac limit [24, 60]. Therefore, tunneling between superconductors is briefly outlined in this section.

The tunnel current between two superconductors with a potential barrier is given by [61]

$$I_{ss} = \frac{G_{nn}}{e} \int_{-\infty}^{\infty} \frac{|E|}{\sqrt{E^2 - \Delta_1^2}} \frac{|E + eV|}{\sqrt{(E + eV)^2 - \Delta_2^2}} \left[f(E) - f(e + eV) \right] dE, \tag{2.21}$$

where the conductance of tunneling between normal metals is G_{nn}. The I/V curves, e.g., follow from numerical integration.

The tunneling process is shown schematically in Fig. 2.5[3]. For $T = 0\,\mathrm{K}$ the states are fully occupied up to the gap, while for the case $T > 0\,\mathrm{K}$ the occupation probability is given by the Fermi function [61]. Sketched are tunneling processes at different voltages, where a smaller pairing potential Δ_t is assumed for the tip (left) relative to the sample Δ_s (right) ($\Delta_\mathrm{t} < \Delta_\mathrm{s}$). If the sample and the tip are at the same potential level ($V = 0$, Fig. 2.5 **a**), electrons can tunnel from occupied states of the tip into a few unoccupied states of the sample due to the temperature-dependent Fermi distribution. However, electrons from the low occupied states of the sample can also tunnel into the unoccupied states of the tip, so that no net current flows (see Fig. 2.5 **a**).

In Fig. 2.5 **b** the case $eV = \Delta_\mathrm{s} - \Delta_\mathrm{t}$ is shown. Now, the thermally occupied electrons at the coherence peak of the tip can tunnel into the large unoccupied density of states at the coherence peak of the sample resulting in a peak in $\mathrm{d}I/\mathrm{d}V$.

Fig. 2.5 **c** shows the case $eV = \Delta_\mathrm{s} + \Delta_\mathrm{t}$, where the almost fully occupied states at the negative-energy coherence peak of the tip can tunnel into the almost empty states at the positive-energy coherence peak of the sample, which leads to a strong current increase and a strong peak in $\mathrm{d}I/\mathrm{d}V$. The described behavior of the superconductor-superconductor-tunneling processes is also found in the characteristic $I - V$ and $\mathrm{d}I/\mathrm{d}V$ curves, which are seen in Fig. 2.5 **d**. For the experimental measurements it should be kept in mind that due to the additional tip-gap all features in the $\mathrm{d}I/\mathrm{d}V$ curve stemming from sample states are shifted by Δ_t relative to their energies in the sample's DOS. This means that sample states at $E_\mathrm{F} = 0$ are found at Δ_t.

---

[3] It should be noted that this model was derived from a single-particle picture and is not suitable if Cooper pairs play a role in the tunneling process (see the Josephson effect for this [62, 63]).

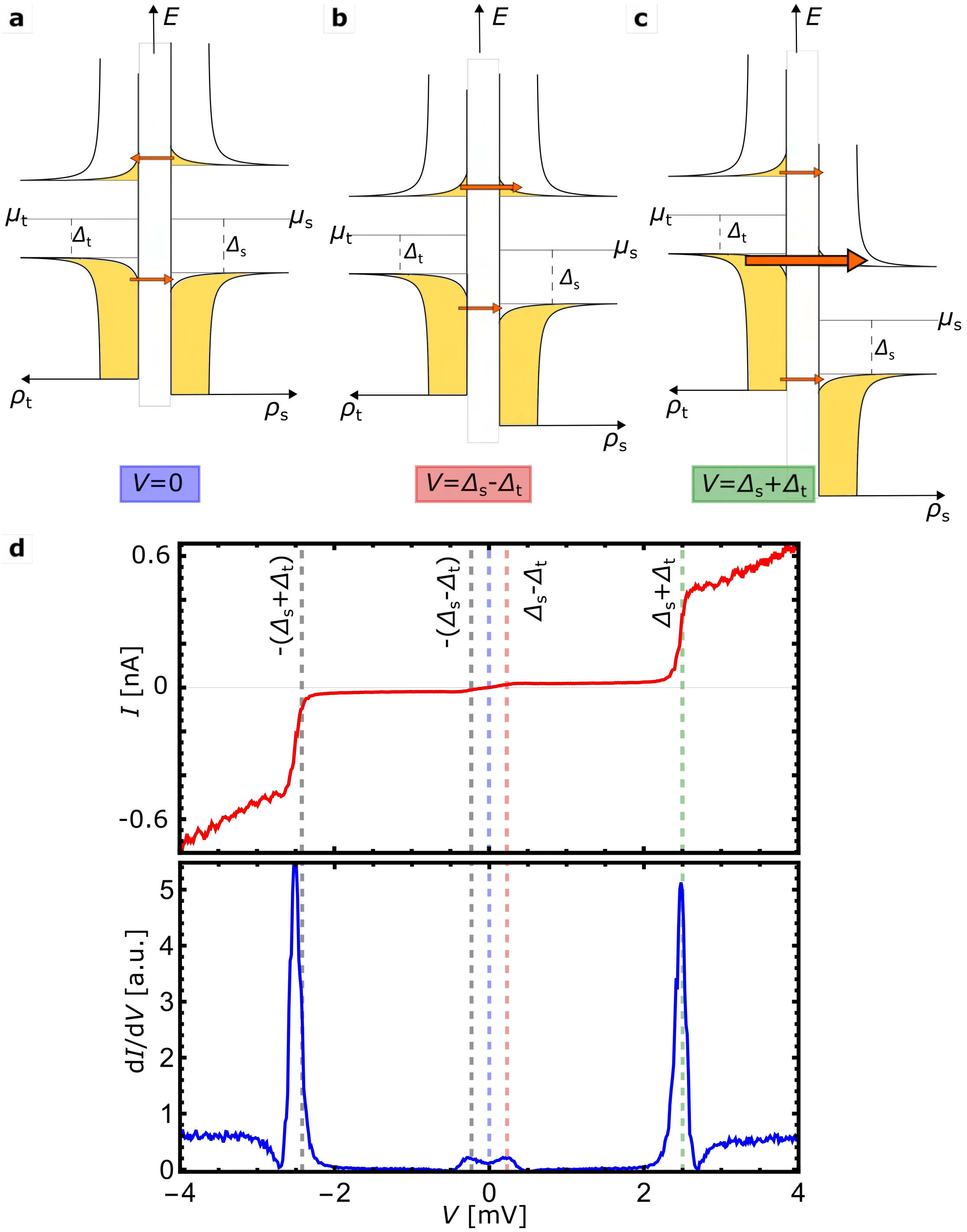

Figure 2.5: Sketches of the tunneling processes between superconductors at different voltages can be seen in **a**-**c**. The DOS-dependence on the energy of the superconductor is described by Eq. (2.53) [61]. For the description of the individual images see main text. In **d** a typical I-V and $\mathrm{d}I/\mathrm{d}V$ curve of the tunneling process can be seen. Measurement parameters: $I_{\mathrm{stab}} = 400\,\mathrm{pA}$, $V_{\mathrm{stab}} = 4\,\mathrm{mV}$, $V_{\mathrm{mod}} = 0.1\,\mathrm{mV}$, $f = 1197\,\mathrm{Hz}$ and $T = 4.5\,\mathrm{K}$.

2.2 Magnetism in Solids

The central quantities for the characterization of the magnetic properties of solids are the magnetic moment $\mathbf{m}$, the magnetization $\mathbf{M}$ and the susceptibility χ, which are provided by the Maxwell equations and the material equation [64, p. 7]. Based on the susceptibility χ, which is a real number that describes the response of a system to an external B-field [64, p. 17], magnetism can be roughly divided into three classes: **diamagnetism**, **paramagnetism** and **collective magnetism**.

In diamagnetism, magnetic moments are induced by an external magnetic field, which are aligned in the opposite direction to the external B-field (due to Lenz's law). In this case, the susceptibility $\chi_{\text{dia}} < 0$ is negative and independent of the temperature.

In paramagnetism, permanent magnetic moments already exist (which is why usually paramagnetism is several orders of magnitude stronger than diamagnetism) and align themselves along an external B-field, but thermal motion hinders the alignment. Thus, when the external B-field is switched off, the overall magnetization is destroyed due to the thermal motion, so that no magnetic preferred direction can be found anymore. The susceptibility for paramagnetism is positive $\chi_{\text{para}} > 0$.

Collective magnetism includes ferro-, ferri-, and antiferromagnetism and more complex spin-orders like spin-spirals or skyrmion lattices. Here, the susceptibility is a complicated function $\chi_{\text{C}}(T, \mathbf{B}, \text{"}\textit{pretreatment}\text{"})$ and positive for ferromagnetism. As in paramagnetism, there are permanent magnetic moments that interact directly or indirectly with each other. Due to this so-called **exchange interaction** the magnetic moments, even without an external B-field below a critical temperature T_c, exhibit spontaneous magnetization, as long as the so-called Stoner criterion (see Sec. 2.2.3) is fulfilled.

Magnetism in solids is therefore a many-particle problem, which so far can only be solved for limiting cases. Especially, for ferromagnetism, one divides systems into strongly localized or quasi-free permanent magnetic moments. When the permanent magnetic moments are strongly localized, i.e., there is no overlap of their wave function, the **indirect interaction** (e.g., by exchange with the conduction electrons or interaction through a substrate) is of central importance and is responsible for the magnetism. In the case of non-localized permanent magnetic moments, i.e., when the conduction electrons simultaneously represent the permanent magnetic moments (as is the case for Fe, Co and Ni), we speak of **band magnetism** and the **direct exchange interaction** plays a central role. The **Hubbard model** [65] is the standard model to describe band magnetism.

In the next sections we will briefly describe the Hubbard model, and based on it, the Stoner approach (Sec. 2.2.3), which is important for understanding ferromagnetism in bulk materials. Afterwards, we will come to the description of micromagnetism and explain the energy terms that are important for thin film magnetism (Sec. 2.2.4).

2.2.1 Spin-orbit Coupling

Spin-orbit coupling describes the coupling of the electron spin to the orbital motion in the nuclear field. The heavier the nucleus, the stronger the resulting field generated by the nucleus, which is "felt" by the electron. Accordingly, spin-orbit coupling usually gets stronger for heavier nuclei. The Hamiltonian for atomic spin-orbit coupling is [64, p. 44]:

$$H_{\text{SO}} = \lambda \mathbf{L} \cdot \mathbf{S}, \tag{2.22}$$

with the orbital angular momentum operator **L** and the spin operator **S** (see appendix A.1) and the constant

$$\lambda = \frac{1}{8\pi\epsilon_0 m^2 c^2} \cdot \frac{Ze^2}{r^3}. \tag{2.23}$$

Note that λ is proportional to the atomic number Z, where ϵ_0 is the electric field constant and c is the speed of light. Moreover, the spin-orbit coupling strongly decreases with nuclear distance (r^{-3}). Spin-orbit coupling also degenerates the multiplet (see appendix A.1). It should also be noted, that the spin-orbit coupling experienced by the conduction electrons in a solid can strongly deviate from the atomic one given by Eq(2.22) and (2.23). In particular due to inversion symmetry breaking at every surface, the electrons additionally feel the so-called surface electric field, which additionally contributes to spin-obit coupling giving rise to the so-called Rashba spin-orbit coupling [66].

2.2.2 Magnetic Atom adsorbed to a Surface

If a magnetic atom is adsorbed on a surface, the electrons cannot move freely, such that the orbital angular momentum **L** is usually strongly reduced - a so-called quenching occurs [67]. Accordingly, Hund's rules are no longer fully applicable and the total magnetic moment of magnetic atoms on a surface is then mostly reduced to the spin momentum:

$$\mathbf{m} \approx \mathbf{m_S}. \tag{2.24}$$

However, the small remaining orbital moment still couples to the neighboring atoms on the surface via the so-called crystal Coulomb field. Together with the spin-orbit coupling, this results in a preferred orientation of the spin momentum of the atom with respect to the surface lattice, the so-called magnetic anisotropy energy (see Sec. 2.2.4.2).

2.2.3 Band Magnetism: From Hubbard to Stoner

To explain spontaneous magnetization in a macroscopic material (Fe, Co, Ni), the Hubbard model [65] (and, based on it, the Stoner approach [56]) provide important physical results. Basically, the model assumes that the conduction electrons (3d), which also represent permanent magnetic moments, are in a relatively narrow energy band and can only interact with each other in this band. However, since it is a narrow energy band, it has a strong maximum of the probability density at each lattice site, but with a small overlap of wave functions at different sites. Thus electrons can still move from site to site, but with a low probability. Also only two electrons with $S = 0$ are allowed in each band, so that the Pauli principle applies. The Hamiltonian reads [64, p. 393]

$$H_{\text{Hubbard}} = \sum_{ij\sigma} T_{ij} c^\dagger_{i\sigma} c_{j\sigma} + \frac{1}{2} V \sum_{i\sigma} n_{i\sigma} n_{i-\sigma}. \tag{2.25}$$

T_{ij} in the first term is called the hopping integral and includes the electron kinetic energy and the periodic lattice potential, with the creation operator $c^\dagger_{i\sigma}$ and the annihilation operator $c_{j\sigma}$ for electrons with spin σ on sites i and j, respectively. The second term describes the intra-atomic Columb interaction V of the electrons of opposite spin on the same site i with the corresponding occupation operators $n_{i\pm\sigma}$. Although Eq. (2.25) looks quite simple, it is a many-particle problem. Stoner made a molecular field approximation so that the many-particle Hamiltonian becomes a one-particle Hamiltonian. The result of the approach shows a spontaneous band splitting of the densities of states for different spin states when there is a high density of states at the Fermi edge and large Coulomb interaction of electrons in the band. From the susceptibility

$$\chi(T, B=0) = \frac{\chi_0}{1 - \frac{V}{2\mu_B^2}\chi_0} \tag{2.26}$$

and the conditions just explained it can be derived that, for spontaneous ferromagnetism to occur, a material has to fulfill

$$V\rho(E_\mathrm{F}) \geq 1, \tag{2.27}$$

with the Pauli susceptibility χ_0 [68, p.324]. This is known as the Stoner criterion.

2.2.4 Ultra-Thin Magnetic Films and Their Energy Terms

As described above, the Stoner model is useful to understand why spontaneous magnetization can occur at all. In practice, however, we can often as well use the Heisenberg model, which is a pure spin model that does not take the band structure into account. Since the Heisenberg model assumes localized spins (see Sec. 2.2.4.1) whereas the spins of 3d metals are itinerant, one needs to consider effective magnetic moments and exchange constants as well as additional effective energy terms in the Heisenberg model in order to describe the magnetism of 3d magnets sufficiently well. The total energy of the magnetic system then results from the sum of all individual energy terms. By minimizing the total energy, the ground state of the system can be calculated theoretically. In the next sections, the Heisenberg model and the additional energy terms are briefly explained.

2.2.4.1 Exchange Interaction

The **exchange interaction** between two spins was described in 1928 by Heisenberg [69] and is written as follows:

$$H_\mathrm{Heisenberg} = -\sum_{i,j} J_{ij} \mathbf{S}_i \cdot \mathbf{S}_j, \tag{2.28}$$

where $\mathbf{S}_i$ and $\mathbf{S}_j$ are the spin operators acting on the spins i and j, respectively. J_{ij} is the so-called exchange integral, which describes the Coulomb interaction of electrons in the overlapping orbitals Ψ_i and Ψ_j at the locations $\mathbf{r}_1$ and $\mathbf{r}_2$:

$$J = \int \Psi_i^*(\mathbf{r}_1)\Psi_j^*(\mathbf{r}_2) \frac{e^2}{|\mathbf{r}_1 - \mathbf{r}_2|} \Psi_i(\mathbf{r}_1)\Psi_j(\mathbf{r}_2) d\mathbf{r}_1 d\mathbf{r}_2. \tag{2.29}$$

As already mentioned, this exchange interaction describes localized spins with short-ranged next-nearest neighbor interaction. Extensions of the model also consider four-spin exchange interactions or a biquadratic exchange [70]. In the isotropic case, i.e. when the exchange is approximately the same for all directions and for all electrons, an effective J can be assumed and the exchange constant can be taken out of the summation. Furthermore, if the total spin of the atom is large enough ($S >> 1/2$) [71] and if the quantum properties are largely suppressed by the hybridization of the spin-bearing orbitals with the conduction bands in metals, the spin operators can be replaced by classical vectors

$$H_\mathrm{Ex} = -J \sum_{i,j} \mathbf{S}_i \cdot \mathbf{S}_j. \tag{2.30}$$

In the case $J > 0$, the energy is more favorable for an antisymmetric space wave function and a symmetric spin wave function with a total spin of S=1. This means that both spins are parallel, leading to ferromagnetism. Now, if $J < 0$, then a symmetric spatial wave function and an antisymmetric spin wave function with a total spin of S=0 is preferred, i.e. the two spins align antiparallel and in this case antiferromagnetism occurs.
Besides the direct exchange interaction, there are other **indirect exchange interactions**. Here, the spins are mostly strongly localized and interact indirectly, e.g. by conduction electrons (RKKY interaction) or by a super-exchange.

2.2.4.2 Anisotropy

Due to the crystal lattice, the shape or stress, the magnetization may have preferred directions. The magnetocrystalline anisotropy results from the coupling of the spins with their orbitals and thereby also with the crystal lattice. The uniaxial magnetocrystalline anisotropy can be described by

$$E_{\text{aniso}} = \sum_{i=1}^{n} K_i S_z^2, \tag{2.31}$$

where K_i denotes the anisotropy constant. It is negative if the magnetic moments prefer an in-plane magnetization (x-y plane, easy plane) and positive if they prefer a magnetization along the z-axis (easy axis).
The cause of the shape anisotropy, on the other hand, is the long-range dipole-dipole interaction between the spin moments $\mathbf{m}$. The interaction is described by

$$\mathbf{H_{dd}} = \frac{\mu_0}{4\pi} \sum_{i,j} \left[\frac{\mathbf{m}_i \cdot \mathbf{m}_j}{r_{ij}^3} - 3 \frac{(\mathbf{m}_i \cdot \mathbf{r}_{ij})(\mathbf{m}_j \cdot \mathbf{r}_{ij})}{r_{ij}^5} \right] \tag{2.32}$$

with the connection vector $\mathbf{r}_{ij}$ of the spin-moments. The magnetic field generated by the dipole-dipole interaction outside and inside the sample is called the stray field and the demagnetized field, respectively. For thin magnetic layers, the shape anisotropy K_{shape} can be described with the saturation magnetization M_s by

$$K_{\text{shape}} = \frac{\mu_0 M_s^2}{2}. \tag{2.33}$$

2.2.4.3 Dzyaloshinskii-Moriya Interaction

The anisotropic exchange interaction, also known as the Dzyaloshinskii-Moriya interaction (DMI), describes an interaction that occurs between two spin moments mediated by electrons that are subject to strong spin-orbit interaction and inversion symmetry [67]. It can be written as follows:

$$H_{\text{DMI}} = \mathbf{D} \cdot (\mathbf{S}_i \times \mathbf{S}_j) \tag{2.34}$$

where the vector $\mathbf{D}$ describes the interaction between the spins $\mathbf{S}_i$ and $\mathbf{S}_j$ on adjacent lattice sites. Here, $|\mathbf{D}|$ is nonzero only if the inversion symmetry is broken, which is always true on surfaces and in thin film systems. The DMI interaction competes with the isotropic exchange interaction as described in Eq. (2.28) and prefers a perpendicular alignment of the spin moments in the plane which is perpendicular to $\mathbf{D}$. Large DMI interactions are found, for example, in systems with magnetic films on substrates with large spin-orbit coupling, such as the 5d metals Pt, Au, and Ir [72].

2.2.4.4 Zeeman Energy

Another energy contribution is the Zeeman energy. This is the potential energy of a magnetic moment $\mathbf{m}$ in an external magnetic field $\mathbf{B}$:

$$E_{\text{Zeeman}} = -\mathbf{m} \cdot \mathbf{B}. \tag{2.35}$$

The Zeeman energy prefers a parallel alignment of the magnetic moments with the externally applied magnetic field $\mathbf{B}$.

2.3 Superconductivity

After discussing magnetism, the next section deals with superconductivity, first describing the main phenomena followed by the London theory and the BCS theory named after J. Bardeen, L. N. Cooper and J. R. Schrieffer.

2.3.1 Superconducting Phenomena

There are two phenomenological observations related to superconductivity. The most famous was first discovered in 1911 after Heike Kamerlingh Onnes succeeded in liquefying helium and performing experiments at low temperature. He found that the electrical resistance of mercury suddenly dropped to a non-measurable value at a critical temperature (T_c) as shown in Fig. 2.6 [73]. In 1933, 22 years later, it turned out that perfect conductivity below the critical temperature was not the only unusual property of a superconductor. In that year, Walther Meißner and Robert Ochsenfeld discovered that superconductors are perfect diamagnets, meaning that they completely expel an external applied magnetic field from their interior except for a thin edge layer (typical 500 Å) [74]. The property of perfect diamagnetism cannot be explained by perfect conductivity only. To understand this, first the law of induction must be remembered and it must be considered that the time variation of the magnetic flux of an ideal conductor becomes zero because the resistivity ρ in an ideal conductor is zero, and therefore the electric field $\mathbf{E}$ also becomes zero,

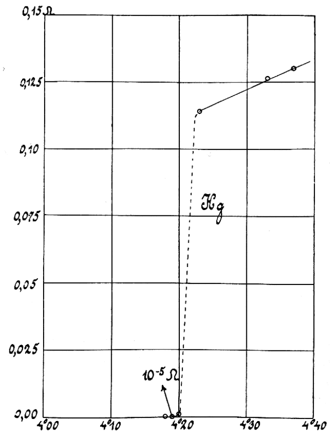

Figure 2.6: Original image of the discovery of superconductivity by Kamerlingh Onnes [73]. The resistance of Hg is plotted as a function of temperature.

$$-\frac{\partial \mathbf{B}}{\partial t} = \nabla \times \mathbf{E} = 0, \tag{2.36}$$

where ∇ is the Nabla operator, $\mathbf{E}$ the electric field and $\mathbf{B}$ the magnetic field. Furthermore

$$\mathbf{j} = \sigma \cdot \mathbf{E} \leftrightarrow \mathbf{E} = \frac{\mathbf{j}}{\sigma} = \rho \cdot \mathbf{j}, \tag{2.37}$$

where $\mathbf{j}$ is the current density, σ is the specific conductance and $\rho = 0$ is the resistivity.

Now we imagine the following thought experiment: If we have a normal conductor (NC), cool it down, so that it becomes an ideal conductor (IC) and apply an external magnetic field, we obtain a complete exclusion of the field in the interior of the conductor shown in Fig. 2.7 **a**, upper path. Due to the perfect conductivity, a permanent circular current is induced at the edge (where the magnetic flux is not zero), which in turn induces

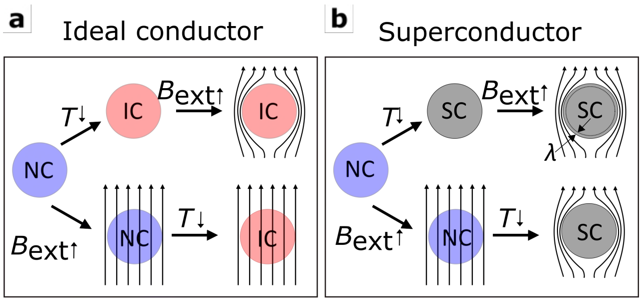

Figure 2.7: Comparison between the behavior of an ideal conductor (**a**) and a superconductor (**b**) in an external magnetic field. Inspired by [75].

an opposite magnetic field according to Lenz's rule, so that this leads to a complete suppression of the magnetic flux inside. However, if we apply the external magnetic field before cooling down, it can penetrate the NC because no infinitely running circle current generates an opposing magnetic field. If the normal conductor has cooled down to an IC, nothing happens because the applied magnetic field does not change in time shown in Fig. 2.7 **a**, lower path. This means that in the case of an ideal conductor, it depends on the order what happens first: the cooling down of the conductor or the application of the magnetic field. For a superconductor (SC), however, this order is not relevant. The displacement of the magnetic field always takes place below T_c, as shown in Fig. 2.7 **b**.

2.3.2 Theoretical Models for Describing Superconductivity

Due to the reversible Meissner-Ochsenfeld effect (see section 2.3.1), it is apparent that the superconducting state must be described thermodynamically. Furthermore, a critical magnetic field (B_{crit}) exists that causes the superconducting state to collapse, since otherwise the superconductor could perform infinite field displacement work.

2.3.2.1 Phenomenological London Theory

In 1935, the brothers Fritz and Heinz London proposed two equations (named after them) to explain the phenomena of superconductivity, or more precisely, the electrodynamics of superconductivity [76]. The first London equation,

$$\frac{\partial}{\partial t}\mathbf{j} = \frac{e^2 n}{m}\mathbf{E}, \tag{2.38}$$

describes the time derivative of the current density which is proportional to the electric field and thus an acceleration of the electrons by an electric field and thereby the perfect conductivity. Here, $\mathbf{j}$ is the superconducting current density, e the charge, m the mass of the charge carriers and n the density of the superconducting electrons. The second London equation describes the Meissner effect and connects the current flow with the magnetic field,

$$\boldsymbol{\nabla} \times \mathbf{j} = -\frac{e^2 n}{mc}\mathbf{B}. \tag{2.39}$$

Substituting the second London equation (2.39) into Maxwell's equation $\boldsymbol{\nabla} \times \mathbf{B} = -\mu_0 \mathbf{j}$ leads to an equation, which describes an exponential decay of the external magnetic field and the screening currents into the superconductor with a decay length given by the so-called London penetration depth λ

$$\lambda = \sqrt{\frac{m}{\mu_0 n e^2}}. \tag{2.40}$$

2.3.2.2 BCS Theory

In 1957 a breakthrough was made by J. Bardeen, L. N. Cooper and J. R. Schrieffer with the first microscopic description of superconductivity [77]. The core of the theory describes an attractive interaction between two electrons by lattice vibrations. The fact that electrons can also attract each other is initially quite counterintuitive. So we will briefly outline a possible attractive interaction that is ultimately an indirect exchange interaction: When an electron moves in a lattice of a crystal, it attracts the positive nuclei as it passes by (see Fig. 2.8 **a**), displacing them from their rest position. Thus, the electron draws a track of deflected positive lattice ions behind itself, which are not instantaneously returned to their rest position, but require a certain time τ for this. While within this time τ the first electron is already gone, a second electron arrives at this place of deflection and experiences an attraction (see Fig. 2.8 **b**). This results in an energy decrease, which indirectly leads to an attractive interaction with the first electron. As can be shown by a maximum **k**-space volume argument, a maximum energy gain is found for electron pairs with wave vectors **k** and −**k**. Bardeen, Cooper and Schrieffer assumed, that the phonon-interaction is spatially isotropic. In such a situation, the two-particle wave function of the bound electron pair has to be symmetric under the exchange of the particles, e.g. an s-wave. Since the electrons are fermions, the overall wavefunction, which is a product of orbital and spin parts, has to be antisymmetric under exchange. Therefore, the spin-part has to be the antisymmetric singlet wave function. Such electron pairs with opposite spins (S=0) are called Cooper pairs [78]. Note that, if the assumption of the spatially isotropic interaction leading to the binding of Cooper pairs is dropped, there are also other possible solutions for the wave function of a binding electron pair. For example, with an antisymmetric *p*-orbital wavefunction and a symmetric spin-triplet spin wavefunction. The resulting superconductor would be called a *p*-wave SC.

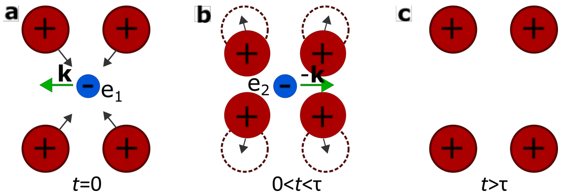

Figure 2.8: Attractive interaction of a Cooper pair. The description can be found in the main text.

However, calculating the energy for a Cooper pair in the Fermi sea reveals an interaction energy smaller than $2E_\mathrm{F}$ [61, p. 45]. This, in turn, means that the energy to form pair states is lowered compared to the energy of free electrons. Instability of the Fermi surface occurs and leads to the formation of a new ground state by the condensation of electrons around the Fermi energy to Cooper pairs.

The BCS ground state pairing Hamitonian H_BCS describes the situation of a phase-coherent superposition of many-body states with pairs of Bloch states ($\mathbf{k}\uparrow, -\mathbf{k}\downarrow$) discussed above, which can be created ($c^\dagger_{\mathbf{k}\uparrow}c^\dagger_{-\mathbf{k}\downarrow}$) or annihilated ($c_{-\mathbf{l}\downarrow}c_{\mathbf{l}\uparrow}$) as units, whereby $c^\dagger$ is the creation and c the annihilation operator for electrons with wave vectors **k**, **l** and spin ↑, ↓. H_{BCS} can be written as [61, p. 53]

$$H_{\mathrm{BCS}} = \sum_{\mathbf{k},\sigma} \xi_{\mathbf{k}} n_{\mathbf{k},\sigma} + \sum_{\mathbf{k},\mathbf{l}} V_{\mathbf{k},\mathbf{l}} c^{\dagger}_{\mathbf{k}\uparrow} c^{\dagger}_{-\mathbf{k}\downarrow} c_{-\mathbf{l}\downarrow} c_{\mathbf{l}\uparrow} \tag{2.41}$$

with the single-particle kinetic energy $\xi_{\mathbf{k}}$ related to the chemical potential μ through

$$\xi_{\mathbf{k}} = \epsilon_{\mathbf{k}} - \mu = \frac{\hbar^2 k^2}{2m} - \mu \tag{2.42}$$

and the particle number operator $n_{\mathbf{k},\sigma} = c^{\dagger}_{\mathbf{k}\sigma} c_{\mathbf{k}\sigma}$. $V_{\mathbf{k},\mathbf{l}}$ describes the attractive interaction potential between electrons given independently by Fröhlich [79] and Bardeen and Pines [80].

Mean Field Ansatz

Because of the phase coherence of a Cooper pair, such operators $c_{\mathbf{k}\uparrow} c_{-\mathbf{k}\downarrow}$ can have nonzero expectation values $b_{\mathrm{k}} = \langle c_{-\mathbf{k}\downarrow} c_{\mathbf{k}\uparrow} \rangle \neq 0$, while in a normal metal, where the phases are random, it averages out to zero. Moreover, the variation around these values should be small due to the high number of particles. It is therefore appropriate to write [61, p. 59]

$$c_{-\mathbf{k}\downarrow} c_{\mathbf{k}\uparrow} = b_{\mathrm{k}} + (c_{-\mathbf{k}\downarrow} c_{\mathbf{k}\uparrow} - b_{\mathrm{k}}), \tag{2.43}$$

where the term in parentheses describes the variation around the mean value. Substituting Eq. (2.43) into Eq. (2.41) and neglecting second order terms of the variation, one obtains the mean field BCS Hamiltonian [61, p. 60]

$$H_{\mathrm{MeanBCS}} = \sum_{\mathbf{k},\sigma} \xi_{\mathbf{k}} n_{\mathbf{k},\sigma} - \sum_{\mathbf{k}} \left(\Delta_{\mathbf{k}} c^{\dagger}_{\mathbf{k}\uparrow} c^{\dagger}_{-\mathbf{k}\downarrow} + \Delta^{\dagger}_{\mathbf{k}} c_{-\mathbf{k}\downarrow} c_{\mathbf{k}\uparrow} - \Delta_{\mathbf{k}} b^{\dagger}_{\mathbf{k}} \right), \tag{2.44}$$

with $\Delta_{\mathbf{k}} = -\sum_{\mathbf{l}} \mathbf{V}_{\mathbf{kl}} b_{\mathbf{l}}$ being the pair potential and $2\Delta_{\mathbf{k}}$ the minimum energy needed to break a Cooper pair.

For later purposes we note here that Eq. (2.44) can be transformed into the Bogoliubov-de Gennes (BdG) form (up to constants)

$$H = \frac{1}{2} \int \Psi^{\dagger}(\mathbf{k}) \mathcal{H}(\mathbf{k}) \Psi(\mathbf{k}) \frac{d^2\mathbf{k}}{(2\pi)^2}, \tag{2.45}$$

with the Nambu Spinor $\Psi(\mathbf{k}) = \left[c_{\mathbf{k}\uparrow}, c^{\dagger}_{-\mathbf{k}\downarrow} \right]^T$ and

$$\mathcal{H}(\mathbf{k}) = \begin{pmatrix} \xi_{\mathbf{k}} & -\Delta_{\mathbf{k}} \\ -\Delta^{\dagger}_{\mathbf{k}} & \xi_{\mathbf{k}} \end{pmatrix}. \tag{2.46}$$

Bogoliubov Transformation for Diagonalization of the Hamiltonian

As Bogoliubov [81] and Valatin [82] have shown independently, a diagonalization of equation Eq.(2.44) can be achieved by a canonical transformation of the creation and annihilation operators

$$c_{\mathbf{k}\uparrow} = u^{\dagger}_{\mathbf{k}} \gamma_{\mathbf{k}0} + v_{\mathbf{k}} \gamma^{\dagger}_{\mathbf{k}l}, \tag{2.47}$$

$$c^{\dagger}_{-\mathbf{k}\downarrow} = -v^{\dagger}_{\mathbf{k}} \gamma_{\mathbf{k}0} + u_{\mathbf{k}} \gamma^{\dagger}_{\mathbf{k}l}, \tag{2.48}$$

with

$$|u_{\mathbf{k}}|^2 + |v_{\mathbf{k}}|^2 = 1. \tag{2.49}$$

Note that $\gamma_{\mathbf{k}0}$ contributes to either annihilating an electron with $\mathbf{k} \uparrow$ or to create one with $-\mathbf{k} \downarrow$. In both cases, the momentum of the system is effectively reduced by $\mathbf{k}$ and the spin by $\hbar/2$. $\gamma^{\dagger}_{\mathbf{k}l}$, on the other hand, increases the total system momentum by $\mathbf{k}$ and spin $\hbar/2$.
If we now substitute Eq. (2.47) and Eq. (2.48) into Eq. (2.44) and choose appropriate $u_{\mathbf{k}}$ and $v_{\mathbf{k}}$,

$$|v_{\mathbf{k}}|^2 = 1 - |u_{\mathbf{k}}|^2 = \frac{1}{2}\left(1 - \frac{\xi_{\mathbf{k}}}{E_{\mathbf{k}}}\right), \tag{2.50}$$

with

$$E_{\mathbf{k}\pm} = \pm\sqrt{\xi_{\mathbf{k}}^2 + |\Delta_{\mathbf{k}}|^2} \tag{2.51}$$

Eq. (2.44) results in the diagonalized mean field BCS Hamiltonian [61]

$$H_{\text{diagBCS}} = \sum_{\mathbf{k}} \left(\xi_{\mathbf{k}} - E_{\mathbf{k}} + \Delta_{\mathbf{k}} b^{\dagger}_{\mathbf{k}}\right) + \sum_{\mathbf{k}} E_{\mathbf{k}} \left(\gamma^{\dagger}_{\mathbf{k}0}\gamma_{\mathbf{k}0} + \gamma^{\dagger}_{\mathbf{k}l}\gamma_{\mathbf{k}l}\right). \tag{2.52}$$

The coefficients $|v_{\mathbf{k}}|^2$ and $|u_{\mathbf{k}}|^2$ can be interpreted as the probabilities that a Cooper pair state with momentum $\mathbf{k}$ is occupied and unoccupied, respectively, where for $E < E_{\mathrm{F}}$ most Cooper pair states are occupied by electrons and for $E > E_{\mathrm{F}}$ most states are unoccupied.
Eq. (2.51) is the dispersion relation of the quasiparticles, resulting in the following density of states of the quasiparticles at $T = 0$:

$$D_s(E_{\mathbf{k}}) = \begin{cases} \frac{E_{\mathbf{k}}}{\sqrt{E_{\mathbf{k}}^2 + |\Delta_{\mathbf{k}}^2|}} & \text{for } |E_{\mathbf{k}}| > |\Delta|, \\ 0 & \text{for } |E_{\mathbf{k}}| < |\Delta|. \end{cases} \tag{2.53}$$

For realistic systems, however, it must be taken into account that the particles have a certain lifetime, which leads to a broadening of the density of states and Eq. (2.53) can be phenomenologically corrected by the Dynes parameter Γ which is inversely proportional to the lifetime [83]:

$$D_s(E_{\mathbf{k}}) = Re\left[\frac{E_{\mathbf{k}} - i\Gamma}{\sqrt{(E_{\mathbf{k}} - i\Gamma)^2 + |\Delta_{\mathbf{k}}^2|}}\right]. \tag{2.54}$$

2.4 Fantastic Majoranas and Where to Find Them

In 1937, Ettore Majorana found real solutions to Dirac's equation that describes the properties and behavior of fermions with spin 1/2 [84]. Majorana's solution of Dirac's equation suggests that fermions could exist which would be their own antiparticles. Expressed mathematically, this means that the creation operator of such particles is identical to the annihilation operator,

$$\gamma = \gamma^{\dagger}. \tag{2.55}$$

So began the search for this particle, named "Majorana" after its theoretical discoverer, and in recent history the search has even extended to solid-state physics because of its potentially promising application to quantum computers (see Chapter 1).

2.4.1 Where to Look

In solid-state physics, electrons and holes can be considered as mutual particle and antiparticle partners, respectively, because of their opposite charge and their ability to "annihilate" (recombine), but their creation ($c^\dagger$) and annihilation (c) operators do not satisfy the Eq. (2.55). However, let us consider an operator that creates an electron and a hole at the same time which is a combination of both operators and has the form

$$\gamma = uc + vc^\dagger, \tag{2.56}$$

with $u, v \in \mathbb{C}$. As can be easily seen, equation (2.56) satisfies the Majorana condition (2.55) exactly when $u = v^*$. Equation (2.56) has a strong similarity to the Bogoliubov operators, Eq. (2.47) and Eq. (2.48), as can be seen when these equations are solved for γ and $\gamma^\dagger$:

$$\gamma = uc - vc^\dagger \tag{2.57}$$

$$\gamma^\dagger = v^* c + u^* c^\dagger \tag{2.58}$$

γ and $\gamma^\dagger$ describe excited Bogoliubov quasiparticle states, but do not satisfy the condition for Majorana operators ($\gamma \neq \gamma^\dagger$), as one can easily check. Thus, analogously to Eq.(2.57, 2.58), a system where the excited quasiparticle states can be described by Eq.(2.56) is searched for, with the Majorana states expected to be at $u = v^*$.

As known from BCS theory, u and v depend on the energy and are equal at $E = 0$ (see Section 2.3.2.2). Accordingly, the search should be performed in a superconducting system at $E = 0$.

However, one point which has been neglected so far is the spin. Even if $u = v^*$ holds, considering the spin, it is $\gamma_\uparrow \neq \gamma_\uparrow^\dagger$. Thus, the fermions have to be made effectively spinless for the Majorana condition (2.55) to be satisfied. This can theoretically be achieved by completely spin-polarizing all fermions and thus effectively making the equations independent of spin, or, in other words, "spinless". However, as shown in Sec. 2.3.2.2 for s-wave superconductors, the Cooper pairs are comprised of a superposition of spin-up and spin-down electrons. An obvious solution would be to search in p-wave-like superconductors, where the Cooper pairs are comprised of electrons of the same spin sort, i.e. they are effectively spin-less.

2.4.2 *p*-Wave Superconductor

Since p-wave superconductors can have nontrivial topological phases, this section uses some terminology from the field of topology. In appendix A.2 and A.3 it is briefly sketched how this mathematical construct can be applied to solid state physics.

However, in nature, no intrinsically p-wave superconducting material could be found yet, although it is predicted that Sr_2RuO_4 should exhibit such a state [17]. Nevertheless, theorists have mathematically constructed p-wave superconductor models and shown that Majorana modes can indeed exist in them. In the following two models are sketched, namely the one- and two-dimensional case of a lattice p-wave superconductor [85].

2.4.2.1 *p*-Wave Toy Model in 1D: Kitaev Chain

The one-dimensional model, known as Kitaev chain [86], which is a simple model for a spin-less, e.g., p-wave superconductor, can be described by the following Hamiltonian, where the nearest neighbor hopping strength is t and the respective lattice site is given by j [85],

$$H_{\text{BdG}} = \sum_j \left[-t \left(c_j^\dagger c_{j+1} + c_{j+1}^\dagger c_j \right) - \mu c_j^\dagger c_j + \Delta \left(c_{j+1}^\dagger c_j^\dagger + c_j c_{j+1} \right) \right]. \tag{2.59}$$

After a lattice Fourier transformation, the Hamiltonian can be easily diagonalized in the Nambu notation, which leads to an energy spectrum of [85]

$$E_\pm = \pm\sqrt{\left(2t\cos(k) + \mu\right)^2 + 4\Delta^2 \sin^2(k)}. \tag{2.60}$$

From Eq. (2.60), one can see that the gap is closed when $\mu = -2t$, as also shown exemplarily in Fig. 2.9 **a**. This gap closing marks the transition between a topologically trivial and nontrivial phase. When $\mu < -2t$ (strong pairing, gray line in Fig. 2.9 **a**) the system is topologically trivial and for $\mu > -2t$ (weak pairing, red line in Fig. 2.9 **a**) the system is topologically nontrivial[4].

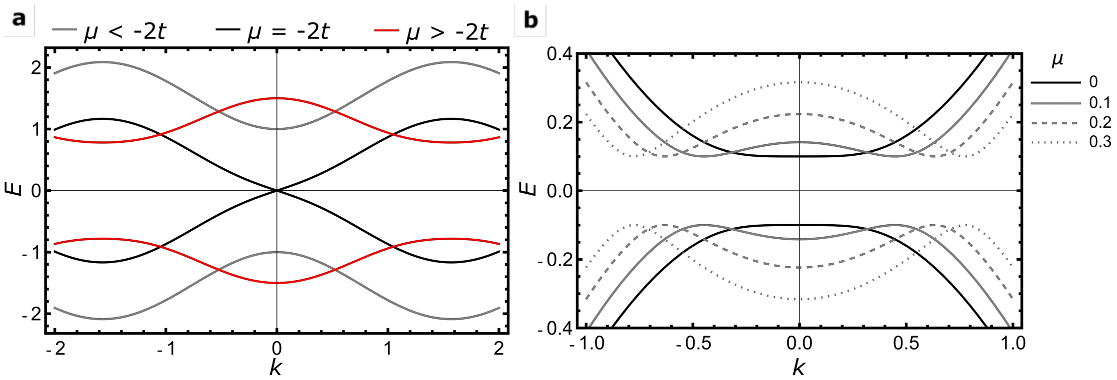

Figure 2.9: The energy bands of the Kitaev chain shown in **a** versus a s-wave superconductor shown in **b** using $E_\pm = \pm\sqrt{\left(\frac{\hbar^2 k^2}{2m} - \mu\right)^2 + |\Delta_{\mathbf{k}}|^2}$ with $m = 1$, $\Delta = 0.1$ and different values of μ (specified in the legend) are shown. Note that while the s-wave SC always exhibits an energy gap, it closes at the critical point $\mu = -2t$ for the p-wave SC.

To gain a better understanding, the system can be viewed from a different perspective [85]. For this purpose, the complex fermion operators $(c_j, c_j^\dagger)$ are described with Majorana operators $c_j = \frac{1}{2}(\gamma_{2j-1} + i\gamma_{2j})$ and $c_j^\dagger = \frac{1}{2}(\gamma_{2j-1} - i\gamma_{2j})$, where γ_j and $\gamma_j^\dagger$ fulfill Eq. (2.55) and, substituted into Eq. (2.59), gives

$$H_{BdG} = \frac{i}{2} \sum_j \left[-\mu\gamma_{2j-1}\gamma_{2j} + (t+\Delta)\gamma_{2j}\gamma_{2j+1} + (-t+\Delta)\gamma_{2j-1}\gamma_{2j+2} \right]. \tag{2.61}$$

For the trivial phases $\mu < 0$ and $|\Delta| = t = 0$, the Hamiltonian reduces to $H = -\mu\frac{i}{2}\sum_j(\gamma_{2j-1}\gamma_{2j})$. In this state the Majoranas are each coupled at one physical lattice site.

If we now consider a special case from the topological phase, namely $|\Delta| = t > 0$, $\mu = 0$, then the Hamiltonian reduces to $H = +it\sum_j(\gamma_{2j}\gamma_{2j+1})$. This couples two Majoranas at different physical lattice sites, leaving two uncoupled Majorana states localized at the ends of the chain, and since the coupling between the two decreases exponentially with distance, they are found to a good approximation at $E = 0$.

---

[4] Gap closing by variation of μ in the s-wave superconductor is not possible as exemplarily illustrated in Fig. 2.9 **b**.

2.4.2.2 Lattice p-Wave Model in 2D

For the 2D p-wave model Eq. (2.59) can be extended to [85]

$$\begin{aligned} H_{\mathrm{2D}} = \sum_{m,n} -t\left(c^\dagger_{m+1,n}c_{m,n} + h.c.\right) - t\left(c^\dagger_{m,n+1}c_{m,n} + h.c.\right) - (\mu - 4t)c^\dagger_{m,n}c_{m,n}c_j \\ + \left(\Delta c^\dagger_{m+1,n}c^\dagger_{m,n} + \Delta^* c_{m,n}c_{m+1,n}\right) + \left(i\Delta c^\dagger_{m,n+1}c^\dagger_{m,n} - i\Delta^* c_{m,n}c_{m,n+1}\right) \end{aligned} \tag{2.62}$$

where m and n are the lattice sites and, for simplicity, a lattice constant of $a = 1$ is assumed. Furthermore, the pairing amplitude is anisotropic and has a phase i in the y-direction compared to the x-direction. Performing a Fourier and gauge transformation and setting $t = \frac{1}{2}$, for simplicity, and shifting the chemical potential by the constant $4t$ [85], Eq. (2.62) can be written in BdG form,

$$H_{\mathrm{2D}}(\mathbf{k}) = (2 - \mu - \cos(k_x) - \cos(k_y))\tau_z - 2|\Delta|\sin(k_x)\tau_y - 2|\Delta|\sin(k_y)\tau_x \tag{2.63}$$

with τ_{i} representing the Pauli matrices in the particle-hole space. The energy spectrum is found to be

$$E_\pm(\mathbf{k}) = \pm\sqrt{(2 - \mu - \cos(k_x) - \cos(k_y))^2 + 4|\Delta|^2(\sin^2(k_x) + \sin^2(k_y))}. \tag{2.64}$$

Eq. (2.64) has several critical points as can be seen in Fig. 2.10 where the gap closes, assuming $|\Delta| \neq 0$. Fig. 2.10 **a-c** shows these critical points as a function of (k_x, k_y, μ) at (0, 0, 0), (π, 0, 2), (0, π, 2), and (π, π, 4). The phases can be characterized by the Chern number (see appendix A.3) and it can be proved that the topologically trivial phases are found at $\mu < 0$ and $\mu > 4$ while the topologically nontrivial phases of opposite chirality are found at $0 < \mu < 2$ and $2 < \mu < 4$, respectively.

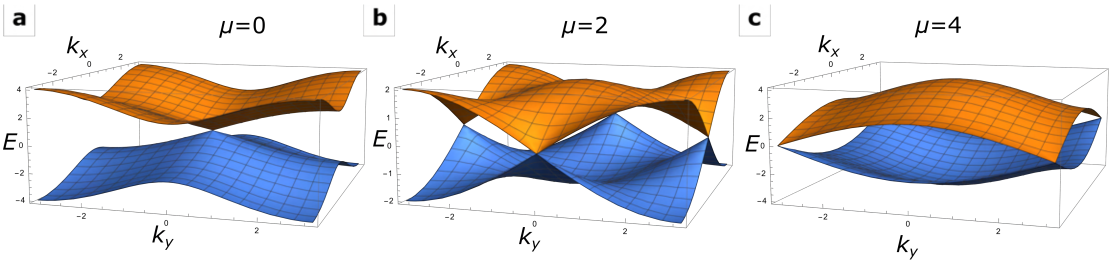

Figure 2.10: Shown here are the energy bands of a 2D p-wave model (Eq. (2.64)) at different critical points as a function of μ, k_x, and k_y with $\Delta = 0.5$.

In case the system is indeed in a topologically nontrivial state (in certain circumstances), it can be shown that such a two-dimensional system shows an energy gap in the bulk of the 2D system, while at the interface, i.e. at the edge, Majorana modes (with a decay length) can be found which are propagating and crossing the energy gap. This means that at E_{F} and near E_{F} Majorana modes have a dispersion (see [85, p. 207]), which results in a particular form of the measured density of states (dI/dV) close to the edges and around the bulk gap [28–30, 85, 87].

2.4.3 Realization of a p-Wave-like Superconductor

For a concrete implementation of the spinless p-wave models in both 1D [86] and 2D [88, 89], the spin-degeneracy of the bands of an s-wave SC (see Fig. 2.9 **b**) must be

lifted. This can be experimentally realized by taking a metallic wire (or an island in the 2D case), and proximity coupling [90] this to an ordinary s-wave superconductor, which provides sufficient spin-orbit coupling, and additionally apply a magnetic field.
With the help of Fig. 2.11 it will be briefly sketched what effect spin-orbit coupling and the magnetic field have on the resulting band structure of such a system, which is described by the following Hamiltonian [14, 91, 92]

$$H = \left(\frac{k^2}{2m} - \mu + \alpha k \sigma_x - \mu\right)\tau_z - B\sigma_z + \Delta\tau_z \tag{2.65}$$

and results to

$$E_\pm = \frac{k^2}{2m} - \mu \pm \sqrt{(\alpha k)^2 + B} \tag{2.66}$$

if $\Delta = 0$ for simplicity. Here α describes the strength of the spin-orbit field originating from the Rashba spin-orbit coupling and B the Zeeman field. If neither spin-orbit coupling nor a magnetic field is turned on then degenerated energy bands result, which is shown in Fig. 2.11 **a**. Next, in Fig. 2.11 **b** the case of an existing spin-orbit coupling with a vanishing magnetic field ($B = 0$ and also $\Delta = 0$) is shown. One gets two parabolic bands (blue and black) touching at $k = 0$, which prevents the states from being fully spin-polarized. With a non-vanishing magnetic field, however, the energy bands are separated from each other (see Fig. 2.11 **c**) and if μ is located inside the gap, the lower occupied band is fully spin-polarized or effectively "spinless". However, the direction of the spin polarization is k-dependent, which is essential since it allows to have antiparallel spins at E_F and therefore allowing the spins to couple with Cooper pairs. This enables to open up a topologically non-trivial gap at E_F if the system is proximitized to an s-wave superconductor ($\Delta > 0$ see [92] for details).

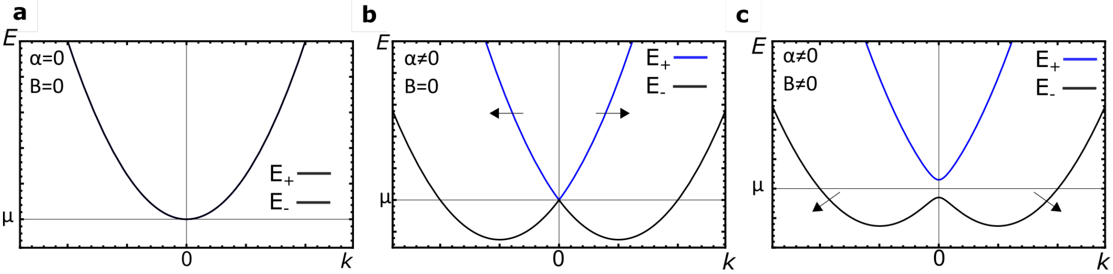

Figure 2.11: Three different cases are shown here, where in **a** both spin-orbit coupling α and the magnetic field B are switched off. In the next panel the bands are shown when spin-orbit coupling is switched on and in **c** with an additional magnetic field. Now the lower band is fully spin polarized, but with a spin polarization that is k-dependent [92]. Note that in all three cases $\Delta = 0$.

Instead of applying an additional external magnetic field, the chain or island can also be built of magnetic atoms, which should then automatically provide the required B-field in the form of an exchange splitting. This setup is motivated by the observation that arrangements of multiple coupled spins are usually magnetically stable for sufficiently long time-scales at low temperatures [22, 93, 94] and that the spins may arrange themselves ferromagnetically [21]. However, by ferromagnetic ordering, the Shiba states would all be perfectly spin-polarized along the same direction, which would render the s-wave host superconductor unable to proximity-pair the electrons in the Shiba bands (see below). Therefore, either a chiral spin-texture or a strong spin-orbit coupling is also needed to generate the required p-wave pairing correlation.
In the next section, first it will be discussed how a system of an s-wave superconductor

with one magnetic impurity behaves, and then what happens when there are several of such magnetic impurities coupled to each other.

2.4.3.1 Single Magnetic Impurity on Superconductor: Shiba States

If a magnetic impurity, such as a magnetic atom, is located on an s-wave superconductor, both a Coulomb interaction (potential scattering) and a magnetic interaction (magnetic scattering) of the atom with the electrons of the superconductor can occur [95]. The latter leads to a potential that can break Cooper pairs, resulting in bound pair states within the energy gap of the superconductor. These states were theoretically predicted independently in the late 1960s by Yu[96], Shiba [97], and Rusinov [98] and are therefore called Yu-Shiba-Rusinov states or Shiba states for short. If the spin is treated in a quasiclassical fashion as a local magnetic exchange field, the corresponding Hamilton operator for the problem can be written as [13]:

$$H_{\mathrm{YSR}} = \left(\frac{p^2}{2m} - \mu\right) \ \boldsymbol{\tau}_z + \left[V\boldsymbol{\tau}_z - J\ \mathbf{S}\ \boldsymbol{\sigma}\right]\ \delta(\mathbf{r}) + \Delta\boldsymbol{\tau}_x. \tag{2.67}$$

The first term is the kinetic energy of the single particles relative to the chemical potential μ (as already given in Eq. (2.41)). In the second term, J is the strength of the exchange interaction (see Sec. 2.2.4.1) between the spin $\mathbf{S}$ and the electrons of the superconductor. The strength of the potential scattering is described by V. $\boldsymbol{\sigma}$ and $\boldsymbol{\tau}$ describe the Pauli matrices acting in different spaces, namely the spin and the particle-hole space (and can be connected via a tensor product; see Eq. A.4 for the definition of the single Pauli matrices). Moreover, it is assumed that the Coulomb and exchange interactions act only very locally in the vicinity of the local magnetic impurity, which, in turn, is described mathematically by a delta function $\delta(\mathbf{r})$. In Eq. (2.67) the energy of the d-bands is assumed to be far from the Fermi energy of the superconductor, so the electronic structure of the impurities is not taken into account.

The Hamiltonian set up in Eq. (2.67) leads to a pair of bound states symmetrically around the Fermi energy, which are located in the energy gap of the superconductor ($|E| < \Delta$) [13]

$$E_{\mathrm{YSR}} = \pm\Delta\frac{1-\alpha^2+\beta^2}{\sqrt{(1-\alpha^2+\beta^2)^2+4\alpha^2}}, \tag{2.68}$$

with unitless parameters $\alpha = \pi\rho SJ$ and $\beta = \pi\rho V$ and the density of states ρ of the superconductor in the normal phase.

The particle and hole components u_{r} and v_{r} of the BdG quasiparticle solutions $\Psi_{\mathrm{r}} = \begin{pmatrix} u_{\mathrm{r}} \\ v_{\mathrm{r}} \end{pmatrix}$ are spin polarized in the direction $\mathbf{S}$, as can be seen from the Nambu eigenspinors[5] at the position of the impurity [13]:

$$\Psi^{+}_{\mathrm{r}=0} = C\begin{pmatrix} \sqrt{1+(\alpha+\beta)^2} \\ 0 \\ \sqrt{1+(\alpha-\beta)^2} \\ 0 \end{pmatrix}, \Psi^{-}_{\mathrm{r}=0} = C\begin{pmatrix} 0 \\ \sqrt{1+(\alpha-\beta)^2} \\ 0 \\ -\sqrt{1+(\alpha+\beta)^2} \end{pmatrix}, \tag{2.69}$$

where C is a normalization factor.

Using scanning tunneling spectroscopy (STS), the components $|u_{\mathrm{r}}|^2$ and $|v_{\mathrm{r}}|^2$ can be

---

[5] Analogous to [13] we choose the Nambu spinor ordered as $\Psi(r) = (\psi_{\uparrow}(r), \psi_{\downarrow}(r), \psi^{\dagger}_{\downarrow}(r), -\psi^{\dagger}_{\uparrow}(r))^T$

studied individually, since there are no other states close to the Fermi level due to the spectral gap. At a bias voltage of $V = +E_{\mathrm{YSR}}/e$, electrons from the tip can tunnel into the Shiba state and analogously holes at $V = -E_{\mathrm{YSR}}/e$. The expected local density of states is therefore $\rho(\mathrm{r}, E) = |u_{\mathrm{r}}|^2\delta(E - E_{\mathrm{YSR}}) + |v_{\mathrm{r}}|^2\delta(E + E_{\mathrm{YSR}})$. However, while the energies E are symmetric with respect to the Fermi energy, the tunneling intensity is not symmetric with the bias voltage for $\beta \neq 0$, since the particle and hole amplitudes are normalized according to Eq. (2.49). Thus, for Shiba states, a symmetric energy around the Fermi energy with asymmetric intensity distribution is expected in the STS spectrum.

If the d-electron energy of the adatoms is close to E_{F} of the superconductor, the electronic structure of the adatoms should be considered. This can be done with a mean-field approach of the Hubbard model, where the magnetic adatoms are described by Anderson impurities (spin 1/2). If, to a good approximation, the spin-up impurity level is occupied and the spin-down level is empty, equation (2.68) becomes [13]

$$E = \pm\Delta \frac{\Gamma^2 + E_{d\uparrow}E_{d\downarrow}}{\sqrt{(\Gamma^2 + E_{d\uparrow}E_{d\downarrow})^2 + \Gamma^2(E_{d\uparrow} - E_{d\downarrow})^2}}, \tag{2.70}$$

with $\Gamma = \pi\rho t^2$, $E_{d\uparrow} = \epsilon_d - \mu$ and $E_{d\downarrow} = \epsilon_d - \mu + U$.

2.4.3.2 Multiple Magnetic Impurities on a Superconductor: Shiba Bands and Tuning of Shiba Bands

Let us now consider an array of magnetic impurities placed on an s-wave superconductor. If the adatoms are sufficiently far apart so that the overlap of the orbitals is small and accordingly the hopping between the atoms can be neglected at low energies, the Shiba states will hybridize to a narrow so-called Shiba band (see Fig. 2.12 **a**). As the coupling between the atoms, and thus the hybridization, becomes stronger, the bandwidth will increase so that the Shiba band may overlap with the Fermi level (see Fig. 2.12 **b**). When this happens, the induced pairing correlation can again open a gap, a so-called minigap, which is then of p-wave nature due to the spin polarization of the Shiba states and thus fundamentally different from the s-wave gap of the superconductor. It is a topologically nontrivial phase which can host Majorana bound states under certain circumstances.

The simplest system that may realize these properties is a chain of magnetic adatoms (1D) placed on an s-wave superconductor with strong spin-orbit coupling. Assuming that the hopping and pairings are dominated by nearest neighbors, such a chain can be described by the Hamiltonian of the Kitaev chain (2.59) if one replaces $-\mu$ by the energy of the Shiba states E_0 [13]. Analogous to the calculation of section 2.4.2.1, it can then be shown that the Shiba states can form a topologically nontrivial phase for which $\mu = \pm 2t$ mark the phase transitions. For the special case $t = \Delta > 0$ and $\mu = 0$ in this topological phase, it can also be shown that unpaired Majorana states can be found at the ends of the chain whose operators commute with the Hamiltonian and thus have zero energy [13, 85].

In the case where the system is not in the two pure special cases (trivial ($\mu < 0$, $t = \Delta = 0$) or nontrivial ($\mu = 0$, $t = \Delta > 0$)), a mixture of Majorana operators in the Hamiltionian that couple at the same and neighboring lattice sites is obtained. However, if the chain is long enough, the Majorana modes can still survive because they are localized at the ends of the chain whose coupling decreases exponentially with the length of the chain and therefore can still remain at $E = 0$ [85].

The theoretical calculations for the realization of a 2D p-wave superconductor by a Shiba lattice, i.e., a square two-dimensional arrangement of ferromagnetic atoms, were carried out by Li et al. [29] among others [87, 99]. Li et al. made a distinction between densely packed magnetic impurities (each lattice site is coupled to a magnetic moment) and dilute packed magnetic impurities, whereby the first case is supposed to be representative for a self-assembled island. They found several cases with topologically nontrivial phases that can exhibit Majorana edge modes. Assuming that $2t > \sqrt{J^2 - \Delta^2}$[6] with the condition that $\mu = (2i + j)t + \lambda\sqrt{J^2 - \Delta^2}$, $i, j, \lambda = \pm 1$, they were able to show that depending on which values μ takes, Chern numbers of $C = -1, 0, +2, 0, -1$ are found, where the number of Majorana modes corresponds to the Chern number.

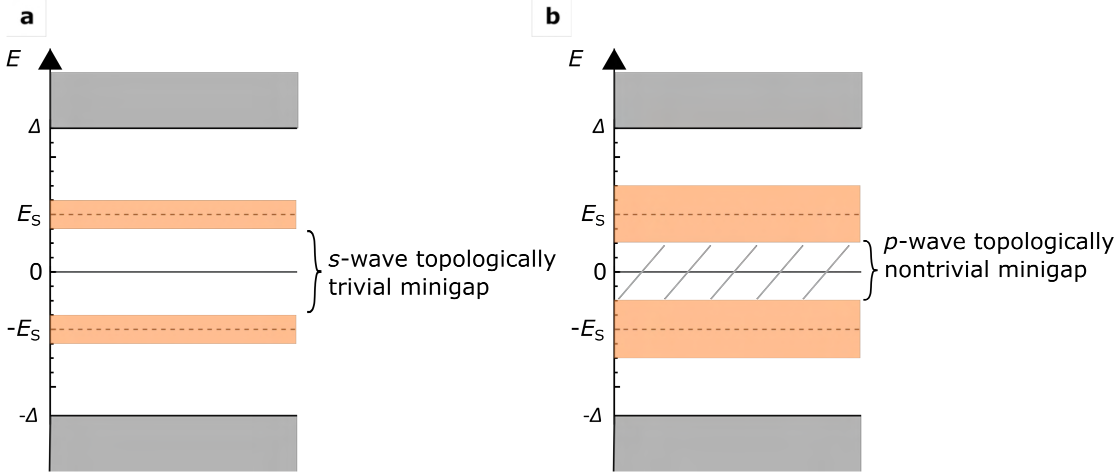

Figure 2.12: Inspired by [13] in **a** the formation of Shiba bands in the energy gap is shown, induced by magnetic impurities, that are far apart. In **b** nearby magnetic impurities lead to the formation of energetically wider Shiba bands that overlap with E_F creating a p-wave pairing which in turn opens a topologically nontrivial p-wave minigap.

2.4.3.3 Disorder Effects on Majorana Zero Modes

It has been shown by theoretical calculations that the effects on topological properties of 1D [100–102] and 2D [103–105] Shiba lattices due to disorder can be strong. Here, a distinction is usually made between potential disorder mediated by a perturbation of the chemical potential $\mu_\mathbf{r} = \overline{\mu} + \delta\mu_\mathbf{r}$ (with a constant background $\overline{\mu}$ and random disorder $\delta\mu_\mathbf{r} \in [-w, w]$), and magnetic disorder. In the case of magnetic disorder, different types of perturbations can again be distinguished: One possibility is a perturbation of the strength of the exchange interaction, which thus becomes location-dependent, $J \rightarrow J_\mathbf{r}$. Another type of disorder arises when the spins lose ferromagnetic alignment, so that the orientation of the spins can be treated as 'orientational disorder'. A third type of disorder is realized by keeping the orientation of the spins aligned with uniform J, but with a probability p for every lattice site that the magnetic moment is absent.

---

[6] t nearest neighbor hopping integral in the superconductor, J exchange coupling constant between electrons of the SC and the magnetic impurity, α the strength of the Rashba spin-orbit coupling and Δ the pairing energy.

For the case of a ferromagnetic spin chain (1D) [102], it has been shown that the Majorana bound states are surprisingly insensitive to disorder in the potential of the superconductor as long as it does not show strong disorder (Agwoga et al. [102] consider generic potential disorder in the superconductor in terms of a site-dependent chemical potential randomly distributed $\delta\mu_i \in [-w, w]$, where w describes the strength of the disorder). By extending the chain length, the stability against disorder can even be increased, although on the other hand the topological minigap becomes increasingly sensitive to disorder.

In the 2D case, e.g., in a layer with a Rashba-type spin-orbit coupling sandwiched between a superconductor and a ferromagnet, a very weak potential perturbation initially decreases the localization length of the Majorana state as the perturbation strength increases [104]. However, when the disorder is of the order of the p-wave pairing energy, it increases again [104].
If the perturbation terms of the chemical potential are correlated with each other with a correlation length ℓ (e.g., by a Gaussian correlation, $\overline{\delta\mu_{\mathbf{r}}\delta\mu_{\mathbf{r}'}} = \delta\overline{\mu}^2 e^{-|\mathbf{r}-\mathbf{r}'|^2/\ell^2}$), the disorder can have an even more significant negative impact on the Majorana zero modes [105]. The effect of the disorder becomes particularly strong when the correlation length ℓ is comparable to the coherence length of the superconductor η, while the effect is not so destructive in the cases $\ell \ll \eta$ and $\ell \gg \eta$.

Magnetic disorder has been studied for the 1D spin chain system [106], which showed that the topological phase is relatively sensitive to such types of disorder.
For a 2D system of magnetic adatoms on an s-wave superconductor with spin-orbit coupling, all previously described types of disorder were investigated and compared by Mascot et al. [103]. In doing so, they were able to show that the system under consideration has two topologically nontrivial phases with Chern numbers $C = 2, -1$ in the absence of disorder (see also appendix A.2), which can be suppressed by all types of disorder. Here, the magnetic disorder suppresses the topologically nontrivial phases more strongly than a potential disorder, where the disorder with randomly missing magnetic moments leads to the strongest suppression of the topological phases. Interestingly, however, it has also been shown that both potential and magnetic disorder can favor topologically nontrivial phases in 2D Shiba lattices when the chemical potential is near the bottom or top of the electronic band. In these cases, a topologically nontrivial phase can also be generated (with a Chern number of $C = -1$) by a disorder-induced increase in the charge density.

Chapter 3

Instrumentation and Sample Preparation

3.1 Low-Temperature STM and Ultra-High Vacuum System

Overall, the measurements of this work were performed in three laboratories: one equipped with an STM cooled by a continuous liquid He-flow cryostat (VT-STM), one equipped with an STM built into a Joule-Thompson effect cryostat (JT-STM) and one equipped with an STM built into a liquid He bath cryostat (Helium-bath STM). In all three systems, the STM is located in ultra-high-vacuum (UHV) chamber systems, which contain very similar standard surface science equipment used for the preparation of samples. But they do differ by the cryostat and thus by the temperature that can be reached with it, as well as by whether or not a magnet is installed. If a magnet is present, a further distinction can be made regarding which field strengths can be achieved and in which directions the magnetic fields can be applied. The VT-STM can operate at temperatures ranging from 16 K to 300 K and has no magnet. The JT-STM can be operated at temperatures down to 1 K (though for the work presented in this thesis the system was operated at a temperature of 4 K due to technical problems) and has a magnet that can apply a magnetic field of up to 2.8 T in the z-direction, i.e. vertical to the sample (out-of-plane). In the following, the He-bath STM is exemplarily described in more detail, which was mainly used for the measurements in this work. A detailed description of the VT-STM is given by Kuck et al. [107] and Goedecke [108]. The JT-STM has been described in detail by L. Cornils [109], among others.

3.1.1 He-bath STM System

The system was built in 1997 by Wittneven et al. [110] and is one of the first systems that combined the ability to perform scanning tunnel spectroscopy at liquid-Helium temperatures in UHV conditions and in a strong magnetic field (see Fig. 3.1 **a** for a current photo of the system). The system stands on passive air springs, on a foundation which is decoupled from the building complex and can be roughly divided into three UHV chambers and the cryostat. In Fig. 3.1 (b) a sketch of the system is shown: on the left is the preparation chamber, in the middle the STM chamber with the cryostat (including magnets) mounted below, and on the right the deposition chamber. All UHV chambers operate at a base pressure of about $1 \cdot 10^{-10}$ mbar or less. The preparation chamber is mainly used for cleaning the surfaces of crystals. Accordingly, the instruments needed

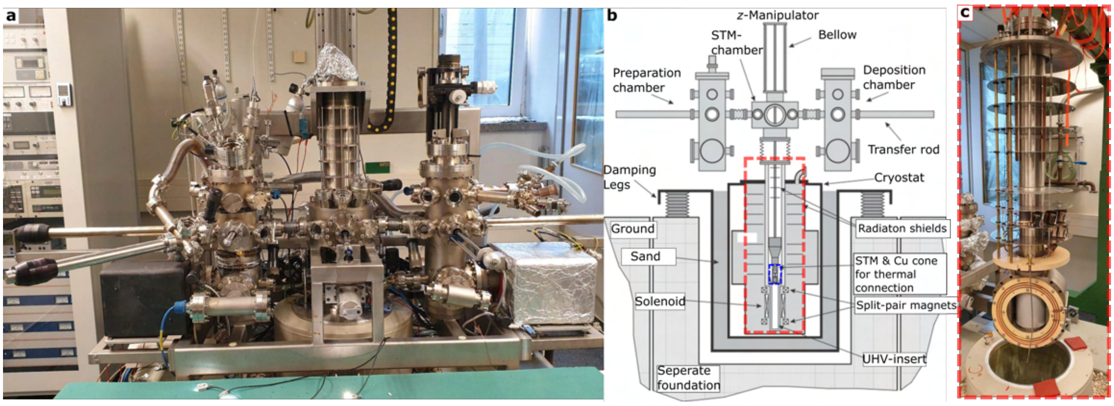

Figure 3.1: The He-bath STM system is shown in **a** with a schematic sketch of the system in **b** [110] and a photo of the insert with solenoid and split pair magnets and the radiation shields in **c**.

for cleaning are mainly located here. Most importantly for the work performed for this thesis, an ion sputter gun and an e-beam stage (home built) are installed in the preparation chamber in order to be able to heat up the samples. A load lock is additionally attached to the preparation chamber in order to transfer samples or tips into and out of the UHV system. If a material is to be deposited on the surface of a single crystal for investigation, the crystal can be transferred to the deposition chamber, where the material evaporators are installed. Here, different materials can then be evaporated onto the crystal, such as elemental iron.

Once a sample is prepared, it is transferred back to the STM chamber and inserted into the STM. The actual STM is attached to a copper cone, which can be moved down into the cryostat by the z-manipulator, such that the cone is pressed into a copper countercone in the measuring position (see Fig. 3.2 **a**) to ensure good thermal contact with the liquid He bath. For additional vibration isolation, the cryostat is embedded in sand inside of a metal frame which rests on the air springs. The magnets are located in the helium dewar (see Fig. 3.1 **c** for the insert taken out of the helium dewar). Between the cryostat and the STM there is a cavity which can be filled with so-called exchange gas (He) which is responsible for the thermal contact of the liquid helium bath and the STM in the vacuum chamber. The cryostat is capable of cooling the STM down to 6.5 K and has two magnets which can generate a maximum B-field of 6.5 T perpendicular to the sample surface (solenoid magnet) and a maximum B-field of 2 T within the sample surface plane (split-pair magnet). The microscope is a home made STM and can be seen in Fig. 3.2. Fig. 3.2 **b** shows the entire STM head, which is then connected to the copper cone with the threaded rods (above). In Fig.3.2 **c** the tip which is clamped into a tip holder can be seen, which in turn is hold in a piezo tube by means of a spring. The piezo tube has five electrodes, four segments on the outer surface which, if set under high voltage, enable a controlled bending of the tube in horizontal $\pm x$ and $\pm y$ directions, respectively, and one on the inner surface which enables an extension or contraction in the vertical z-direction. Also the soldered copper wires on the tube scanner, with that the electrical voltage can be applied, can be seen. The tube scanner, in turn, is installed in a sapphire prism. Fig. 3.2 (d) shows where it is mounted into the STM head as well as the sample slot above it into which a sample can be inserted. By applying high voltage ramps to six other piezo stacks between which the sapphire prism is clamped, four of which are shown in Fig. 3.2 **e**, the coarse approach of the tip is performed, moving the

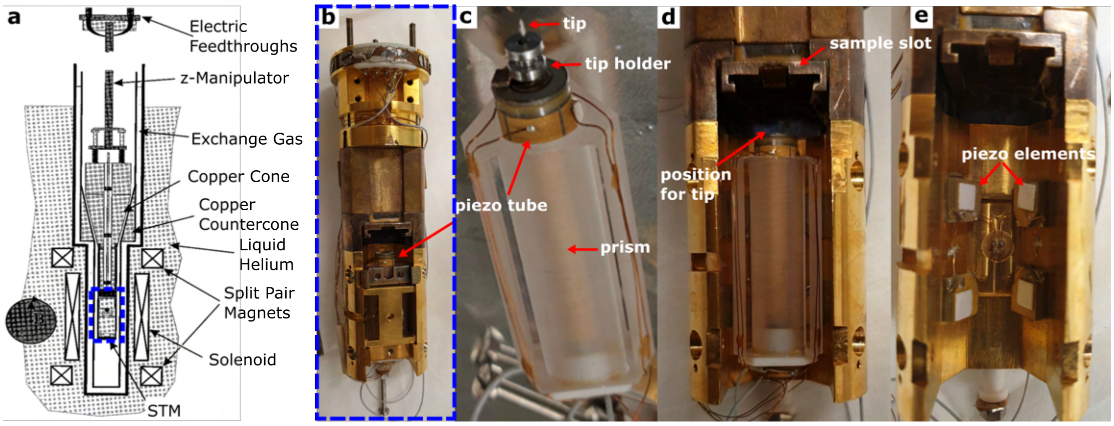

Figure 3.2: In **a** the solenoid and split-coil magnets surrounding the cone and counter cone with the mounted STM head (dashed blue rectangle) is shown [110]. **b-e** STM head and its individual parts. The description can be found in the text.

prism in the $\pm z$-direction. After the coarse approach, the sample surface can be scanned line-by-line via the tube scanner, with a measurement range of about 1x1μm^2.

3.1.2 Measurement Methodology

STM-images were measured at constant tunnel current I with a bias voltage V applied to the sample, for which the corresponding values are always given in the figure captions. dI/dV point spectra were obtained by stabilizing the tip at a given point above the surface at stabilization current I_{stab} and bias V_{stab} (usually V_{stab} is the first voltage value at which the spectroscopy starts), switching off the feedback loop, and recording the differential tunneling conductance as a function of sample bias V using the standard Lock-In technique where the modulation voltage V_{mod} of frequency f (approximately in the range of $f = 1000\,\text{Hz}$ to $2000\,\text{Hz}$) is added to the bias voltage. The modulation voltage V_{mod} for measurements near the Fermi energy (in the range of $V = -6\,\text{mV}$ to $V = 6\,\text{mV}$) was usually $V_{\text{mod}} = 0.1\,\text{mV}$ and for larger energies ($V = -1\,\text{V}$ to $V = 1\,\text{V}$) $V_{\text{mod}} = 10\,\text{mV}$. Spectroscopic line profiles and spectroscopic fields were taken by recording point spectra on one- and two-dimensional grids, respectively, over the surface. In contrast, dI/dV maps were recorded in constant-current mode in parallel to usual STM-images.

3.2 Tip and Sample Preparation

This section will briefly introduce the preparation of the tip and sample, which is necessary for the experimental measurements in this work.

3.2.1 Tip Preparation

Depending on the task, different tips were used to obtain the results presented in this work. For atomically resolved images in Sec. 4.3 the measurements were performed with an electrochemically etched W-tip. In order to clean the W-tip for the measurements and remove impurities, it was flashed several times in UHV.
For high energy resolution measurements, such as spectroscopic measurements within the energy gap (of Nb), a pure niobium tip was used (Sec. 4.5), which increases the energy resolution at elevated temperatures beyond the Fermi-Dirac limit [24, 60]. For this purpose, a niobium wire was mechanically sharpened and, analogous to the W-tip, flashed after being introduced into the UHV chamber to remove impurities.
Spin-polarized measurements (Sec. 4.4) were performed by carefully dipping the Nb-tip into an Fe island so that a cluster of Fe is attached to the tip and the tip is thus spin-polarized. Here, after dipping, point spectroscopy on Nb(110) was performed to check for the presence of YSR states indicating that magnetic material has been successfully transferred to the tip. It is expected that after successful transfer of a small amount of magnetic Fe material, the tip behaves soft magnetic and aligns fully parallel to the external magnetic field already at a few hundred mT [111].

3.2.2 Preparation of Niobium

Niobium is a transition metal in the 5th period and belongs to the vanadium group. In nature, niobium does not occur in its pure state, but mostly in combination with oxygen and other metals (for example $(\mathrm{FeMn})(\mathrm{NbTa})_2\mathrm{O}_6$ or $(\mathrm{FeMn})(\mathrm{NbO}_3)_2)$. It is obtained by chemical processes, such as by means of electrochemical or chemical reduction [112].

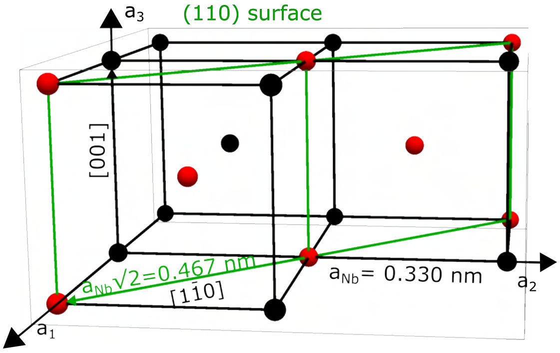

Figure 3.3: Sketch of the Nb bcc lattice with the (110) plane indicated with green lines, containing the Nb atoms marked in red.

Physically, niobium is known for being an elemental s-wave superconductor of second type with the highest critical temperature of all elementary superconductors of $T_\mathrm{c} = 9.2$ K. The coherence length ξ of the Cooper pairs is $\xi = 38$ nm and the upper critical magnetic field is $B_{\mathrm{c}2} = 289$ mT± 7 mT at $T = 4.2$ K [113]. The metal crystallizes in a body-centered cubic (bcc) structure and has a lattice constant of $a = 330$ pm (see

Fig. 3.3).

All niobium single crystals used in this work, i.e. the one with the Nb(111) surface as well as the one with the Nb(110) surface, were purchased from the company MaTeck Material-Technologie & Kristalle GmbH, which states a purity of 99.99% [114]. Despite the high purity, however, oxygen impurities are still present, and for the experiments at least the surface should be largely free of impurities.

As described in detail in Chapter 1, both Nb(111) and Nb(110) were prepared and investigated in this work. The preparation of the surfaces is described in the following sections.

3.2.2.1 Preparation of Nb(110)

For the cleaning of the (110) surface, an already established procedure reported by Odobesko et al. [115] has been applied. The crystal and the surface undergo a cleaning process in which they are first sputtered, as is typical for surface experiments, and then briefly flashed several times at very high temperatures close to the melting tem-

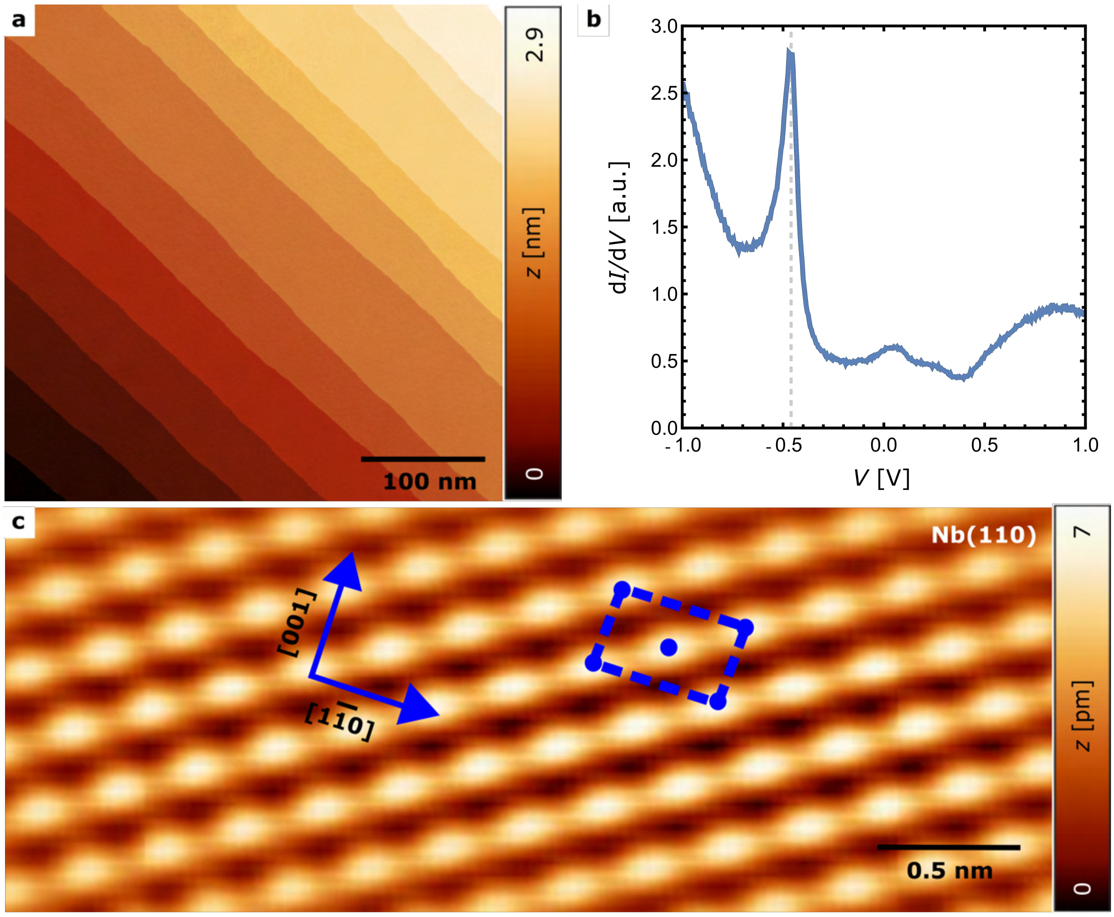

Figure 3.4: In **a** a STM overview image of Nb(110) with several terraces is shown ($V = -1\,\text{mV}$, $I = 30\,\text{pA}$, $T = 6.5\,\text{K}$). In **b** point spectra are shown, taken on clean Nb(110) with a vertical gray dashed line marking the Nb(110) surface state at negative bias around $V = -450\,\text{mV}$ ($V_{\text{stab}} = 1\,\text{V}$, $V_{\text{mod}} = 10\,\text{mV}$, $f = 1197\,\text{Hz}$, $I_{\text{stab}} = 0.5\,\text{nA}$, $T = 4.5\,\text{K}$). In **c** an atomically resolved STM image of Nb(110) is shown together with the crystallographic directions and the conventional unit cell dashed in blue lines ($T = 6.5\,\text{K}$, $V = -10\,\text{mV}$, $I = 5\,\text{nA}$).

perature of Nb. The last point is crucial here, since flashing allows desorption of the oxygen impurities from the crystal surface. However, since the melting point of Nb is $T = 2750\,\mathrm{K}$, heating must be done with great care. In Fig. 3.4 **a**, a typical overview image ($400 \times 400\ \mathrm{nm}^2$) with several terraces of clean Nb(110) is shown. Moreover, in Fig. 3.4 **b**, the characteristic peak of clean Nb(110) at $V = -450\,\mathrm{mV}$ can be seen, which was identified as the signature of the d_{z^2} type surface state [115]. When applying an out-of-plane magnetic field of $B = 100\,\mathrm{mT}$, flux tubes typical for a type II superconductor can be observed at a low sample bias voltage (in this case $V = -1\,\mathrm{mV}$), forming a hexagonal lattice (see Fig. 3.5 **a**). Point spectra of the surface further demonstrate the disappearance of the gap upon increasing the magnetic field, as shown in Fig. 3.5 **b**.

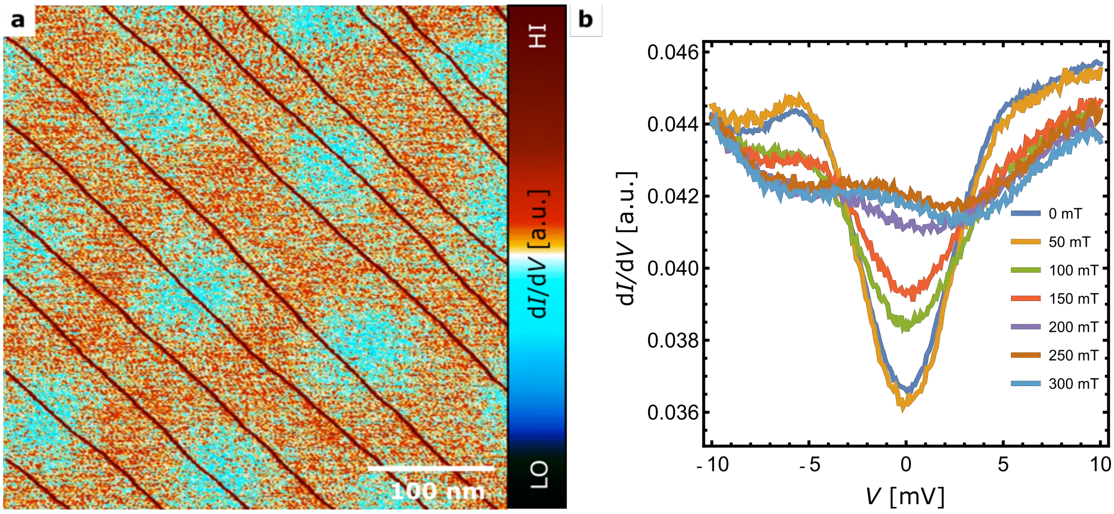

Figure 3.5: In **a** the simultaneously recorded $\mathrm{d}I/\mathrm{d}V$ image of Fig. 3.4 **a** at $T = 100\,\mathrm{mT}$ is shown, which clearly shows the typical flux tubes of a type II superconductor arranged in a hexagonal lattice ($V = -1\,\mathrm{mV}$, $V_{\mathrm{mod}} = 0.5\,\mathrm{mV}$, $f = 977\,\mathrm{Hz}$, $I = 30\,\mathrm{pA}$, $T = 6.5\,\mathrm{K}$). **b** Point spectra taken on clean Nb(110) at different B-fields as indicated and shown in different colors in the plot ($V_{\mathrm{stab}} = -10\,\mathrm{mV}$, $V_{\mathrm{mod}} = 0.5\,\mathrm{mV}$, $I_{\mathrm{stab}} = 0.5\,\mathrm{nA}$, $T = 6.5\,\mathrm{K}$)

3.2.2.2 Preface to the Preparation of Nb(111)

In contrast to Nb(110), there is no established method for cleaning the surface of Nb(111) yet. Therefore, a method for cleaning the (111) surface was developed in this work. The problems associated with cleaning the surface are described below. In Sec. 4.1 the developed method is described in detail as a result of this work.

As mentioned earlier, niobium exhibits a bcc crystal structure. Looking at the (111) surface sketched in Fig. 3.6, the hexagonal lattice is shown which is containing the Nb atoms marked in red, with the plane being indicated by the green lines/arrows. The hexagonal lattice exhibits a lattice constant of $a_{\mathrm{Nb}(111)} = a_{\mathrm{Nb}}\sqrt{2} = 0.467\,\mathrm{nm}$, making it a rather open surface in contrast to Nb(110). However, this feature raises a problem. If impurities, especially oxygen are present in the crystal (which is usually the case), the surface cannot be cleaned simply by sputtering and heating, as it is done for Nb(110). Actually, if it is heated to very high temperatures, about $T > 2013\,\mathrm{K}$, which must be the case to dissolve the oxygen from the crystal, a rearrangement of the surface atoms occurs, leading to surface facetting.

In fact, Coupeau et al. [116] reported the preparation of clean Nb(111) solely by sputtering and annealing. The annealing temperature they used was only $T = 1250\,\mathrm{K}$. According to our own experience and reports from the literature [115, 117–119], this temperature is too low to dissolve the oxygen from the niobium crystal or its surface. A possible explanation could be that the Nb material they used was already relatively cleaner compared to the commercially available crystals which nevertheless provide a purity of 99.99%.

However, if this surface could be made accessible for further experiments, it would be an ideal choice for realizing promising 2D magnet-superconductor hybrid systems due to the high transition temperature (above 9 K) of Nb between the normal conducting and superconducting state. Furthermore, if magnetic monolayers are deposited on the (111) surface, the threefold symmetry could give rise to a frustrated spin system favoring skyrmions or other non-collinear spin-structures. It is, therefore, of great interest to also make Nb(111) accessible with all its possibilities, just as the Nb(110) surface was made accessible by Obodesko et al. [115].

The results that have been achieved in the context in this work are described in Chapter 4.1.

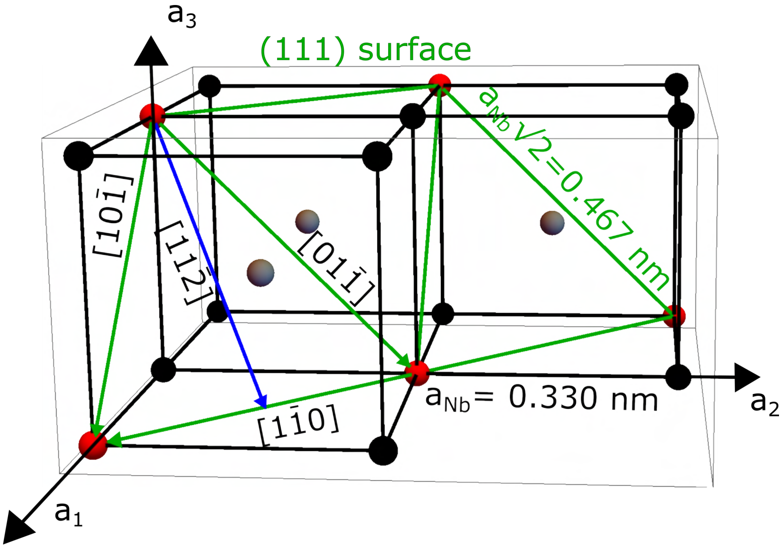

Figure 3.6: Sketch of the Nb bcc lattice with the (111) plane. The Nb(111) plane is containing the Nb atoms marked in red and forms a hexagonal lattice, with a side length of $a_{\mathrm{Nb}}\sqrt{2} = 0.467\,\mathrm{nm}$. Also drawn are the crystallographic directions in the crystal lattice.

3.2.3 Preparation of Iron on Niobium

Iron, one of the most abundant elements on earth, belongs to the 3d transition metals and has the electron configuration $[\mathrm{Ar}]3\mathrm{d}^6 4\mathrm{s}^2$. The metal crystallizes at room temperature as a bulk material in a bcc structure with a lattice constant of $a_{\mathrm{Fe}} = 287\,\mathrm{pm}$. In this work, for the deposition of iron on niobium, iron was evaporated onto the niobium surface using an e-beam evaporator immediately after the crystal clean-up procedure described in Sec. 3.2.2 for Nb(110) and in Sec. 4.1 for Nb(111). The evaporation was performed at room temperature for Nb(110) and at $T = 520\,\mathrm{K}$ for Nb(111). To ensure that the iron source was clean, the evaporator was extensively outgassed beforehand. After evaporation, the sample was quickly transferred to the STM to avoid possible contamination.

Chapter 4

Experimental Results and Discussion

In this chapter, the results of this work are presented and discussed. The results of the investigation of Nb(111) are shown and discussed in Sec. 4.1. In Sec. 4.2 and Sec. 4.3, the growth and the structure of the Fe layers on Nb(110) are investigated. Afterwards, the magnetic studies of Fe/Nb(110) are presented in Sec. 4.4 followed by the low energy measurements in Sec. 4.5.
The results from Sec. 4.1 to Sec. 4.1.2 are summarized in the publication "Preparation and STM study of clean Nb(111) surfaces" [120] while the results from Sec. 4.2 to Sec. 4.1.3 are summarized in the publication "Correlation of Magnetism and Disordered Shiba Bands in Fe Monolayer Islands on Nb(110)". [121].

4.1 Investigation of Niobium (111)

One goal of my thesis was to make the niobium (111) surface accessible for further experiments, as mentioned in Chapter 1 and Sec. 3.2.2.2. This section describes the experiments I did in order to achieve a recipe for the preparation of an atomically clean surface of a Nb(111) single crystal. At first the initial attempts to clean Nb(111) by sputter-annealing cycles will be described (Sec. 4.1.1), followed by the treatment with atomic hydrogen and the determination of the atomic structure (Sec. 4.1.2). Finally, in Sec. 4.1.3, the deposition of iron on Nb(111) is addressed.

4.1.1 Attempts of Cleaning Nb(111) by Sputter-annealing Cycles

A Nb(111) single crystal purchased from Mateck with a purity of 99,99% [114] was bonded to a tungsten sample plate and introduced into the VT-STM system, where the base pressure in the preparation chamber was $p_{\mathrm{base}} \approx 10^{-10}$ mbar. Cleaning experiments were performed typically with cycles of argon ion sputtering and annealing. For the first cycles, a sputtering time of 60 min was used to initially remove large contaminants, with an annealing time of 10 min. After twelve cycles, the sputtering time was reduced to 30 min whereas the annealing time remained the same. After each cycle, the crystal was then transferred to the STM and investigated, with the temperature being further increased each time. The measurement temperature was $T = 25\,\mathrm{K}$.

Fig. 4.1 **a** shows an overview image of the surface after it has been annealed to $T \approx 1387\,\mathrm{K}$. The surface exhibits nanoscale roughness, and no well-defined atomic terraces have formed yet. This means that this temperature is not sufficient to heal the

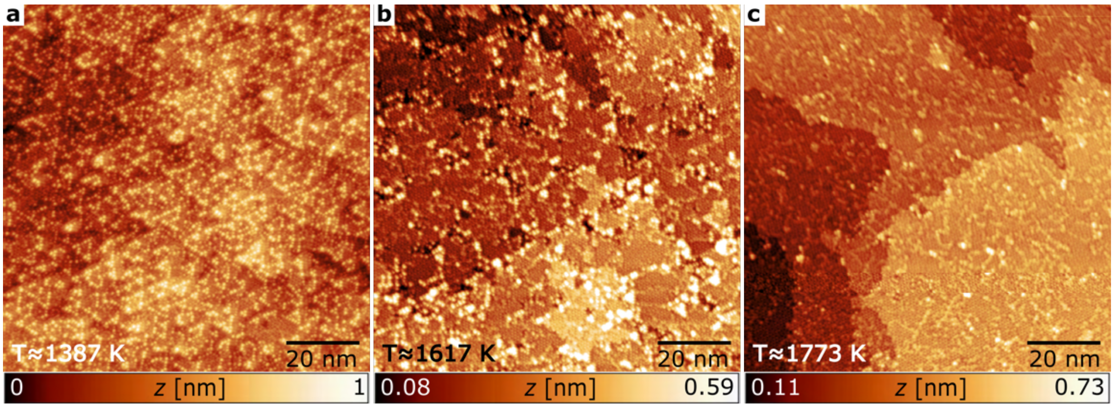

Figure 4.1: In **a** to **c** STM image series of the crystal surface shows how the crystal gradually forms a mostly flat surface with terraces as the temperature increases. In this process, the crystal was heated to **a** $T \approx 1387\,\text{K}$, **b** $T \approx 1617\,\text{K}$ and **c** $T \approx 1773\,\text{K}$. The measurement parameters are **a**: $V = 500\,\text{mV}$, $I = 150\,\text{pA}$; **b**: $V = 500\,\text{mV}$, $I = 120\,\text{pA}$; **c**: $V = 500\,\text{mV}$, $I = 50\,\text{pA}$ with $T = 25\,\text{K}$.

surface from sputtering after 10 minutes of annealing. Increasing the annealing temperature to $T \approx 1617\,\text{K}$ (Fig. 4.1 **b**) leads to the formation of larger terraces, although still, some nanoscale holes and clusters on top can be observed. The STM image in Fig. 4.1 **c** shows the crystal surface now after annealing to $T \approx 1773\,\text{K}$. Compared to Fig. 4.1 **b**, the terraces are larger and mostly closed. In a smaller scale-image, which can be seen in Fig. 4.2 **a**, a hexagon super-lattice can be identified. The distances of the hexagon super-lattice, measured in the different directions, shown in the schematic sketch Fig. 4.2 **b**, are approximately twice the length of the hexagonal atomic lattice of Nb(111). These data are in agreement with those of Coupeau et al. [116], whose studies suggest that the Nb(111) surface is associated with a specific atomic structure characterized by a lattice constant twice as large as for a truncated (111) plane of bcc Nb and thus, a (2×2) reconstruction forms which has an atomic density reduced by 4. In addition, elongated clusters can be seen on the surface, which appear bright in Fig. 4.2 **a**. It is most probable

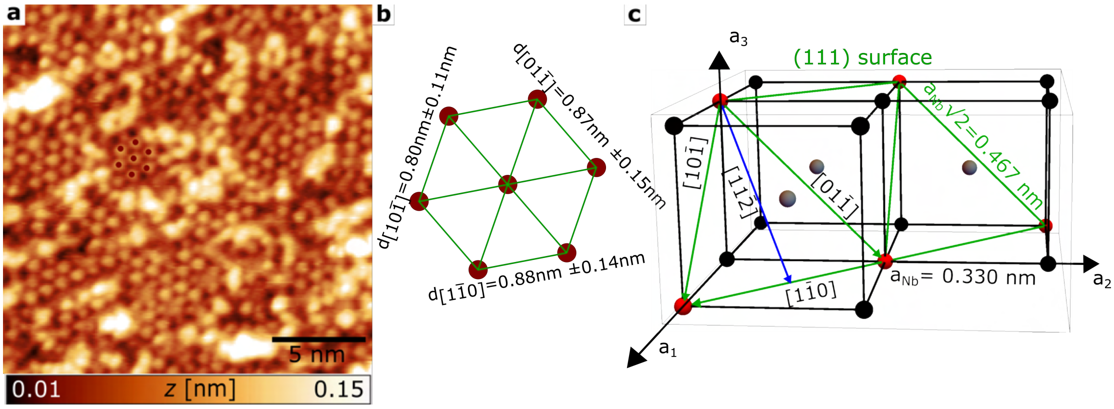

Figure 4.2: In **a** a close up of the surface which was annealed at $T \approx 1773\,\text{K}$ shows clusters on top of a hexagonal super-lattice structure. A schematic sketch **b** of the underlying hexagonal super-lattice from **a** with measured distances given in the figure, where in **c** the crystal structure is given as a reminder. Measurement parameters: **a** $V = 500\,\text{mV}$, $I = 50\,\text{pA}$, $T = 25\,\text{K}$.

that these clusters are correlated to oxygen impurities. However, since Nb_2O_5 is already

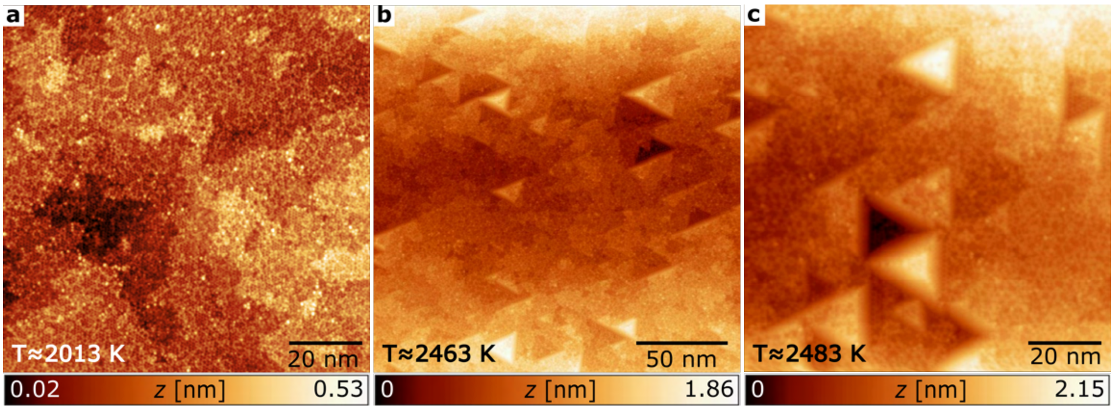

Figure 4.3: Shown in **a** is the surface after annealing at $T \approx 2013\,\mathrm{K}$, where no increase of the terrace size is visible in comparison with the STM image of Fig. 4.1 **c**, where the Nb(111) crystal has been annealed up to $T \approx 1773\,\mathrm{K}$. However, if the crystal is heated further to $T = 2463\,\mathrm{K}$, pyramid "hill" and "valley" structures **b** form which continue to grow in height and depth, respectively with increasing annealing ($T \approx 2483\,\mathrm{K}$) **c**. Measurement parameters for **a**: $V = 500\,\mathrm{mV}$, $I = 50\,\mathrm{pA}$, $T = 25\,\mathrm{K}$; **b**: $V = -2\,\mathrm{V}$, $I = 50\,\mathrm{pA}$, $T = 25\,\mathrm{K}$; **c**: $V = 2\,\mathrm{V}$, $I = 50\,\mathrm{pA}$, $T = 25\,\mathrm{K}$.

reduced at $T \approx 423\,\mathrm{K}$ [122, 123] and NbO_2 is reduced at $T \approx 613\,\mathrm{K}$ [123, 124], it can be assumed that these clusters relate with oxygen impurities in a composition of NbO. As already known from own experience during the preparation of Nb(110) and from the literature, NbO is a very stable composition, which, in the case of Nb(110) dissolves from the crystal surface only at temperatures above $T \approx 2730\,\mathrm{K}$ [115]. Therefore, for Nb(111), an analogous procedure to the preparation of oxygen-free Nb(110) was followed by heating the crystal to a higher temperature, since no facetting could yet be detected. In Fig. 4.3 **a** an STM image of the crystal surface which was annealed for 10 min at about $T \approx 2013\,\mathrm{K}$ can be seen. Interestingly, no increase of the terrace size could be found. Instead, the clusters described above, which are very likely related to oxygen impurities, could be observed more frequently. This observation suggests that further heating drives the diffusion of oxygen from the crystal interior to the surface, although the temperature does not yet seem to be high enough to completely dissolve NbO from the surface. As already investigated by Odobesko [115], diffusion of oxygen atoms in

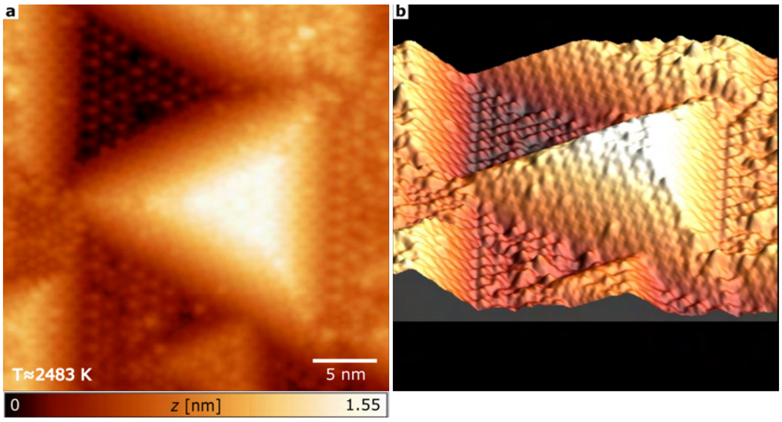

Figure 4.4: A close-up of a pyramid island can be seen in **a** while **b** is showing a 3D representation of the same image. Measurement parameters: $V = -750\,\mathrm{V}$, $I = 500\,\mathrm{pA}$, $T = 25\,\mathrm{K}$.

the bulk during heating is a problem that one can try to solve by flashing the crystal only for a very short time (a few seconds), so that the oxygen atoms at the surface are released, but not long enough to allow further oxygen atoms to diffuse from the bulk to the surface [115]. After annealing at $T \approx 2463\,\mathrm{K}$ it was possible to observe the formation of triangular islands and vacancy islands (see Fig. 4.3 **b**). Then, after heating at $T \approx 2483\,\mathrm{K}$ (see Fig. 4.3 **c**) these progressively formed into pyramid structures, as can be more clearly seen in Fig. 4.4 **a** and **b**. This observation is typical for a surface where a facetting occurs: An initially planar surface forms into a 'hill-and-valley' structure like in [125, 126].
Possible pyramid structures on a bcc(111) surface are the {011} and the {211}-pyramid [125] as shown schematically in Fig. 4.5 **a**.
The work of Madey et al. shows that the {211} pyramid structure has a lower total surface energy than the {011} structure. In addition, step edges, indicated in Fig. 4.5 **b** by the red arrows, could be clearly found, which most likely supports the hypothesis of a {211} pyramid structure. Therefore, the pyramid structures found are most likely of the {211} type.
In summary, however, these results strongly indicate that cleaning the Nb(111) surface of a single crystal with a certain amount of residual oxides in a reasonable time is not possible by only sputtering and annealing due to facetting.

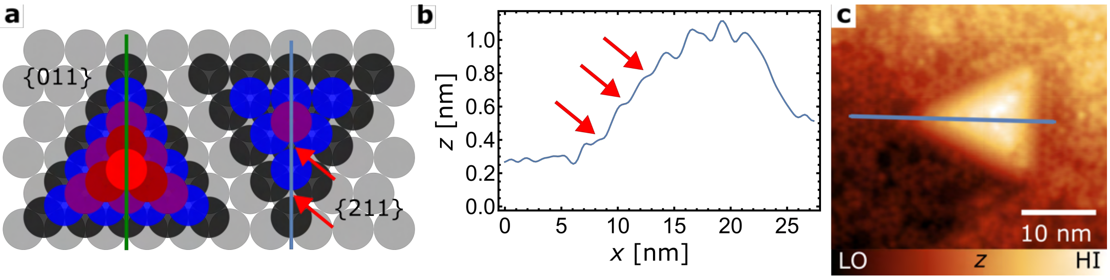

Figure 4.5: In **a** a schematic sketch (inspired by [125]) is showing the different variations for a {011}- and {211}-pyramid structure, where the blue vertical line indicates the expected orientation of the line profile shown in panel **b** taken over the pyramid structure in the STM image in panel **c**. The red arrow shows the steps found on the flat edge. Measurement parameters: $V = 2\,\mathrm{V}$, $I = 50\,\mathrm{pA}$, $T = 25\,\mathrm{K}$.

4.1.2 Niobium(111) Treatment with Atomic Hydrogen

Based on the results described in Sec. 4.1.1, an alternative chemical approach was chosen to achieve a clean Nb(111) surface. For this purpose, a hydrogen source has been installed in the preparation chamber of the VT-STM to chemically reduce niobium oxide with atomic hydrogen. In the literature, the reduction of niobium oxide can also be found being done with carbon, but the temperature required for the reaction is relatively high, up to $T \approx 2773\,\mathrm{K}$ [112, 127–129]. This is rather unfavorable for Nb(111) because of facetting (see Fig. 4.4). With atomic hydrogen, however, at least the reduction of $\mathrm{Nb_2O_5}$ should proceed without difficulty [129]:

$$\mathrm{Nb_2O_5} + 10\,\mathrm{H} \rightarrow 2\,\mathrm{Nb} + 5\,\mathrm{H_2O} + 360900\,\mathrm{cal} \tag{4.1}$$

For the preparation, the sample was exposed to atomic hydrogen at a pressure of $p \approx 10^{-7}$ mbar for $t \approx 16$ h, with additional slight heating at $T \approx 473\,\mathrm{K}$. Fig. 4.6 **a** shows

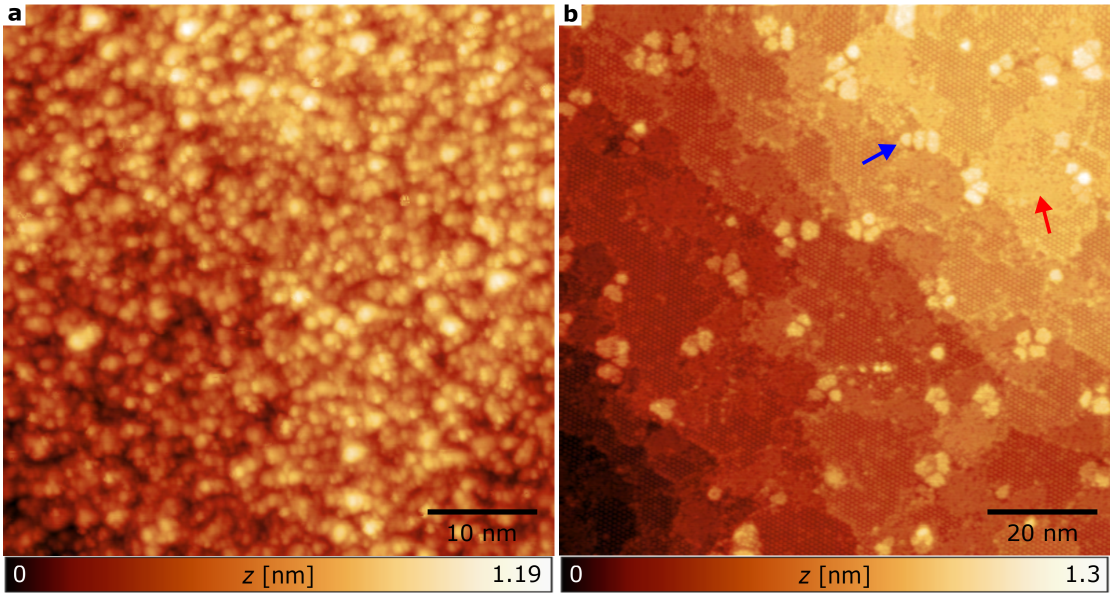

Figure 4.6: In **a** a surface after treatment with atomic hydrogen is shown, where a rough surface can be observed. After short flashes a surface appears **b** on which the hexagonal super-lattice structure can be seen very clearly. Furthermore, a differently structured surface (such a region is indicated with a red arrow) and, in addition, some elevated clusters (blue arrow) can be detected. Measurement parameters **a**: $V = 500\,\text{mV}$, $I = 50\,\text{pA}$, $T = 25\,\text{K}$; **b**: $V = 100\,\text{mV}$, $I = 1\,\text{nA}$, $T = 25\,\text{K}$.

the surface after the described treatment. Theoretically, under the given experimental conditions (hydrogen-pressure and $T \approx 473\,\text{K}$), if the reduction has occurred as described in Eq. (4.1), any H_2O produced should have already been evaporated. Thus, there should be no water molecules on the surface. However, since this is ultimately an etching process, i.e. a chemically material removal of the surface takes place (considering that the oxygen is also part of the surface), it is not surprising to find a rough surface after the treatment with atomic hydrogen (like after a sputtering process). After five short flashes (with a duration of 5 s each) at $T \approx 1273\,\text{K}$ the surface morphology changed considerably, as can be seen in Fig. 4.6 **b**: The surface clearly shows the underlying hexagonal super-lattice structure which was already described in the context of Fig. 4.2. In addition, the number of elongated clusters is decreased and a reduced number of higher clusters with a height of about 0.3 nm-0.4 nm (indicated with a blue arrow) are visible now. Also, other areas can be seen, which exhibit a denser structure than the hexagonal super-lattice, with one area in the image marked with a red arrow for clarity. After five more flashes, the higher clusters are no longer present (see Fig. 4.7 **a** and **b**) and the formation of large (over 50 nm wide) terraces is observed. Much more remarkable, however, are the atomically resolved STM images of the hexagonal super-lattice shown in Fig. 4.7 **b**, Fig. 4.8 **a** (and only partially in Fig. 4.8 **b**) and the dense structure in the upper half of the images. These two images in Fig. 4.8 indicate that earlier STM topography images of the hexagonal super-lattice were not atomically resolved. It becomes clear when Fig. 4.8 **a** and **b** are compared. Both are images of exactly the same area of the sample. Fig. 4.8 **a** shows atomic resolution of the surface in the whole image frame, while in Fig. 4.8 **b**, after about one-fifth of the image has been scanned from the top to the bottom, a change in the tip has occurred, revealing the familiar hexagonal super-lattice with twice the lattice constant of Nb(111) (bottom of Fig. 4.8 **b**). As we will see in following, the STM images of Coupeau [116] are not atomically

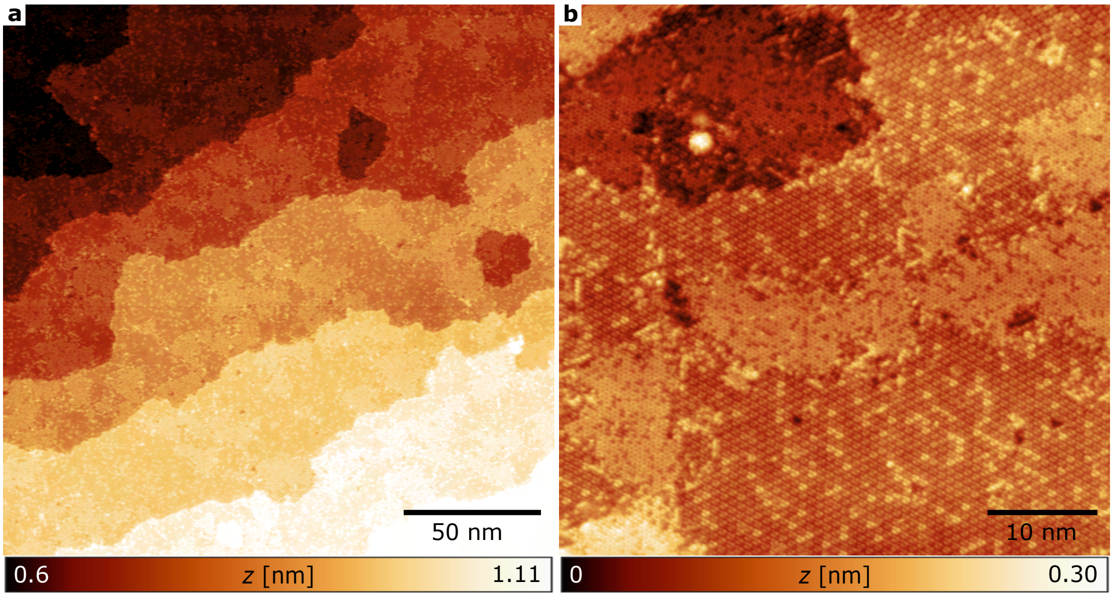

Figure 4.7: Figure **a** shows broad terraces with apparently two kinds of different structures. In **b** a close-up of **a** is shown, with atomic resolution. Measurement parameters **a**: $V = 100\,\text{mV}$, $I = 1\,\text{nA}$, $T = 25\,\text{K}$; **b**: $V = 100\,\text{mV}$, $I = 1\,\text{nA}$, $T = 25\,\text{K}$.

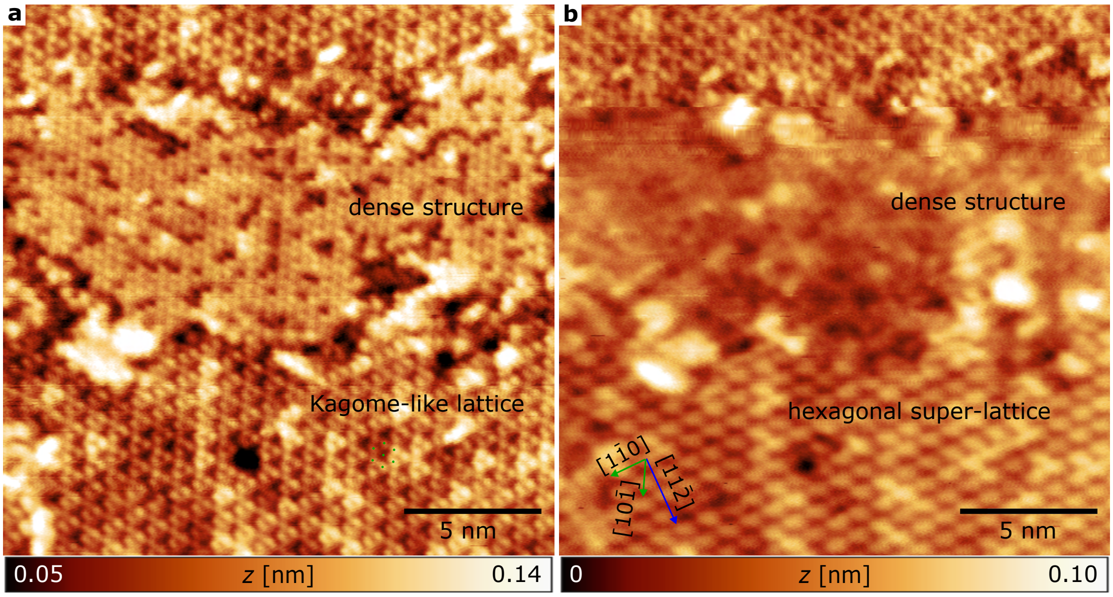

Figure 4.8: **a** and **b**: STM images taken at the same location on the surface. In **b** the atomic resolution is lost after about one fith of the image size has been scanned (image scanned from top to bottom). Also plotted are the crystallographic directions. Measurement parameters for **a**: $V = -500\,\text{mV}$, $I = 1\,\text{nA}$, $T = 25\,\text{K}$; **b**: $V = 1\,\text{V}$, $I = 1\,\text{nA}$, $T = 25\,\text{K}$.

resolved images. A close-up of the image with atomic resolution is shown in Fig. 4.9 **a**. In this image, the observed lattice of the surface is indicated with blue dots. It is noticeable that for a hexagonal lattice, if one considers the hexagon with one atom at each corner and one in the center, most of the time the atom in the center seems to be missing and thus this Nb(111) surface exhibits a Kagome-like lattice structure. However, also regions for which this is not the case can be found in Fig. 4.9 **a** (denoted with green dots). Measurements in both Fourier space and real space (see appendix A.4.1.2) of the shortest atomic distances in $[1\bar{1}0]$, $[10\bar{1}]$, and $[01\bar{1}]$ directions are shown in Fig. 4.9 **b**, agreeing very well with the theoretical value of the lattice constant of Nb(111), which is $a_{\mathrm{Nb}} = 0.467\,\mathrm{nm}$. The typical height of the atoms is approx. 20 pm (see line profile in the appendix Fig. A.4). The unit cell of the Kagome-like structure is shown in Fig. 4.9 **b**.

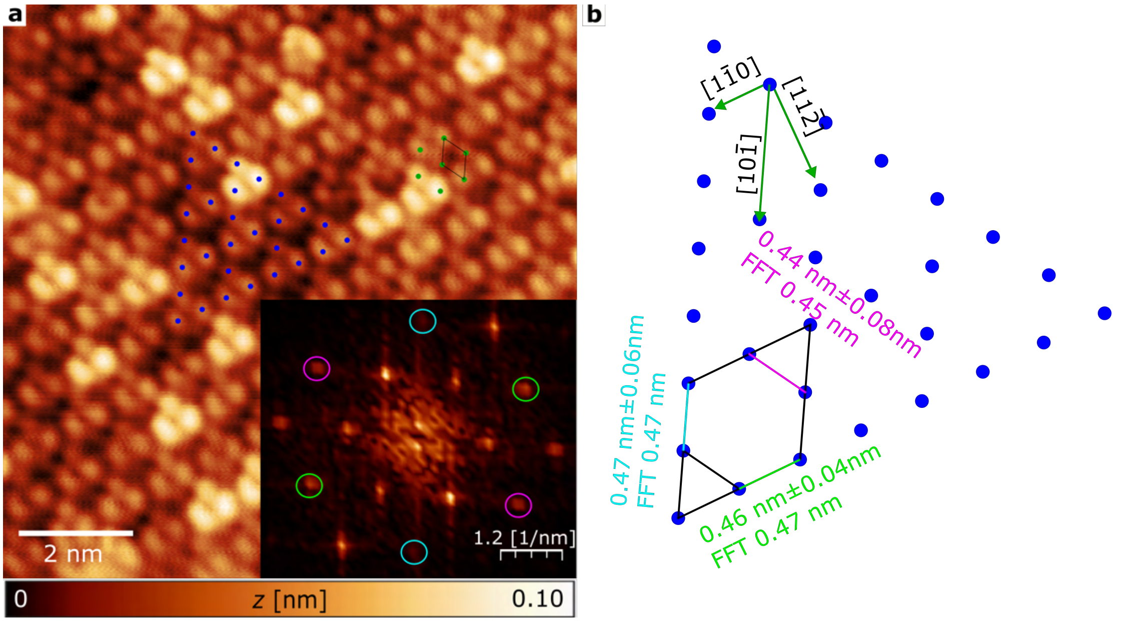

Figure 4.9: In **a** the atomic resolution of Nb(111) shows a surface reconstruction with blue dots marking the positions of some atoms to illustrate the lattice structure, with the unit cell drawn in **b**. In addition, a region where an additional atom is visible in a hexagon is marked with green dots. Shown in the bottom right corner of **a** is the Fourier transform of **a**, with the corresponding distances color-coded and given in **b**. The grid drawn in **a** is shown enlarged in **b** with distances as deduced from the STM data and the FFT. Measurement parameters: **a** $V = 100\,\mathrm{mV}$, $I = 1\,\mathrm{nA}$, $T = 25\,\mathrm{K}$.

The Kagome-like lattice is qualitatively consistent with the theoretical work of Yang et al. [130], who investigated melting mechanisms of Nb(111) planes. Yang showed that Nb(111) should already exhibit an initial activation of subsurface atoms at a temperature of $T \approx 1250\,\mathrm{K}$. He describes this process as premelting, in which the density of the first atomic layers are slightly reduced compared to the layers below.

Another interesting effect can be observed in Fig. 4.10 **a**: some atoms, usually a three-atom combination, appear very high compared to the neighboring atoms, about two times higher (see also the line profile in appendix Fig. A.4). The assumption is that these bright three-atom clusters still have oxygen attached. This assumption can be supported by looking at $\mathrm{d}I/\mathrm{d}V$ images taken at $V = -100\,\mathrm{mV}$ and shown in Fig. 4.10 **b** with the corresponding topography presented in **a**. The three-atom clusters that appear bright in Fig. 4.10 **a** show strongly reduced $\mathrm{d}I/\mathrm{d}V$ values at this energy in **b** indicating a strongly reduced local DOS at this location. However, the missing-atom defect (highlighted with

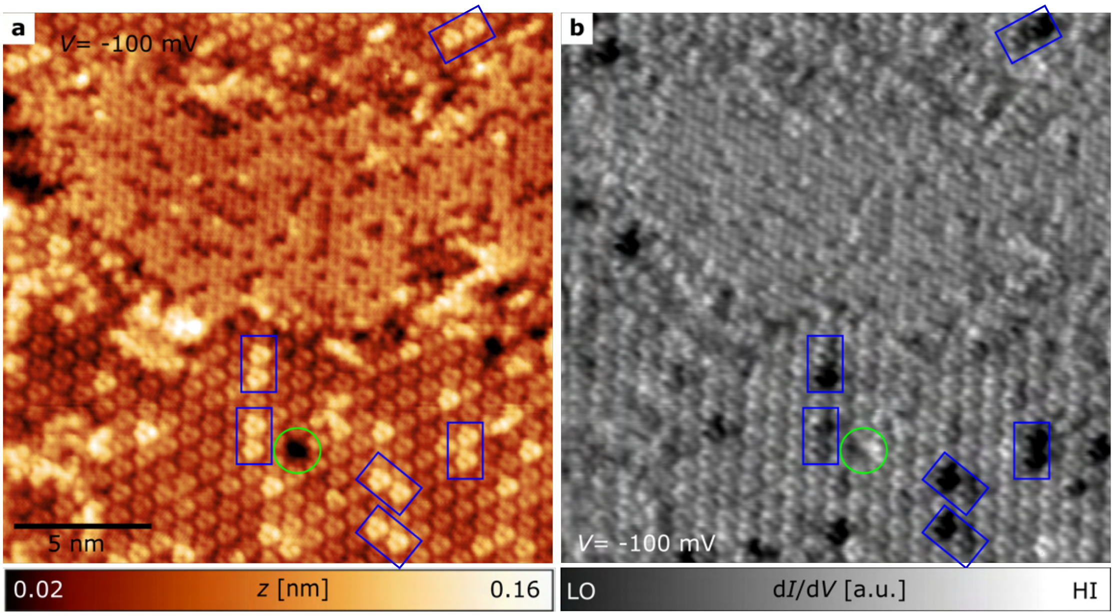

Figure 4.10: In **a** the Kagome-like reconstruction can be seen with the simultaneously recorded $\mathrm{d}I/\mathrm{d}V$ map in **b**, in which two of the bright three atom clusters (framed in blue) show a strongly reduced $\mathrm{d}I/\mathrm{d}V$ value at $V = -100\,\mathrm{mV}$ in contrast to the neighbouring atoms. In addition, there is a defect in the lattice (framed in green) where the $\mathrm{d}I/\mathrm{d}V$ values are larger at this energy. Measurement parameters for **a** and **b**: $V = -100\,\mathrm{mV}$, $I = 1\,\mathrm{nA}$, $T = 25\,\mathrm{K}$.

a green circle), the dense structure (in the upper part of the image) and the rest of the Kagome-like structure clearly show a stronger differential conductance. This strongly suggests that another elemental species is involved or attached to the bright three atoms, which most likely is oxygen.

The last apparent effect that can be examined and described in more detail is the irregular, densely packed structure that is presented (enlarged) in Fig. 4.11 **a**. As can be clearly seen in the figure, a hexagonal lattice can indeed be identified, though with a lot of defects. The determination of the atomic distances from the STM image shown in Fig. 4.11 **a** gives distances that are in the range of the expected lattice spacing of Nb(111) (see Fig. 4.11 **b** and Fig.4.2 **c**). This result suggests that the hexagonal lattice shown in Fig. 4.11 **a** most likely shows the unreconstructed Nb(111) surface at an earlier stage, but was pre-melted by heating and therefore has a lower atomic density compared to the truncated(111) surface of a bcc crystal.

For the investigation of niobium(111), the following can now be summarized: Firstly, a cleaning of the surface without hydrogen treatment, i.e. only by the usual physical treatments (sputtering and annealing) proves to be difficult and results mostly in a facetting of the surface. Secondly, the treatment of the surface with atomic hydrogen results in two types of surfaces, namely reconstructed Nb(111) which exhibits a Kagome-like lattice and an unreconstructed hexagonal Nb(111) lattice with a lot of defects. In both, a lattice spacing that is in the range of the theoretical value of the lattice constant of Nb(111) $a_{\mathrm{Nb}} = 0.467\,\mathrm{nm}$ can be found. These two surfaces most likely represent different stages of premelting, which was theoretically predicted by Yang et al. [130]. Furthermore, these results show for the first time a very good surface quality of Nb(111), i.e. wide terraces with a very low amount of impurities.

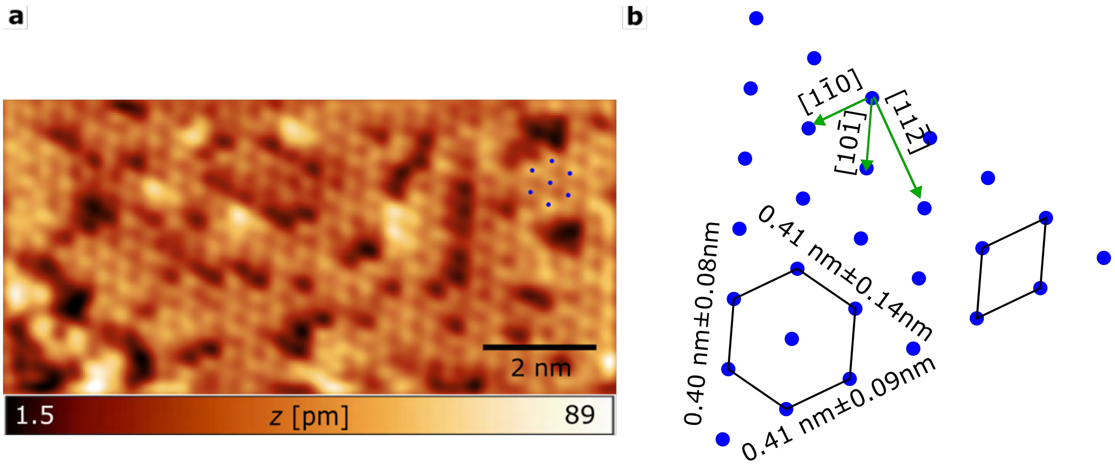

Figure 4.11: Shown in **a** is the hexagonal lattice of Nb(111) (with many defects) with atomic distances given in **b**. The measurement parameters are: $V = -100\,\mathrm{mV}$, $I = 1\,\mathrm{nA}$, $T = 25\,\mathrm{K}$.

4.1.3 Iron Deposition on Niobium (111)

For the next step on the way to the construction of an artificial topological superconductor, according to Sec. 2.4.3, magnetic material must be placed on the substrate. For this purpose, Fe was vapor deposited on the cleaned Nb(111) surface. A temperature of $T \approx 520\,\mathrm{K}$ was chosen such that on the one hand the monolayers will be formed and, on the other hand, the oxygen from the bulk will not diffuse to the surface (compare the temperatures in Sec. 4.1.1). The result is shown in Fig. 4.12. However, as can be clearly seen in Fig. 4.12 on close examination, Fe clusters have formed, presumably due to the open surface of the Kagome lattice.

In parallel to this investigation, the study of Fe/Nb(110) was started in the He-bath STM system (see Sec. 3.1.1), where it was found that the deposition of monolayers of Fe was much easier (see Sec. 4.2). For this reason, the investigation of Fe/Nb(111) was not pursued further and instead the focus was placed on Fe/Nb(110) in the further course of the work.

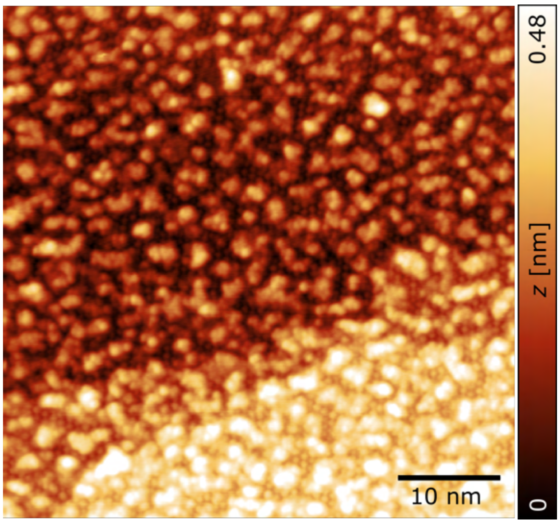

Figure 4.12: An STM image of Fe deposited on a cleaned Nb(111) surface is shown. Despite a deposition temperature of $T \approx 520\,\mathrm{K}$, the iron shows cluster formation. The measurement parameters are given by $V = 500\,\mathrm{mV}$, $I = 50\,\mathrm{pA}$, $T = 25\,\mathrm{K}$.

4.2 Growth of Fe/Nb(110)

In this section, the growth of Fe/Nb(110) is discussed. The sample preparation of Nb(110) has already been described in Sec. 3.2.2 and the preparation procedure of Fe/Nb(110) in Sec. 3.2.3.

The lattice constants play an important role in growing thin films on a substrate. If the difference in lattice constants is large, it is unlikely that the vapor-deposited material adopts the lattice structure of the substrate and thus forms a pseudomorphic growth; instead, it is more likely that the layer will release strain by the formation of reconstructed Fe-monolayer islands. If we compare the lattice constants of iron $a_{\mathrm{Fe}} = 287\,\mathrm{pm}$ with niobium $a_{\mathrm{Nb}} = 330\,\mathrm{pm}$, the mismatch is $\eta = \frac{a_{\mathrm{Fe}} - a_{\mathrm{Nb}}}{a_{\mathrm{Nb}}} = -13.33\%$. This large mismatch compared for example to Fe/W (-9.4%), Fe/Mo (-8.6%), and Fe/V (-5%) [131] can clearly affect the growth behavior of iron monolayers on niobium.

A few growth studies of Fe/Nb(110) and vice versa, were already performed by Wolf et al. [132–134] using STM and by Mougin et al. [131] using reflection high energy electron diffraction and Auger electron spectroscopy. In Wolf's work, however, Nb was not used in form of a single crystal as substrate. Instead Nb was evaporated on buffer layers (Al_2O_3 and W), on which iron was then evaporated. Wolf et al. found that no intermixing of Nb and Fe occurs during evaporation at room temperature, but only when the crystal is heated above $T = 800\,\mathrm{K}$ after depostion. Since no evidence of intermixing [134] is found in this work, as will be shown below, and Fe was only evaporated at RT, it can be assumed that for the following results for Fe/Nb(110) no alloys are present.

STM images of clean Nb(110) with multiple terraces and different coverage of Fe, all in the submonolayer regime, are shown in Fig. 4.13. The shallower islands have a typical height of 250 pm corresponding to one ML. They seem to have arbitrary shapes, i.e. a growth in a particular preferred direction is not observed. The second layer, however, which can be seen in Fig. 4.13 **c** in the form of bright stripes ontop of the ML islands, shows that nucleation starts before the first layer is completely closed and that they are mostly elongated in the $[1\bar{1}0]$-direction. This is in agreement with Köhler et al. [135]. They studied the growth process of Fe/Fe(110) and explained in detail, with the sup-

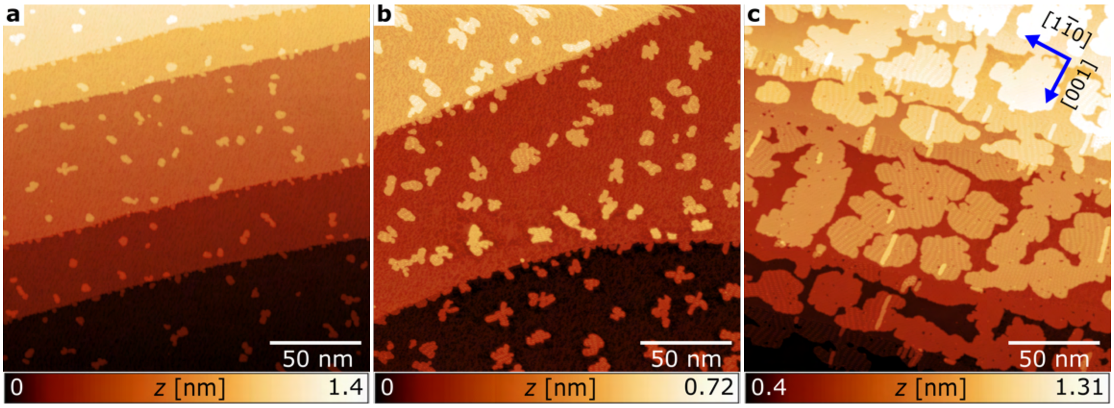

Figure 4.13: STM images of Fe/Nb(110) for **a** 0.06 monolayer, $V = -1\,\mathrm{V}$, $I = 100\,\mathrm{pA}$, $T = 6\,\mathrm{K}$; **b**: 0.2 monolayer, $V = 1\,\mathrm{V}$, $I = 1\,\mathrm{nA}$, $T = 6\,\mathrm{K}$; **c**: 0.7 monolayer, $V = 500\,\mathrm{V}$, $I = 1\,\mathrm{nA}$, $T = 6\,\mathrm{K}$

port of Monte Carlo simulations, why the islands are elongated in the [001] direction: The reason is basically that diffusion is more likely along the [1$\bar{1}$1]-direction than in the [001]-direction, since in the [001]-direction hopping must take place over an on-top position, while this is not true for the [1$\bar{1}$1]-direction. This results in an accumulation at the ⟨111⟩-edges, which again results in elongated stripes along the [1$\bar{1}$0]-direction [135]. This elongated growth along the [001] direction is also reported by Wolf et al. [132]. However, the results differ insofar as Wolf has a very strong island growth (Volmer-Weber formation): a fourth monolayer is already formed, while the first is not yet completely closed [134]. In this work, such growth was observed when the Nb crystal was not flashed high enough so that it still had an oxygen-reconstruction before the deposition of Fe. Fig. 4.14 **a** shows an STM image of a thin film of Fe grown on Nb(110) after the crystal was heated with a reduced power of only 350 W instead of 510 W where the latter is the necessary power for clean niobium. Also here, as in Wolf's work, the first ML is not yet fully closed, while the second ML and third ML have already started to grow. The islands themselves are also quite small (few nm^2), unlike the islands in Fig. 4.13 **c** on which no third or fourth monolayer islands can be seen. Increasing the Fe amount on the oxygen-reconstructed Nb surface leads to narrow multilayers elongated in the [001]-direction, which can be seen in Fig. 4.14 **b**. The second layer also has a reconstruction which is very characteristic and was observed in this work as well as in [132, 134]. It is therefore reasonable to assume that Nb in [132, 134] was not sufficiently clean and therefore the rough island growth was observed. Wolf et al. also reports problems with oxygen contamination, although Nb was vapor-deposited on a buffer layer. They were even confronted with the first reconstruction of oxygen described in [115] which can be identified if the crystal is heated only to 2073 K.

Based on the corresponding results and findings, it is assumed that the preparations shown in Fig. 4.13 **a** - **c** are pure unalloyed iron grown on Nb(110) which is free from the oxygen-reconstruction. Taking a closer look at the individual islands now, we can identify further different reconstructions, which we will discuss in more detail in the following Chapter 4.3.

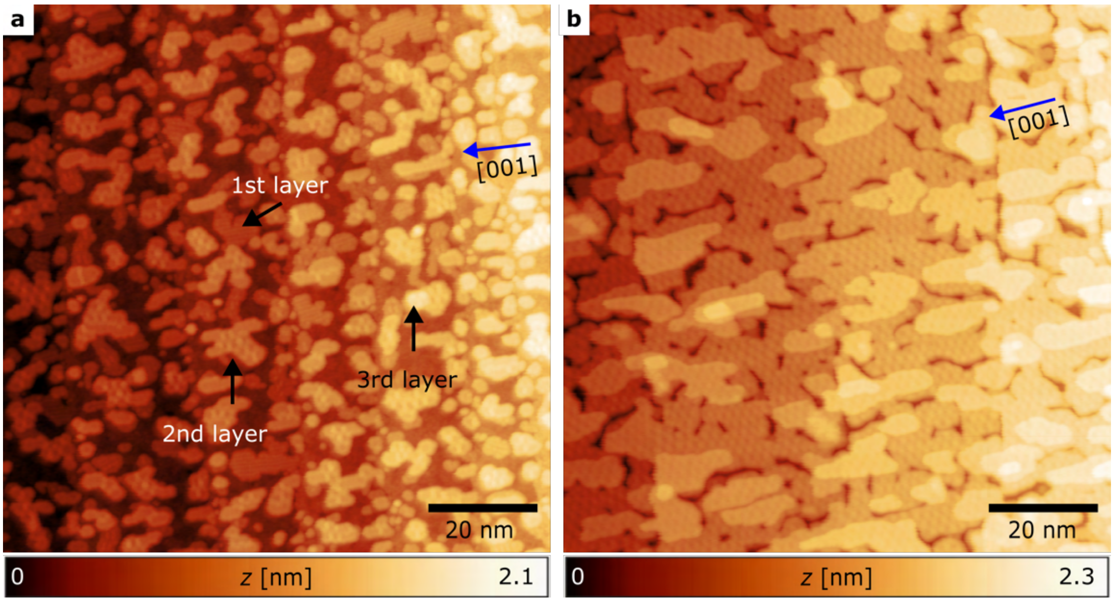

Figure 4.14: **a** STM image showing a thin film of Fe grown on Nb(110) after the crystal was heated with a reduced power of only 350 W ($V = 300\,\mathrm{mV}$, $I = 300\,\mathrm{pA}$, and $T = 4.5\,\mathrm{K}$). **b** An extended evaporation time leads to narrow multilayers exhibiting a reconstruction pattern ($V = 400\,\mathrm{mV}$, $I = 500\,\mathrm{pA}$, and $T = 4.5\,\mathrm{K}$).

4.3 Reconstructions of Fe ML on Nb(110)

As discussed in Sec. 4.2, due to large lattice mismatch, a significant strain can occur in the Fe lattice which can lead to reconstructions. Indeed, the data show mainly islands with three different reconstructions, referred to as type I, type II, and type III, which can be seen in Fig. 4.15 **a**. The reconstructions can occur in separated islands, but also islands where all three reconstructions transition from one to the other can be observed (as can be seen in Fig. 4.15 **a**). Moreover, it can be concluded that the Fe islands do not simply maintain the bulk Fe lattice structure without any adaptation to Nb(110), since otherwise only one moire pattern should be found. In the following, these rather complicated structures are described in more detail, starting with structure type I.

The islands with the **type I** reconstruction show many short stripe-like protrusions, which exhibit an apparent height of $70 - 80$ pm compared to the flat part of the reconstruction (see Fig. 4.15 **b**) and with an average length of about 1 to 2 nm. They are mostly regularly spaced at intervals of 1.14 nm ± 0.12 nm in the short direction and of 3.16 nm ± 0.61 nm in the long direction. The directions of repetition can be observed in [001], but also deviating from [001] as shown in Fig. 4.16 **a** (lower right). An atomic resolution image was taken, showing the niobium lattice and the reconstruction (see Fig. 4.16 **b**). A lattice structure can be seen on the flat area revealing a rectangular "unit cell" indicated in green in Fig. 4.16 **c**, showing that the long side of the unit cell is parallel to the long side of the stripe-like protrusions. The lattice extends similarly to Nb(110) in the [001] and $[1\bar{1}0]$ directions with about one degree of deviation and in the $[1\bar{1}1]$ direction with a deviation of about 10° (Fig. 4.16 **b**). In addition, the following distances were measured for the lattice structure: $0.47\,\mathrm{nm} \pm 0.05\,\mathrm{nm}$ in [001] direction ($0.33\,\mathrm{nm}$ for Nb), $0.48\,\mathrm{nm} \pm 0.06\,\mathrm{nm}$ in $[1\bar{1}1]$ direction ($0.57\,\mathrm{nm}$ for Nb) and

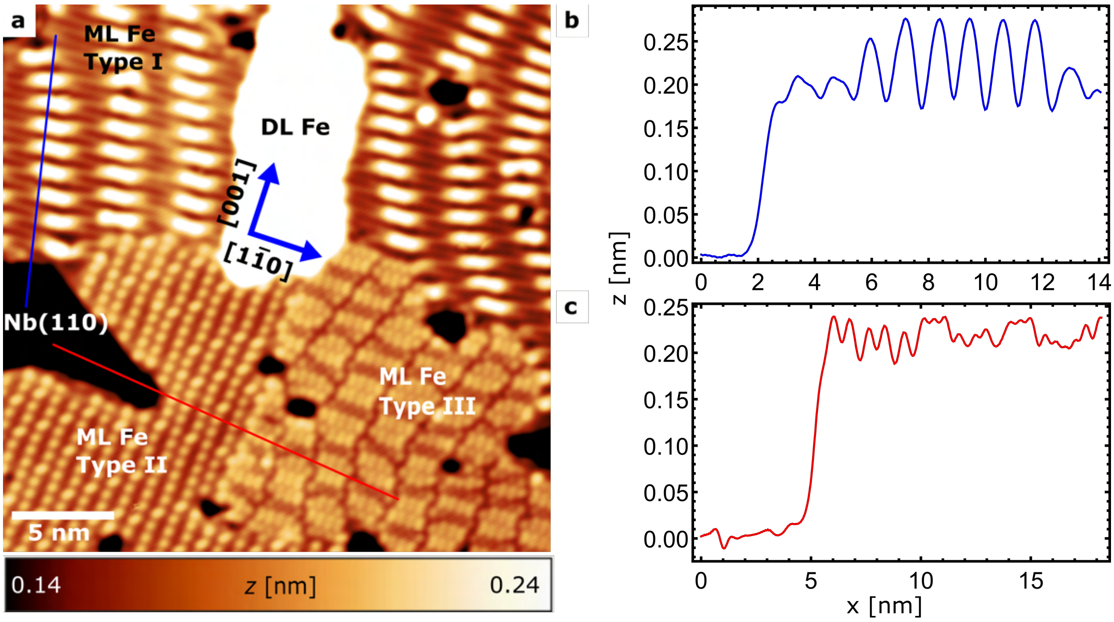

Figure 4.15: **a** STM image of ML Fe islands having the three distinct reconstructions I, II, III ($V = -10\,\mathrm{mV}$, $I = 4\,\mathrm{nA}$, $T = 6.5\,\mathrm{K}$). Furthermore, a DL Fe island can be identified as a bright stripe. **b** and **c** profile lines taken from **a** (along the lines marked in blue and red), showing a typical height of the islands at about 0.23 nm.

0.71 nm ± 0.17 nm in [1$\bar{1}$0] direction[1] (0.47 nm for Nb). Furthermore, the reconstructions span a large number of substrate unit cells on a roughly 8 × 16 superlattice (with respect to [001] × [1$\bar{1}$0]). The typical height of the Fe monolayer with the reconstruction of type I is about 0.23 nm, as can be seen in Fig. 4.15 **b**.

The iron reconstruction of **type II** is the only one that shows a uniform long-range order, as shown in Fig. 4.17 **a** and Fig. 4.15 **a**. Since the tip used in these measurements achieved atomic resolution on the niobium lattice, it is natural to assume atomic resolution here as well. However, the apparent sizes and spacings of the Fe atoms are surprisingly large. If one nevertheless assumes an atomic resolution, then it exhibits a (2 × 2) superlattice spanning about 4 substrate unit cells, but with every second atom missing along the [001] and the [1$\bar{1}$0] directions, as shown in Fig. 4.17 **a**. The superlattice spacings measured over several rows are 0.69 nm ± 0.06 nm along the [001] direction and 0.84 nm ± 0.07 nm along the [1$\bar{1}$0] direction[2]. Furthermore, it can be observed at irregular intervals that the lattice rows in the [1$\bar{1}$1] direction have different apparent heights. A line profile drawn across type II and type III Fe monolayers shows a typical island height of 0.23 nm (see Fig. 4.15 **c**).

The last reconstruction of **type III** shows only short-range order. An enlargement

---

[1] Distance measurements were made after calibrating the STM on the niobium lattice using the method described in appendix A.4.1.2, with 61, 43, and 12 distances measured and averaged (in [001], [1$\bar{1}$1] and [1$\bar{1}$0] directions, respectively). A distance measurement using a Fourier transform did not provide a robust result.

[2] Distance measurements were also made using the method described in appendix A.4.1.2, with 136 distances measured in [001] direction and 127 distances measured in [1$\bar{1}$0] direction. In addition, the structure of the lattice is suitable for a distance measurement using a Fourier transform, which also yielded distances of 0.69 nm in [001] direction and 0.84 nm in [1$\bar{1}$0] direction (see Appendix Fig. A.6).

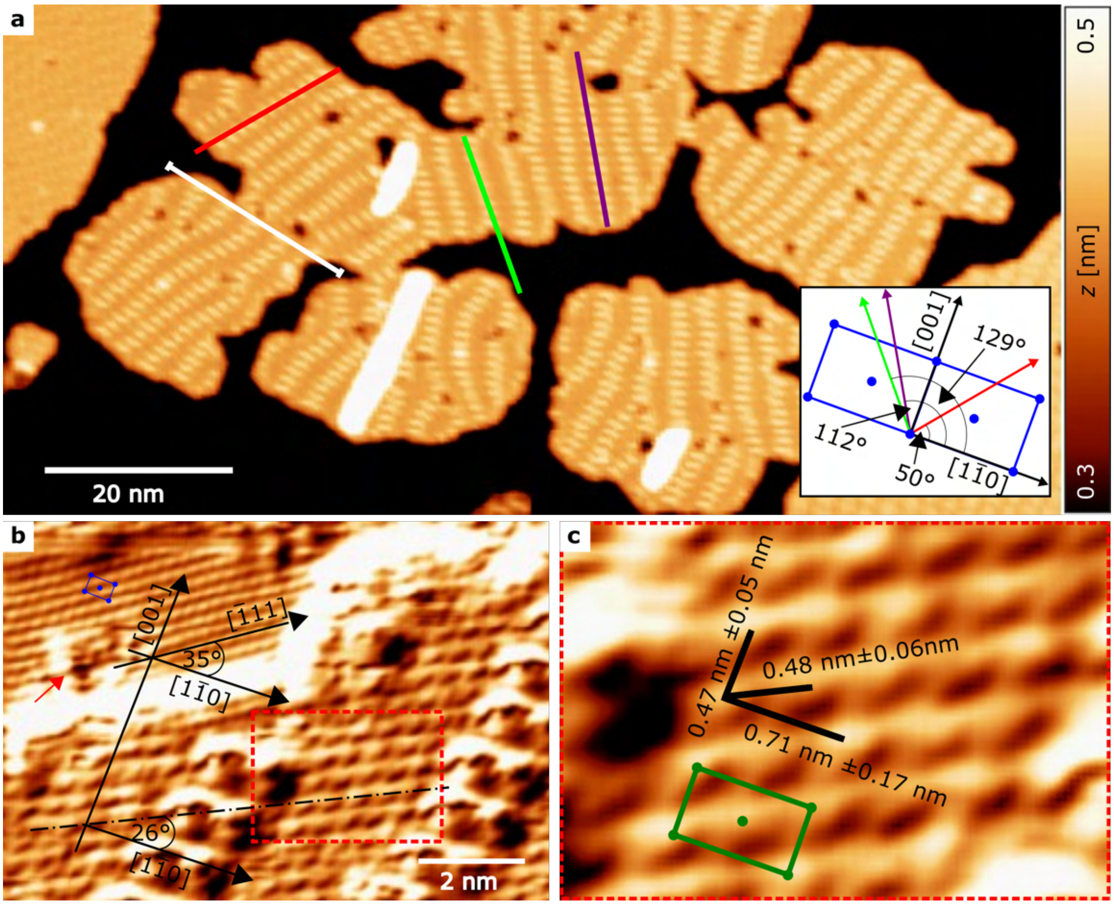

Figure 4.16: In **a** the reconstructed islands of type I are shown with their typical stripe-like protrusions extending at regular intervals in different directions (lower right panel). Shown in **b** is an atomically resolved STM image of Nb(110) and of the reconstruction of type I (with the Nb unit cell in blue). For better visibility of the structures the image was filtered using matrix convolution. The Fe lattice extends similarly to Nb(110) in the [001] and [1$\bar{1}$0] directions with about one degree of deviation and in the [1$\bar{1}$1] direction with a deviation of about 10° (dashed line). In the region indicated by a red arrow, oxygen contamination is most likely attached to Nb. In **c** a zoom-in of the flat area in **b** framed by a dotted red rectangle, with the measured distances of the lattice structure is shown. Measurement parameters for **a**: $V = 500\,\mathrm{V}$, $I = 1\,\mathrm{nA}$, $T = 6.5\,\mathrm{K}$; **b**: $V = -10\,\mathrm{mV}$, $I = 5\,\mathrm{nA}$, $T = 6.5\,\mathrm{K}$.

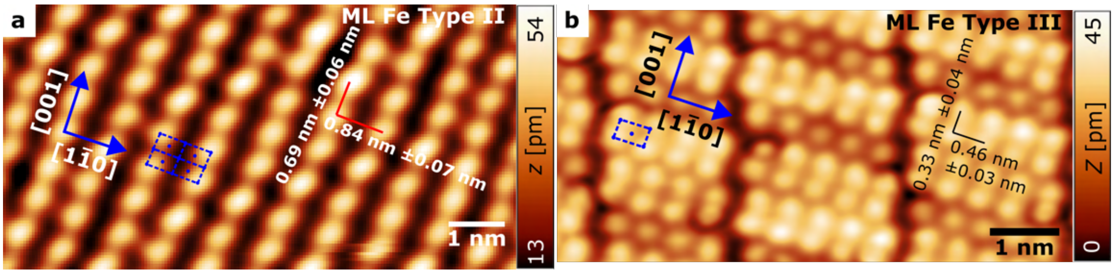

Figure 4.17: Atomically resolved STM images of type II **a** and type III **b** Fe ML reconstructions with the Nb(110) unit cell shown in blue. Measurement parameters for **a**: $V = -10\,\mathrm{mV}$, $I = 7\,\mathrm{nA}$,$T = 6.5\,\mathrm{K}$; **b**: $V = -5\,\mathrm{mV}$, $I = 10\,\mathrm{nA}$, $T = 6.5\,\mathrm{K}$.

can be seen in Fig. 4.17 **b**. For this rather irregular structure (see also Fig. 4.15 **a**), it is difficult to define a unit cell. However, it can be noted that in the $[1\bar{1}0]$ direction, a repetition can be observed after 3 to 4 substrate unit cells, which are then interrupted by reconstruction lines along the [001] direction. However, no clear repetition pattern can be seen along the [001] direction. It is also noticeable that individual atomic rows along the $[1\bar{1}0]$ direction have an apparently lower height. The measured atomic distances in the [001] direction are $0.33\,\mathrm{nm} \pm 0.04\,\mathrm{nm}$ and in the $[1\bar{1}0]$ direction $0.46\,\mathrm{nm} \pm 0.03\,\mathrm{nm}$[3].

---

[3] The method described in appendix A.4.1.2 was used again with 161 measured distances in $[1\bar{1}0]$ direction and 44 in [001] direction. A distance measurement using a Fourier transform did not provide a robust result.

4.4 Investigations of the Magnetism of Fe/Nb(110)

Having described the individual structures, the magnetic properties of the Fe islands will now be characterized in the next sections. We will start with the magnetic characterization of the tip, followed by the magnetic properties of the monolayer islands. The extraction of data and data processing of the $\mathrm{d}I/\mathrm{d}V$ maps is described in appendix A.4.2. The data processing for spin asymmetry maps is described in A.4.3.

4.4.1 Characterization of the Magnetic Tip

In the following, the behavior of the magnetic tip (namely tip 1) as a function of an out-of-plane applied B-field will be explained and shown exemplarily.

As described in Sec. 3.2.1, the tip is softly magnetized by dipping the tip into Fe islands and its magnetization aligns to the external field at a few hundred mT. In contrast, it can be assumed that the magnetization of the Fe double layers is more stable against thermal fluctuations and external magnetic fields, due to the increased amount of magnetic material. In particular, this means that the magnetization of the tip will be oriented along an external magnetic field at significantly lower field strengths, compared to the Fe double layer. Therefore, the characterization of the tip was performed on a double layer of Fe (see Fig. 4.18 **a**).

The behavior of the magnetization of the tip can be studied especially by considering the magnetic hysteresis loops, shown in Fig. 4.18 **b**. For this hysteresis loop, the data were extracted from the area enclosed in blue in Fig. 4.18 **c** for each B-field dependent $\mathrm{d}I/\mathrm{d}V$ map. The data were then averaged and plotted as a function of the B-field[4] (see Fig. 4.18 **b**).

It can be observed that the magnetization of the tip gradually aligns along the direction of the external magnetic field as the magnitude of the field strength increases. This can be seen at the beginning of the loop in the range from $B_z = 0\,\mathrm{T}$ to $B_z = -0.375\,\mathrm{T}$, (along the direction of the arrow in Fig. 4.18 **b**), by the decrease in the $\mathrm{d}I/\mathrm{d}V$ values, until saturation is reached at about $B_z = -0.5\,\mathrm{T}$. If the magnetic field is then increased from $B_z = -1\,\mathrm{T}$ to $B_z = 0.5\,\mathrm{T}$, a reorientation of the magnetization of the tip takes place from downwards to upwards magnetization (increase of the $\mathrm{d}I/\mathrm{d}V$ signal). The

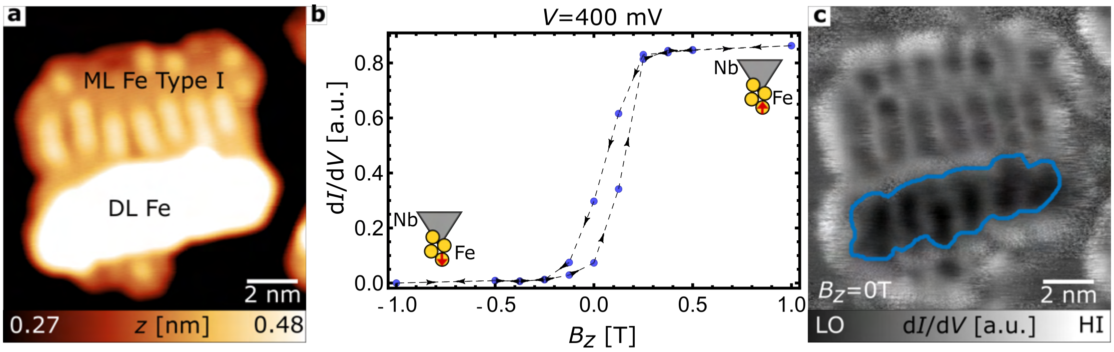

Figure 4.18: In **a**, an STM image of a type I island with a DL is shown where the tip characterization was performed. **b** Hysteresis loop of the tip showing a coercivity of approximately $B_z \approx \pm 0.375\,\mathrm{T}$. **c** One exemplary $\mathrm{d}I/\mathrm{d}V$ map which shows the area inside blue line that has been evaluated in order to extract the hysteresis loop. Measurement parameters: $B_z = 0\,\mathrm{T}$, $V = 400\,\mathrm{mV}$, $V_{\mathrm{mod}} = 10\,\mathrm{mV}$, $f = 1197\,\mathrm{Hz}$, $I = 1\,\mathrm{nA}$ and $T = 4.5\,\mathrm{K}$.

---

[4] Note that in this hysteresis loop the switching of the island is not visible. To see the switching of the Fe DL, a stronger magnetic field is required (see Fig. 4.31 **b**).

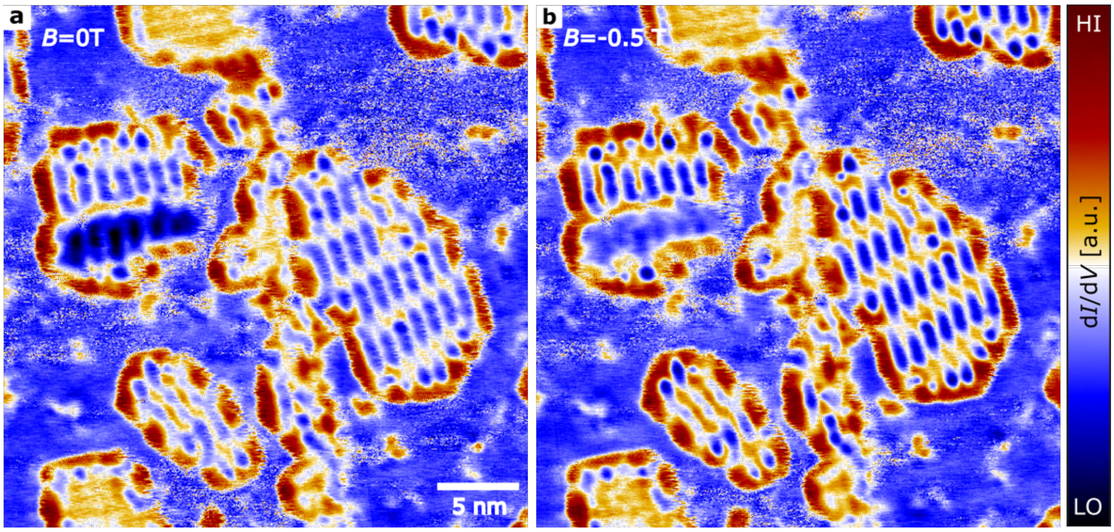

Figure 4.19: dI/dV maps of the loop at $B_z = 0\,\mathrm{T}$ (**a**) and $B_z = -0.5\,\mathrm{T}$ (**b**) revealing signal changes due to field dependence of the tip magnetization. Measurement parameters: $V = 400\,\mathrm{mV}$, $V_{\mathrm{mod}} = 10\,\mathrm{mV}$, $f = 1197\,\mathrm{Hz}$, $I = 1\,\mathrm{nA}$ and $T = 4.5\,\mathrm{K}$.

resulting hysteresis curve in Fig. 4.18 **b** shows the typical narrow magnetization curve of a soft magnet. Since an unknown amount of Fe with unknown crystal structure and shape is taken up with the tip by dipping the tip into the Fe islands, it is not known which anisotropy axes are present. However, one possible explanation of the measured hysteresis curve would be an anisotropy axis with a fraction in z-direction, as well as perpendicular to it (compare with the simulation result in Fig. 4.24 **a**).

To support the previous conclusions, dI/dV maps at $B_z = 0\,\mathrm{T}$ can be compared with dI/dV maps taken at $B_z = -0.5\,\mathrm{T}$ (see Fig. 4.19 **a**, **b**). It can be observed that a change in the dI/dV signal occurs on all islands regardless of the type, thickness and their size, except for the type II (orange) island. In contrast, assuming a constant tip magnetization for this magnetic field region implies that all islands switch their magnetization at a similar, very small coercive field, which is very unlikely. Thus, it can be concluded that this magnetic tip 1 has a coercivity of about $|B_{\mathrm{c}}^{\mathrm{tip}}| \sim 0.375\,\mathrm{T}$.

4.4.2 Local Spin-Resolved SP-STS on Fe/Nb(110)

In order to determine the bias voltage ranges with a considerable spin contrast for the SP-STM measurements, point spectra have been taken in the range from -1 V to 1 V at different positions of the islands (Fig. 4.20, 4.21, 4.22 **a**) and for different magnetic fields (Fig. 4.20, 4.21, 4.22 **b** - **c**). For the type I ML, a considerable spin polarization can be detected in the point spectroscopy for position 1 approximately from $V = -500$ mV to $V = 700$ mV and for position 2 from $V = -650$ mV to $V = 900$ mV. To achieve maximum spin contrast in the spin-resolved differential tunneling conductance, the voltage with the strongest deviation of the curves was used for the dI/dV maps. The voltages subsequently selected for dI/dV maps for the type I ML were -400 mV, 200 mV, and 400 mV (gray dashed lines in Fig. 4.20 **b** - **c**). Also a contrast reversal between the ranges of $V = -400$ mV to $V = 0$ mV and $V = 330$ mV to $V = 530$ mV was observed between the stripe (position 1) and flat areas (position 2) of the reconstruction (see Fig. 4.20 **a**). This is most likely due to an inversion of the vacuum spin polarization above the stripes with respect to the flat regions, as this effect is already known in the literature for other systems [136], but not due to any kind of alternating domain or helical spin structure.

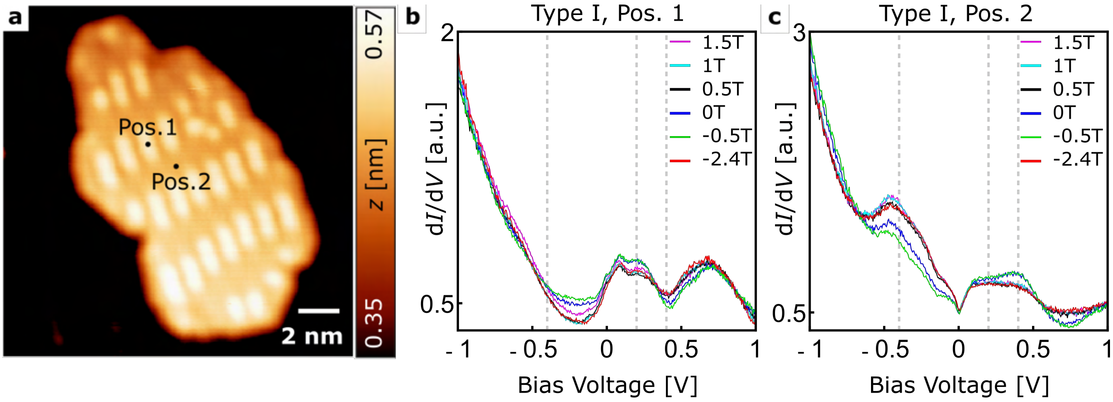

Figure 4.20: **a** STM image of a type I Fe ML island, indicating the positions where point spectra have been taken ($V = 400$ mV, $I = 1$ nA and $T = 4.5$ K). In **b** - **c** point spectra can be seen, taken for the magnetic field values indicated in the legend on the positions marked in **a**. Gray dashed lines, see text. Measurement parameters: $I_{\text{stab}} = 500$ pA, $V_{\text{stab}} = 1$ V, $V_{\text{mod}} = 10$ mV, $f = 1197$ Hz and $T = 4.5$ K.

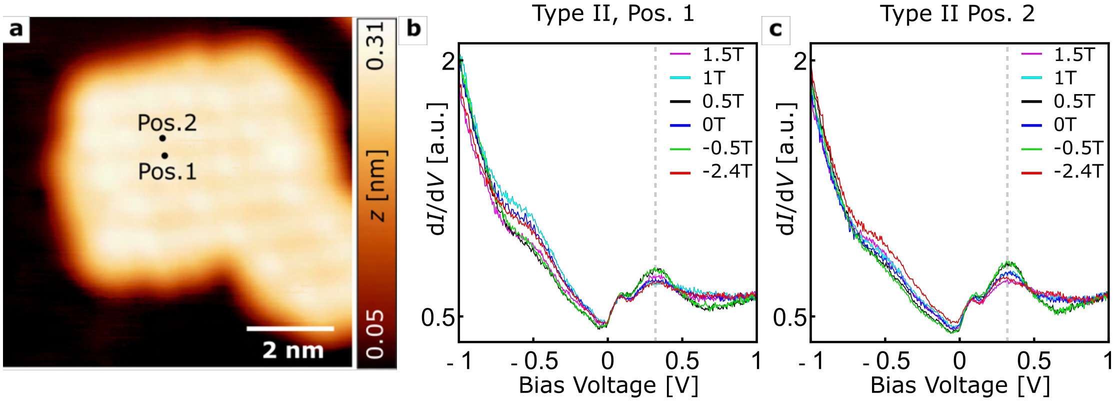

Figure 4.21: **a** STM image of type II island indicating the positions where point spectra have been taken ($V = 400$ mV and $I = 1$ nA). In **b** - **c** point spectra can be seen, taken for the magnetic field values indicated in the legend on the positions marked in **a**. Gray dashed lines, see text. Measurement parameters: $I_{\text{stab}} = 500$ pA, $V_{\text{stab}} = 1$ V, $V_{\text{mod}} = 10$ mV, $f = 1197$ Hz and $T = 4.5$ K.

This will be further discussed in Sec. 4.4.3.
For the type II ML a spin polarization for position 1 and 2 (see Fig. 4.21 **a**) can be detected ranging approximately from $V = -700\,\mathrm{mV}$ to $V = -100\,\mathrm{mV}$ and from $V = 150\,\mathrm{mV}$ to $V = 860\,\mathrm{mV}$ (see Fig. 4.21 **b** - **c**). The voltage that has been selected for the $\mathrm{d}I/\mathrm{d}V$ maps was 320 mV (gray dashed lines in Fig. 4.21 **b** - **c**)).

The point spectra for type III ML (Fig. 4.22 **b** - **c**)) hardly show any magnetic-field dependent contrast in the entire bias and magnetic field range, except for a region in the small magnetic field range of $B_z < 0.5\,\mathrm{T}$. The voltage selected for $\mathrm{d}I/\mathrm{d}V$ maps in this case was 375 mV (gray dashed lines in Fig. 4.22 **b** - **c**)).

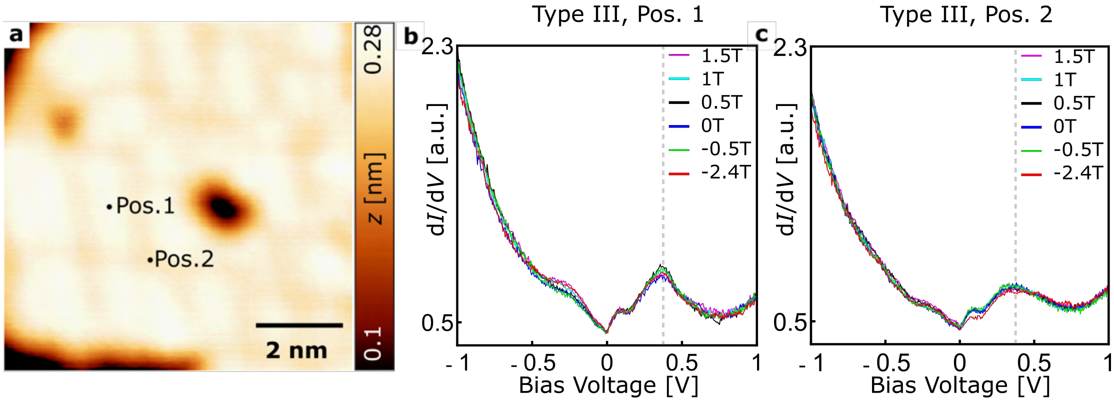

Figure 4.22: **a** STM image of a type III ML island indicating the positions where point spectra have been taken ($V = 375\,\mathrm{mV}$ and $I = 1\,\mathrm{nA}$). In **b** - **c** point spectra are shown, taken for the magnetic field values indicated in the legend on the positions marked in **a**. Gray dashed lines, see text. Measurement parameters: $I_{\mathrm{stab}} = 500\,\mathrm{pA}$, $V_{\mathrm{stab}} = 1\,\mathrm{V}$, $V_{\mathrm{mod}} = 10\,\mathrm{mV}$, $f = 1197\,\mathrm{Hz}$ and $T = 4.5\,\mathrm{K}$.

4.4.3 Hysteresis Loops and Spin Asymmetry Maps of the Fe Islands

After showing in Sec. 4.4.1 how the magnetic property of a tip can be determined and in Sec. 4.4.2 at which voltage the Fe islands show the strongest spin polarization, the measured magnetic hysteresis loops (Sec. A.4.2) and spin asymmetry maps (Sec. A.4.3) of the islands will be presented and discussed next.

4.4.3.1 Type I

Following the results in Sec. 4.4.2, magnetic measurements of an island of type I were performed at $V = -400\,\mathrm{mV}$, $V = 200\,\mathrm{mV}$, and $V = 400\,\mathrm{mV}$. We will first consider the measurements taken at $V = 400\,\mathrm{mV}$.
For type I, the flat and stripe areas were examined separately. The data taken from the flat areas show a butterfly-like hysteresis loop, which can be seen in Fig. 4.23 **b**. Along the direction of the arrows an increasing $\mathrm{d}I/\mathrm{d}V$ signal can be measured between $B_z = 0\,\mathrm{T}$ and $B_z = -0.5\,\mathrm{T}$ indicating that the tip aligns along $-B_z$ (down) direction, while the island maintains a constant magnetization until $B_z = -2\,\mathrm{T}$. This is also schematically sketched in panel 1 of Fig. 4.23 **c**. An abrupt decrease in the $\mathrm{d}I/\mathrm{d}V$ signal is observed between $B_z = -2\,\mathrm{T}$ and $B_z = -2.4\,\mathrm{T}$. Since the tip has already reached its saturation magnetization (see Sec. 4.4.1), the change can be explained by the fact that in this B-field region the magnetization of the island aligns along the external magnetic field, i.e. down (panels 1 and 2 of Fig. 4.23 **b**, **c**). If the external B-field is now increased, an

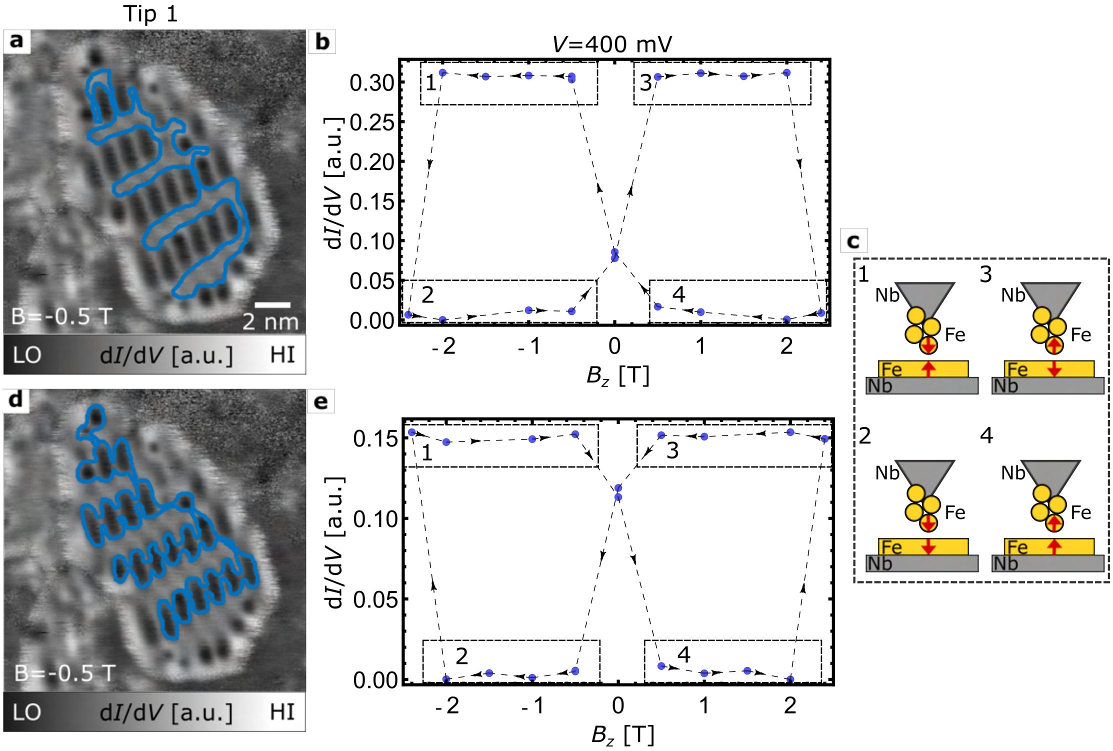

Figure 4.23: In **a** and **d**, the first $\mathrm{d}I/\mathrm{d}V$ maps of the loop are shown as an example, where the data for the blue outlined area is averaged and plotted as a function of the B-field. In **b** and **e** the resulting hysteresis loops are shown while **c** shows an illustrative sketch of the determined magnetization of the tip and the type I Fe ML island for different parts of the hysteresis loop, as indicated by the corresponding numbers in **b** and **e**. Measurement parameters: $I = 1\,\mathrm{nA}$, $V = 400\,\mathrm{mV}$, $V_{\mathrm{mod}} = 10\,\mathrm{mV}$, $f = 1197\,\mathrm{Hz}$, $T = 4.5\,\mathrm{K}$ and $B_z = -0.5\,\mathrm{T}$.

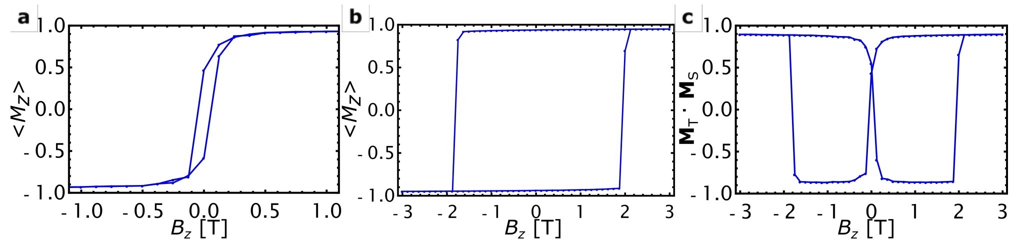

Figure 4.24: In **a** and **b** hysteresis curves from simulation calculations are shown (see Sec. 4.4.4). In **a** the averaged magnetization in z-direction is shown for a $5 \times 5 \times 5$ bcc lattice, which is supposed to represent the magnetization of the tip. An exchange interaction of $J = 2\,\mathrm{mV}$ was chosen and an anisotropy, which also has a significant in-plane contribution, with $|K| = 0.0125\,\mathrm{mV}$ and $\mathbf{e}_K = (0.8, 0, 0.6)^T$. In **b**, again the averaged magnetization in z-direction is shown for a 2D (20×20) triangular lattice, with $J = 2\,\mathrm{mV}$ and $K_z = 0.2\,\mathrm{mV}$. The external magnetic field was applied in the z-direction in both cases and varied from -3 T to 3 T in 0.125 T steps. In **c** the scalar product of the magnetization vectors from **a** and **b** is shown.

increase in the dI/dV signal is observed between $B_z = -0.5\,$T and $B_z = 0.5\,$T as the tip reorients along B_z, i.e., becoming upwards magnetized while the islands still show a downwards magnetization (panels 2 and 3 of Figs. 4.23 **b**, **c**). Between $B_z = 2\,$T and $B_z = 2.4\,$T the island flips its magnetization along the upwards direction, which is again indicated by a decrease in the dI/dV signal (panels 3 and 4 of Fig. 4.23 **b** and **c**). Thus, this magnetic behavior of the island strongly suggests a single-domain ferromagnetic island with an anisotropy axis in z-direction.

This conclusion is supported by simulations (which are explained in detail in Sec. 4.4.4) as can be seen in Fig. 4.24. In Fig. 4.24 **a** a simulation is shown which mimics the magnetization of the tip (compare to Fig. 4.18 **b**) and in **b** a simulation of a magnetic triangular lattice is shown, which has a ferromagnetic monodomain magnetization with a coercivity of about 2 T. In Fig. 4.18 **c** the scalar product of the magnetization vectors from Fig. 4.18 **a** and Fig. 4.18 **b** is shown, which is proportional to the measured differential conductance dI/dV according to relation (2.18). If we now compare Fig. 4.24 **c** with Fig. 4.23 **b** (and **e**), it is easy to see that the same qualitative curve is obtained, supporting the conclusion of a monodomain ferromagnetic island.

If we now consider the data taken from the stripe areas in Fig. 4.23 **d** and **e**, the same behavior as for the flat area in Fig. 4.23 **b** can be observed, only with an inverted spin contrast. One might jump to the conclusion that this change in the sign of the spin polarization could be due to a reversal of the local magnetization between the flat and stripe regions, e.g., due to very small antiparallel domains. However, such domains should increase (decrease) in size with increasing (decreasing) magnetic field if the domains are aligned along (against) the B-field, which was not observed (see the complete loop in Appendix A.5 Fig. A.7). In case of a non-collinear spin structure, using a soft magnetic tip as the one in the present experiment, we would expect to observe lateral shifts of the maxima and minima of the dI/dV values measured across the flat and stripe regions as a function of the magnetic field [137]. However, for the entire magnetization curve, none of such lateral shifts are observed, as can be seen in Fig. 4.25 **b** and **c**.

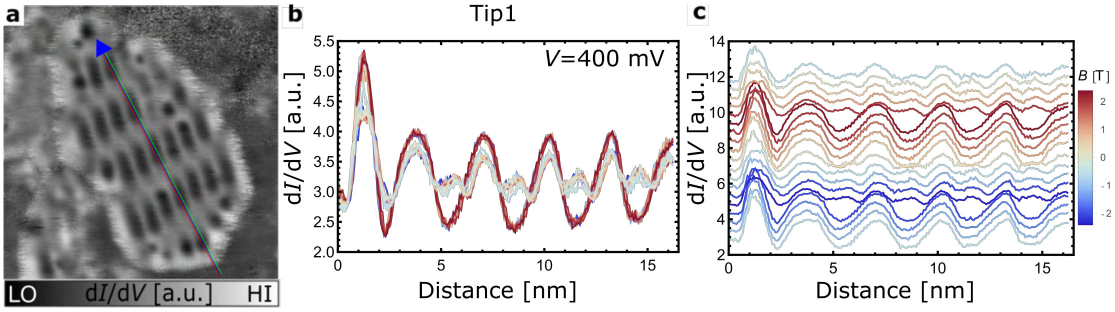

Figure 4.25: **a** dI/dV map of a type I ML island showing the lines and arrow along which the dI/dV line profiles in **b** and **c** have been extracted and averaged. **b** and **c** show dI/dV line profiles along the lines in **a** plotted in normal and waterfall fashion, respectively, from the dI/dV maps recorded during a hysteresis loop at the external magnetic field values given by the color scale on the right. Each dI/dV line profile is an average of three individual profiles positioned parallel, side by side (green, blue and red lines in **a**). Measurement parameters **a**: $I = 1\,$nA, $V = 400\,$mV, $V_{\mathrm{mod}} = 10\,$mV, $f = 1197\,$Hz, $T = 4.5\,$K and $B_z = -0.5\,$T.

Moreover, with two other different magnetic tips (tip 2 and tip 3), even though the magnetic behavior of the tips (at small fields $|B| < 1$ T) cannot be interpreted unambiguously, the switching behavior between 2 T and 2.4 T was also detected for different islands and sizes, which can be seen in Appendix A.5 Fig. A.8 **a** - **e**. Furthermore, no spin inversion was measured with the tip 2 (see Fig. 4.26 **a** - **d**), which is also particularly

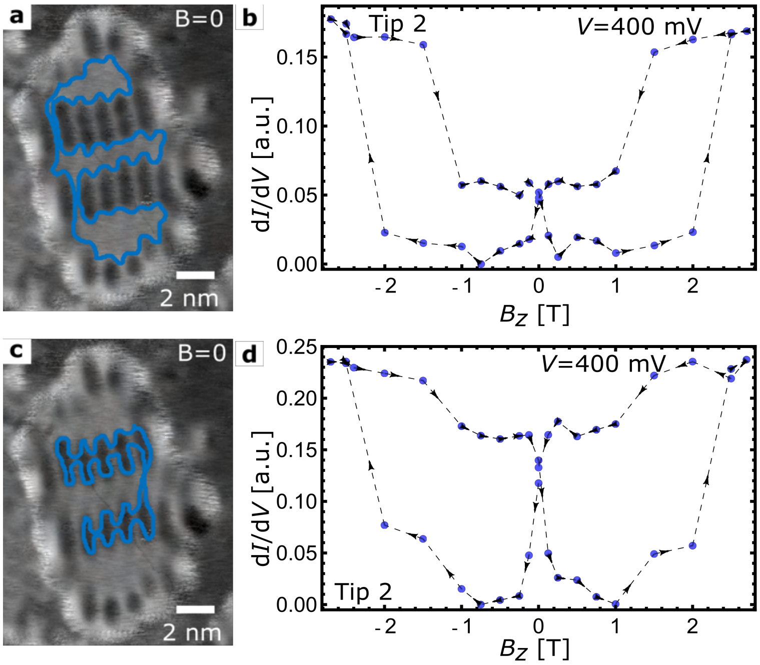

Figure 4.26: Hysteresis curves with additional magnetic tip 2 measured on the flat (**a**, **b**) and on the stripe regions (**c**, **d**). The switching behavior of the islands can also be observed here between $|B_z| = 2\,\mathrm{T}$ and $|B_z| = 2.4\,\mathrm{T}$. Furthermore, no inversion of spin polarization was detected with this tip 2. Measurement parameters are: $I = 1\,\mathrm{nA}$, $V = 400\,\mathrm{mV}$, $V_{\mathrm{mod}} = 10\,\mathrm{mV}$, $f = 1197\,\mathrm{Hz}$, $T = 4.5\,\mathrm{K}$ and $B_z = 0\,\mathrm{T}$.

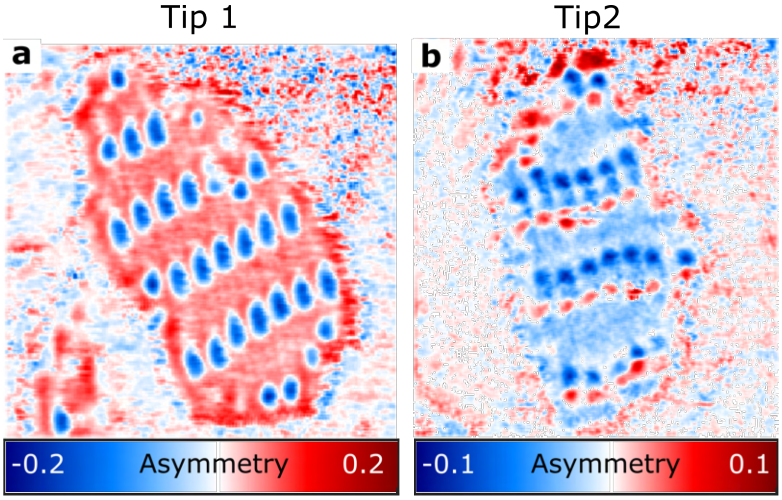

Figure 4.27: **a** - **b** Spin asymmetry maps ($B_{z_1} = -2\,\mathrm{T}$, $B_{z_2} = +2\,\mathrm{T}$) of Fe ML reconstructions type I, taken with tip 1 and tip 2. There is no visible spin inversion for tip 2 between the flat and stripe regions. Measurement parameters **a** and **b**: $I = 1\,\mathrm{nA}$, $V_{\mathrm{mod}} = 10\,\mathrm{mV}$, $V = 400\,\mathrm{mV}$, $f = 1197\,\mathrm{Hz}$ and $T = 4.5\,\mathrm{K}$.

clearly visible in the spin asymmetry map (see Fig. 4.26 **a** and **b**) and strengthens the hypothesis that the islands are out-of-plane monodomain ferromagnetic.
The hysteresis measurements at $V = 200\,\mathrm{mV}$ and at $V = -400\,\mathrm{mV}$ (see Appendix A.5 Fig. A.9) reproduce the hysteresis measured at $V = 400\,\mathrm{mV}$, except that no inversion of spin polarization between the flat and stripe regions is seen at $V = 200\,\mathrm{mV}$, which is also evident in the STS data from Sec. 4.4.2.
It can be summarized that the data presented in this section support the conclusion that the type I Fe ML exhibits a single domain out-of-plane ferromagnetic spin-order with a coercive field of $2.2\,\mathrm{T} \pm 0.2\,\mathrm{T}$, and that the sign reversal (as shown in the spin asymmetry maps from the stripe to the flat regions) most probably is due to an inversion of the vacuum spin polarization above the stripes with respect to the flat regions, as it has already been reported in the literature for other ferromagnetic systems [136].

4.4.3.2 Type II

The magnetic measurements of type II islands were mainly performed at $V = 325\,\mathrm{mV}$ with a hysteresis loop shown in Fig. 4.28 **c** which reveals qualitatively the same magnetic behavior as for type I, but with a lower coercivity: between $B_z = -0.5\,\mathrm{T}$ and $B_z = 0.5\,\mathrm{T}$ the usual behavior of the tip (1) can be seen which orientates itself along the applied magnetic field. The island (in contrast to type I) already switches between $B_z = \pm 0.5\,\mathrm{T}$ and $B_z = \pm 1\,\mathrm{T}$. Thus it can be assumed that type II is also most likely a ferromagnetic monodomain out-of-plane Fe island, which exhibits a coercivity of $0.75\,\mathrm{T} \pm 0.25\,\mathrm{T}$. In addition, particular regions also appear to have an inverted spin polarization on this island relatively to the interior of the island (see Fig. 4.28 **e** and **f** for the hysteresis loop), which can also clearly be seen on the spin asymmetry map (shown in Fig. 4.28 **d**). Likely, an inversion of the vacuum spin polarization is the cause here as well. If we exclude these regions from the hysteresis curve (Fig. 4.28 **b**), we obtain an almost perfectly symmetric hysteresis loop with respect to the $B_z = 0\,\mathrm{T}$ axis (Fig. 4.28 **c**). Comparing the spin asymmetry map in Fig. 4.28 **d** with that of type I (see Fig. 4.27 **a**) then it is noticeable, that type I has a stronger spin polarization. It should also be noted that a comparison of the intensity of the spin asymmetry images can only be made from measurements with the same tip, which is the case here.

4.4.3.3 Type III

Type III islands are the least abundant. It can already be deduced from the STS data that the magnetic characterization cannot be performed as conclusively as for types I and II, since the spin polarization over the entire range from $-1\,\mathrm{V}$ to $1\,\mathrm{V}$ is relatively low compared to the other types (see Figs. 4.22 **b** and **c**).
While the other island types show a distinct switching behavior in the hysteresis (Fig. 4.23 **b**, **e** and Fig. 4.28 **c**, **f**), the $\mathrm{d}I/\mathrm{d}V$ values for this type remain relatively constant for magnetic fields in the range $|B_z| > 0.5\,\mathrm{T}$, which can be seen in the plotted data in Fig. 4.29 **c** and **f** (note the scaling of the axes!). With good will, a change in $\mathrm{d}I/\mathrm{d}V$ values, if at all, is most likely to be observed in small field regions where the tip magnetization direction is reoriented.

The following scenarios for the magnetic behavior of the island can be considered: Due to the proximity effect, i.e. the induction of superconducting properties into the island, the magnetization of the island might be quenched [90]. However, as already shown, a very low spin polarization (see Figs. 4.22 **b** around -400 mV and 375 mV) was detected in the STS measurement. Furthermore, the measured hysteresis curves of the islands

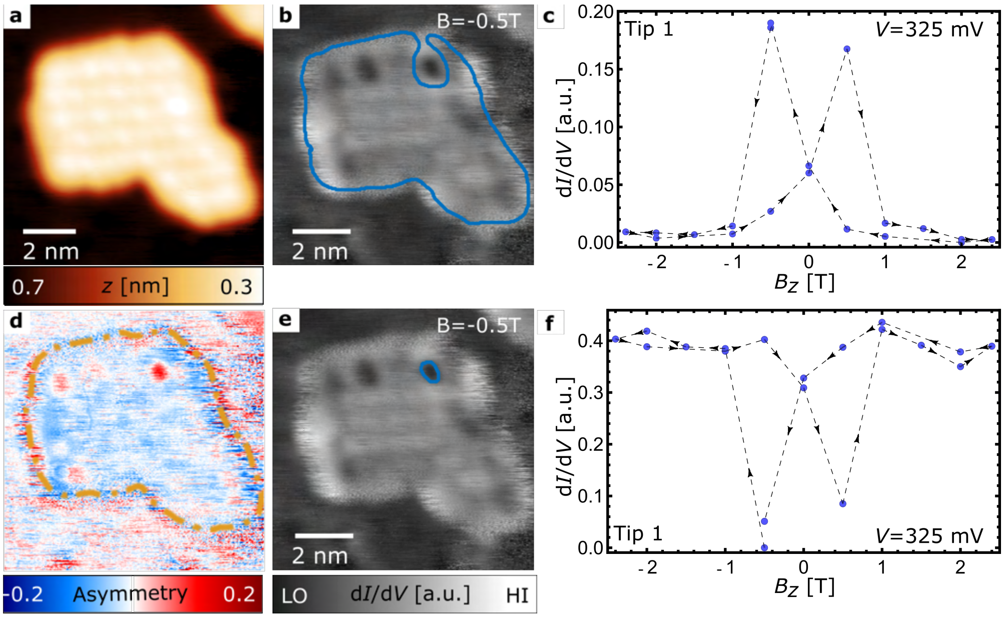

Figure 4.28: **a** STM image of a ML island of type II with its spin asymmetry map in **d** ($B_{z_1} = -2\,\mathrm{T}$, $B_{z_2} = +2\,\mathrm{T}$). In **b** and **e**, the first $\mathrm{d}I/\mathrm{d}V$ maps of the loop are shown as an example where the parts of the island which have been used to extract the data are indicated by blue areas. The extracted data from the area in **b** and **e** was averaged and plotted as a function of the B-field with the resulting hysteresis loops **c** and **f**, respectively. Measurement parameters are: $I = 1\,\mathrm{nA}$, $V_{\mathrm{mod}} = 10\,\mathrm{mV}$, $V = 325\,\mathrm{mV}$, $f = 1197\,\mathrm{Hz}$ and $T = 4.5\,\mathrm{K}$.

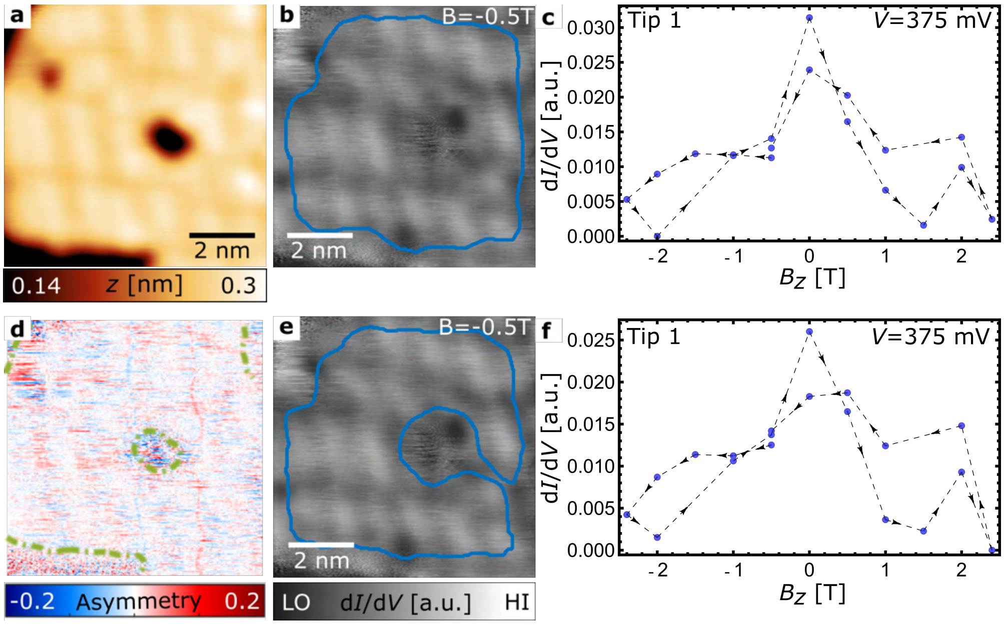

Figure 4.29: **a** Topography STM image of a ML island of type II with its spin asymmetry map in **d** ($B_{z_1} = -2\,\mathrm{T}$, $B_{z_2} = +2\,\mathrm{T}$). In **b** and **e**, the first $\mathrm{d}I/\mathrm{d}V$ maps of the loop are shown as an example, with the extracted data (blue outlined area) averaged and plotted as a function of the B-field with the resulting hysteresis loops **c** and **f**. In **e** and **f** the evaluation has been carried out without the disturbance (in the center right), which, however, does not show a strong effect. Measurement parameters are: $I = 1\,\mathrm{nA}$, $V_{\mathrm{mod}} = 10\,\mathrm{mV}$, $V = 375\,\mathrm{mV}$, $f = 1197\,\mathrm{Hz}$ and $T = 4.5\,\mathrm{K}$.

most probably show a minor spin contrast (see Fig. 4.29 **c**, **f**) at small magnetic fields. A further confirmation that this Fe reconstruction is magnetic is that it shows Shiba states in the gap of the superconductor, as will be shown in Sec. 4.5.3.

Another scenario is that the island could be strongly magnetized in-plane, which could not be detected by an out-of-plane sensitive tip (in this case at $|B_z| > 0.5\,\mathrm{T}$) and thus shows no spin contrast. However, Monte Carlo and Landau-Lifshitz-Gilbert simulations show (in the next Sec. 4.4.4) that, even with relatively high values of the exchange constant J and an in-plane anisotropy constant K_x (see Sec. 2.2.4.1 and Sec. 2.2.4.2) with an external applied magnetic field of $B_z = 3\,\mathrm{T}$, such an island would be magnetized in the direction parallel to the out-of-plane B-field by 25%. Such a magnetization would be measurable experimentally [138], in contradiction to the measurement results in this work.

Looking at the spin asymmetry map in Fig. 4.29 **d** compared to those of type I and II islands (see Fig. 4.27 **a** and Fig. 4.28 **d**)[5], we can see that the spin polarization is lowest in type III.

In Fig. 4.30 the hysteresis curves of the three Fe ML reconstructions are summarized in one plot, whereby the magnetization reversal behaviour of islands of type I and II at different coercive field strengths can be seen very well. To confirm the results of the experiment, additional measurements were made with different spin-polarized tips on other islands of different sizes and shapes. The resulting hysteresis curves can be seen in the appendix A.5, Fig. A.8, whereby Tab. 4.1 summarizes the coercive field strengths, that were found to be $B_c^{\mathrm{I}} = 2.3\,\mathrm{T} \pm 0.2\,\mathrm{T}$ for type I (strongest coercivity) followed by type II with $B_c^{\mathrm{II}} = 0.7\,\mathrm{T} \pm 0.3\,\mathrm{T}$ and type III with $B_c^{\mathrm{III}} < 0.4\,\mathrm{T}$. Note that for ML type III islands there is no spin-dependent contrast in the region $|B_z| > 0.5\,\mathrm{T}$, therefore only upper borders for the corresponding coercive fields of type III Fe ML islands can be given by the coercivity of the tip magnetization.

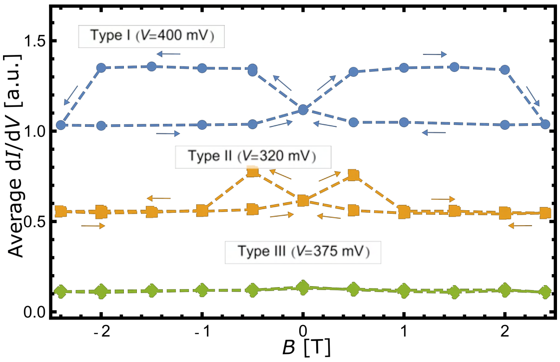

Figure 4.30: Hystereses of Fig. 4.23, Fig. 4.28 and Fig. 4.29 plotted all together for better comparison.

---

[5] These measurements were done with the same magnetic tip.

Table 4.1: Coercive fields B_c of the islands of different ML types with numbering and hysteresis loops according to Fig. A.8 in the Appendix (Island No. 9 is shown in Fig. 4.29), extracted from the hysteresis loops measured by different tips as given. The error in B_c is defined by the last (first) magnetic field value before (behind) the magnetization reversal of the island. For the type III islands, no clear contrast reversal is observed outside of the coercive field of the tip. Therefore, this magnetic field range can only be used to determine upper borders for B_c.

ML type	island no.	B_c [T]		
		tip 1	tip 2	tip 3
I	1			2.2 ± 0.2
I	2	2.2 ± 0.2		2.2 ± 0.2
I	3			2.2 ± 0.2
I	4		2.2 ± 0.2	
II	5	0.75 ± 0.25		0.6 ± 0.1
II	6			0.6 ± 0.1
II	7	0.45 ± 0.05		
III	8	< 0.4		< 0.4
III	9	< 0.4		

4.4.3.4 Magnetic Properties of Iron Double Layers

The second Fe layer, seen on a type I island in Fig. 4.31 **a**, shows essentially the same magnetic behaviour as the type I monolayers. In Fig. 4.31 **b** the hysteresis curve of a double layer is shown, whereby this was measured with tip 3 (for comparison with a hysteresis curve of a type I monolayer see appendix Fig. A.8). In summary, the double layer thus also exhibits, as in type I, a mono-domain ferromagnetic out-of-plane spin order with a coercive field of 2.2 T ± 0.2 T.

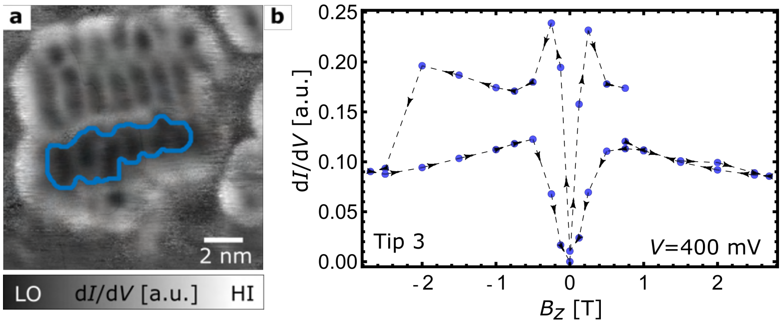

Figure 4.31: **a** First dI/dV map of the loop with the extracted data (blue outlined area) averaged and plotted as a function of the B-field with the resulting hysteresis loop **b**. A similar magnetic behavior is found as for type I ML islands. Note that compared to Fig.4.18 **b**, the magnetic loop here was recorded at up to ±2.7 T. For tip 3 it must be added that the loops were not measured correctly to the end. For a complete loop one can imagine the measuring points mirrored around $B = 0\,\mathrm{T}$. Measurement parameters: $I = 1\,\mathrm{nA}$, $V_{\mathrm{mod}} = 10\,\mathrm{mV}$, $V = 400\,\mathrm{mV}$, $f = 1197\,\mathrm{Hz}$ and $T = 4.5\,\mathrm{K}$.

4.4.4 Monte Carlo and Landau-Lifshitz-Gilbert Simulations

As anticipated in the previous Sec. 4.4.3.3, micromagnetic simulations were performed for the islands to rationalize the results. For this purpose, the MonteCrystal software for atomistic simulations of magnetic materials was used, implemented by Julian Hagemeister [139, 140]. The model implemented in this software considers the spins classically (i.e. as described in Sec. 2.2.4.1) and essentially uses a Heisenberg Hamiltonian that includes all energy terms discussed in Sec. 2.2.4.

For the Fe islands in this particular experiment, the Hamiltonian can be written as follows, neglecting the DMI interaction, since the measurements gave no indication of non-collinear magnetic structures:

$$H = -\sum_{i,j} J_{i,j} \left(\mathbf{S}_i \cdot \mathbf{S}_j\right) + \sum_i K_z \left(S_i^z\right)^2 + \sum_i K_x \left(S_i^x\right)^2 - \mu_B \sum_i S_i^z \cdot B_z. \tag{4.2}$$

For the simulations, localized Heisenberg spins $\mathbf{S}_i$[6] were placed on a triangular lattice of 30×30 sites (as well as 15×15 and 60×60 for comparison, see below and appendix A.5 Fig. A.10 **b** and **c**) such that the overall island exhibits a square shape. The effective exchange interaction coefficients $J_{i,j}$ have been restricted to the nearest neighbors (J_1). The on-site anisotropy can be chosen in any direction in the simulation program. For the simulations in this work, only uniaxial anisotropy directions were chosen, oriented either out-of-plane (K_z) or along K_x. In the Zeeman term (see also Sec. 2.2.4.4), the orbital angular momentum has been neglected (see Sec. 2.2.2) and the external magnetic field was chosen to be in out-of-plane orientation (B_z). The temperature was set to that of the experiment, i.e. $T = 4.5\,\mathrm{K}$ and the magnetic moment was chosen to a reasonable size consistent with the island material (Fe) of $m_z = 2.5\mu_\mathrm{B}$ [70].

To simulate the hysteresis curves found experimentally, the calculations of the spin configurations were started at a magnetic field of $B_z = -3\,\mathrm{T}$ and increased in steps of $0.125\,\mathrm{T}$ to $B_z = 3\,\mathrm{T}$ before being subsequently reduced back to $-3\,\mathrm{T}$ with the same step size. For each magnetic field strength, the simulation program then performs a freely selectable number of simulation steps, which vividly represents the time that the system is exposed to the magnetic field. The dependency of the result on the simulation steps is exemplarily shown in appendix A.5 Fig. A.10 **a**. It was found that with more than 60k simulation steps, the system had sufficient time to adjust to the external magnetic field. Therefore, 80k-100k steps were used for the simulations.

The constants J_1 (per bond), K_x and K_z were chosen within reasonable limits [139], so that the experimentally measured magnetization curves with its coercive fields are reproduced.

The resulting z component of the magnetization M, averaged over the whole lattice and all simulation steps (for the respective magnetic field strength), are shown as a function of B_z for different parameter settings in Fig. 4.32 **a** - **c**, with a summary of the resulting coercive field strengths and the parameter choices in Tab. 4.2.

Considering now the influence of J_1 and K_z ($K_x = 0$), the following conclusions can be drawn: First, the trend can be observed that the coercivity increases with J_1 and K_z, which can be seen in all three figures 4.32 **a** - **c**. However, K_z seems to influence the coercive field more than J_1. This result can be clearly seen by comparing Fig. 4.32 **a** and **c**.

Accordingly, the measured hysteresis curves can be reproduced by a variety of different parameter sets. In the following, therefore, plausible example values are presented with which the critical coercive fields can be obtained.

For type I Fe islands, a critical coercive field around $|B_c^\mathrm{I}| \approx 2.5\,\mathrm{T}$ can be reached for a large J_1 of $J_1 = 5\,\mathrm{meV}$ with small $K_z = -0.2\,\mathrm{meV}$ or for a small $J_1 = 1\,\mathrm{meV}$ with large $K_z = -0.5\,\mathrm{meV}$. Type II, on the other hand, can be simulated with a critical coercive field of $|B_c^\mathrm{II}| \approx 1\,\mathrm{T}$ with parameter sets, for example, of $J_1 = 2\,\mathrm{meV}$, $K_z = -0.1\,\mathrm{meV}$ and $J_1 = 1\,\mathrm{meV}$, $K_z = -0.2\,\mathrm{meV}$. For simulations with $J_1 = 1\,\mathrm{meV}$ and $K_z = -0.05\,\mathrm{meV}$,

---

[6] $\mathbf{S}$ describes the total spin of the atom.

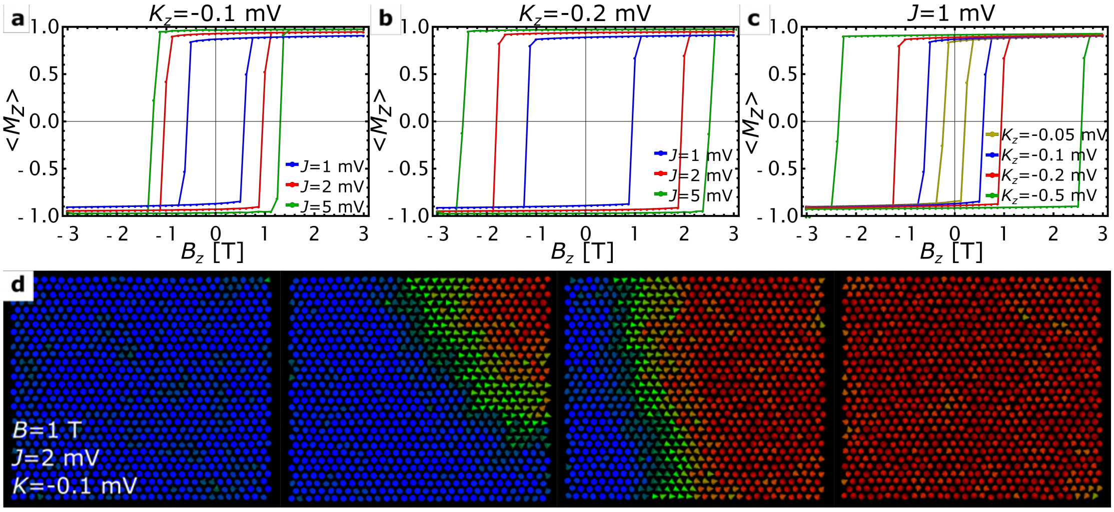

Figure 4.32: Monte Carlo simulation of the spin configuration of a square of a triangular spin lattice during an out-of-plane magnetic field loop (30 × 30 sites, $\mu = 2.5\mu_\mathrm{B}$, $T = 4.5\,\mathrm{K}$). Shown in **a**-**c** are the z component of the magnetization averaged over the whole lattice, $\langle M_z \rangle$, as a function of B_z for different selections of parameters, given inside and on top of each of the plots. In **d** there are four snapshots of the calculated spin configurations at a coercive field of $B_z = 1\,\mathrm{T}$ (for a set of parameters shown in the first panel), illustrating the switching by a nucleation at the edge of the island (second panel) and its propagation (third and fourth panels), with the colored cones indicating the orientations of the individual spins in the lattice.

the coercive field of the island becomes comparable to the coercive field of the tip $B_c^{\mathrm{tip}} \approx 0.1\,\mathrm{T}$ (see Sec. 4.4.1). In this case, SP-STS would be no longer sensitive to the coercive field and would yield a largely constant signal, consistent with the experimental observation for type III islands.

Furthermore, the simulations show, that the switching of the island is most often initiated by a nucleation at the edge or corner of the island, which is very plausible due to the smaller number of neighbors that can force the magnetization back to the initial position. In Fig. 4.32 **d** four simulation steps are shown as an example, before, during and after the switching process. It is clearly visible how a domain wall is formed, which propagates over the surface during the simulation steps and causes a complete flip of the magnetic moments of the island along the external field. As described before, it depends not only on the physical parameters but also on the number of simulation steps (which effectively describes time and thus, of course, also a physical parameter), or how abruptly the island switches, i.e. whether it switches over all Monte Carlo steps at one of the field steps or whether the process of aligning all spins continues over several B-field steps (see appendix A.5 Fig. A.10 **a**). Generally, as no indications of multidomain states were observed in the $\mathrm{d}I/\mathrm{d}V$ maps recorded during the hysteresis loop, we can assume that the switching of the magnetization of the islands by domain wall nucleation and propagation happens on a time scale which is much shorter compared to the time scale it takes to record the individual lines of the $\mathrm{d}I/\mathrm{d}V$ maps, which is seconds. To investigate the dependence of magnetization on the size of the island, further simulations were performed for several parameter sets and island sizes. In Fig. 4.33 **a**, exemplary hysteresis curves are shown for $J_1 = 2\,\mathrm{meV}$ and $K_z = -0.1\,\mathrm{meV}$ with island sizes of 15 × 15, 30 × 30 and 60 × 60 sites (more examples with other parameter sets are shown in Appendix A.5 Fig. A.10 **b**). It can be seen that there is hardly any difference in the coercive field strengths for the islands of different sizes. This in turn means that in this

Table 4.2: Summary of the simulations with the different parameters and the resulting coercive field B_c with a constant value for $K_x = 0\,\mathrm{meV}$, lattice sites of 30×30, $m_z = 2.5\mu_\mathrm{B}$ and $T = 4.5\,\mathrm{K}$.

J_1 [meV]	K_z [meV]	$\pm B_\mathrm{c}$ [T]	Fe ML Type
1	-0.1	0.62,-062	-
2	-0.1	1,-1	II
5	-0.1	1.24,-1.24	-
1	-0.2	1,-1.1	II
2	-0.2	1.9,-1.7	-
5	-0.2	2.5,-2.5	I
1	-0.1	0.63,-0.61	-
1	-0.5	2.6,-2.4	I
1	-0.05	0.26,-0.23	III

size range, the coercive field is essentially independent of the size of the island, as it was actually observed in the experiment.

Finally, simulations were also performed to assess the magnetization of the Type III Fe island, as mentioned earlier in Sec. 4.4.3.3. For this purpose, an anisotropy axis in the x-direction was assumed and different parameter sets were used. As can be seen from Fig. 4.33 **b**, even for a strong in-plane magnetic anisotropy (e.g. $J_1 = 5\,\mathrm{meV}$, $K_x = 1\,\mathrm{meV}$), there is still an out-of-plane magnetization of 25% of the saturation magnetization at the experimentally available maximum magnetic field of $B_z = \pm 3\,\mathrm{T}$, which would be experimentally detectable [138]. As this is in conflict with the measurements, it can be concluded, that the type III Fe islands most probably have a small out-of-plane magnetic anisotropy comparable to that of the tip, as summarized in table 4.2.

In summary, the simulations provide a deeper understanding of the measurement results. It is found that the size and shape of the island has practically no (or negligible) influence on the coercivity. Instead, the coercivity depends on the particular type of reconstruction, which most likely have different magnetic anisotropies and/or exchange constants. All reconstruction types indicate a single-domain out-of-plane ferromagnetic state, with the coercivity of type I being the strongest, followed by type II. The coercivity of type III most likely is of the same order of magnitude as that of the tip, which

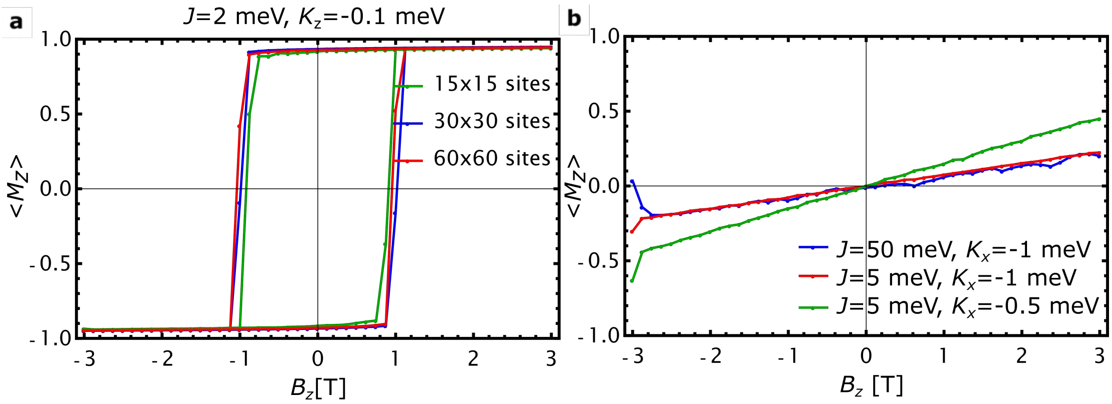

Figure 4.33: In **a** simulations with possible parameters for Fe ML type II islands with different island sizes are shown. It can be seen that the island size does not have much influence on the coercivity in these dimensions. In **b** simulations show that even with a larger in-plane anisotropy, there would still be a M_z component of 25% of the saturation magnetization $< M_z >= 1$ at $B_z = \pm 3\,\mathrm{T}$ that would have to be experimentally measurable, which was not the case.

is why these islands are practically invisible in the magnetic measurements.

4.5 Investigation of the Shiba Bands

In the previous chapter we found that most probably all three Fe reconstructions have an out-of-plane ferromagnetic spin structure with different coercive field strengths. Now, we will focus on the Shiba bands which should form by hybridization of the Yu-Shiba-Rusinov states of the individual Fe atoms of the islands [28, 29, 97, 141] (see also Sec. 2.4.3.2). For this purpose, spectroscopic line profiles were measured over the different reconstructed Fe-ML islands with a superconducting Nb tip (see Sec. 3.2.1). We should keep in mind that when using a Nb tip, the energies of all observed features are shifted by $\pm\Delta_t$ relative to the Fermi energy E_F (see Sec. 2.1.5), which means that $\pm\Delta_t$ is approximately the energy at which we should look for Majorana modes. Furthermore, we are interested in Shiba bands induced by the Fe islands in the gap of the substrate and thus focus on the energy range from $\pm\Delta_t$ to $\pm(\Delta_s + \Delta_t)$. In addition to point spectroscopy, dI/dV maps were taken at $\pm\Delta_t$ to investigate the Shiba states spatially. All measurements for the examination of the Shiba bands were naturally taken without the application of an external B-field. We will first discuss the islands individually, while a comparison between them will be made in the end. In addition, the measurement results of the DL Fe islands are also presented and discussed.

4.5.1 Type I Fe Islands and the Shiba Bands

Fig. 4.34 shows the measurement results of a line of point spectroscopies on a type I reconstruction. Looking at the plot in Fig. 4.34 **b**, where the measurement was performed on the niobium, typical features of a tunneling process between two superconductors can be seen (see Sec. 2.1.5), although the influence of the Fe island on the superconductor is increasing the closer one gets to the Fe island, since the DOS is non-zero in the range from $\pm\Delta_t$ to $\pm(\Delta_s + \Delta_t)$.

On the island itself, however (we will always consider the range $\pm\Delta_t$ to $\pm(\Delta_s + \Delta_t)$ in the following, if not specified otherwise), there is an increase of the spectral intensity in the whole gap region compared to the Nb substrate, whereby the coherence peaks are strongly suppressed. The spectral intensity can be assigned to the Shiba bands, which also have significant intensities at E_F. This is of great importance as it is an indication that their bandwidths are large enough to overlap with E_F, which is a necessary condition for the reopening of a p-wave gap (see Sec. 2.4.3.2 and [13]) and thus having different topological phases.

However, the intensity of the Shiba bands seems to fluctuate strongly depending on the location. In order to evaluate this disorder more accurately, i.e. to evaluate the intensities of the Shiba states and find possible local dependencies, autocorrelation calculations of the spectroscopic line profiles were done (see Sec. A.4.4 for a more detailed explanation).

Fig. 4.35 **b** shows the autocorrelation function for the point spectroscopy measurements highlighted in blue in Fig. 4.34 **a**. A modulation of about $x = 1.1\,\mathrm{nm}$ in the energy range just below the coherence peak ($V = \pm\ 2\,\mathrm{mV}$) can be found. In order to estimate this quantity, we consider the atomic lattice between the stripes, as measured and shown in Sec. 4.3, in an idealized form. We recall that the lattice is oriented in such a way that the long side of the unit cell is parallel to the long side of the stripes. The line of spectroscopy points then has an angle of $\approx 16^\circ$ to the short side of the unit cell. If we now consider a line with this angle relative to the short side of the unit cell, as illustrated in Fig. 4.35 **a**, we see that this line cuts the lattice atoms relatively precisely and that the

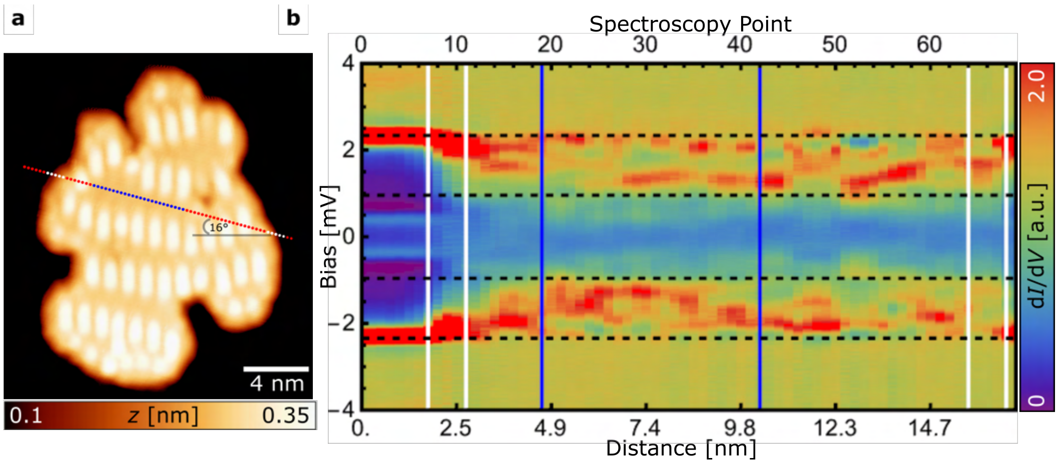

Figure 4.34: **a** STM image of a Fe ML island of type I, with dots marking the position where point spectroscopies were taken, running along a line from top left to bottom right. It, therefore, starts at the Nb substrate, crosses the island and ends again on Nb. The Fe island was oriented in such a way that the long sides of the central stripes are oriented vertically. According to the measurement results in Sec. 4.3, the lattice in the flat region between the stripes should then be oriented in such a way that the short side of the unit cell is horizontal (see Fig. 4.35 **a**). The line of spectroscopy points then has an angle of ≈ 16° to the short side of the unit cell, as is shown in **a**. The blue dots of the line of spectroscopy points are those used to calculate the autocorrelation shown in 4.35 **b**. (The autocorrelation was limited to the blue measuring points in order not to include the stripes in the evaluation.) White dots mark the transition from the island to the substrate or vice versa. In **b** the plot of the line spectroscopies in **a** is shown with the colour markings already explained for **a**. Gray dashed horizontal lines in the spectra are at $e \cdot V = \pm \Delta_\mathrm{t}$ ($\pm$ 0.96 mV) and $e \cdot V = \pm(\Delta_\mathrm{t} + \Delta_\mathrm{s})$ ($\pm$ 2.34 mV). Measurement parameters for **a**: $I = 400\,\mathrm{pA}$, $V = -4\,\mathrm{mV}$, $T = 4.5\,\mathrm{K}$; **b**: $I_\mathrm{stab} = 400\,\mathrm{pA}$, $V = -4\,\mathrm{mV}$, $V_\mathrm{mod} = 0.1\,\mathrm{mV}$, $f = 1197\,\mathrm{Hz}$ and $T = 4.5\,\mathrm{K}$.

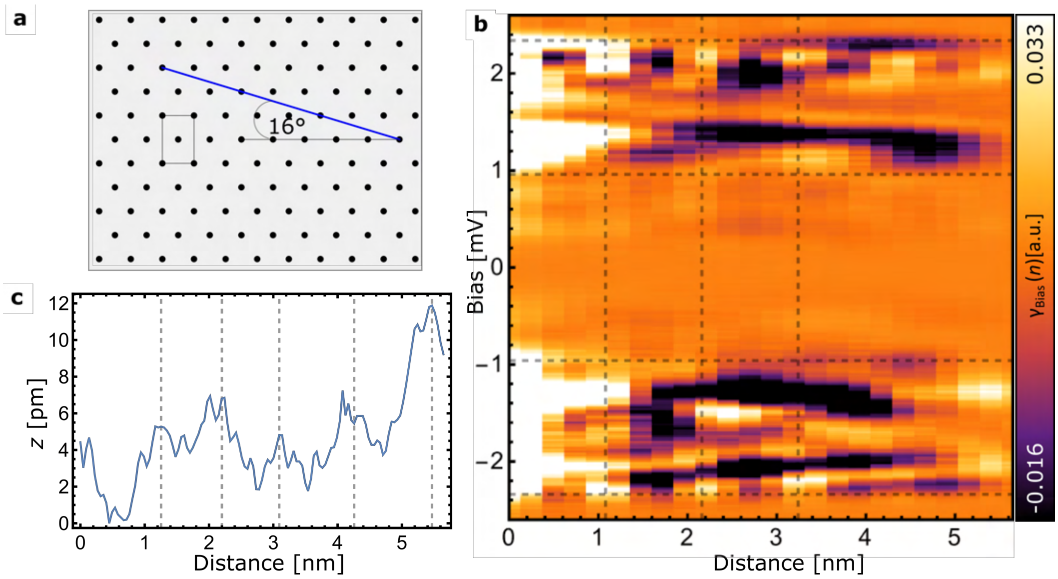

Figure 4.35: Shown in **a** is an idealized lattice, as it would be expected (according to the measurements described in Sec. 4.3) in the flat region between the stripes in Fig. 4.34 **a**. For the long and short sides of the unit cell, the mean values from Sec. 4.3 were used: $x = 0.46\,\mathrm{nm}$ and $y = 0.71\,\mathrm{nm}$. A line with an angle of ≈ 16° to the horizontal axis is shown in blue, analogous to Fig. 4.34 **a**. Shown in **c** is the height profile line taken from the STM image in **a** exactly where the blue dots in Fig. 4.34 **a** are. From this one can see an underlying topographic structure with a periodicity of about $1.09\,\mathrm{nm} \pm 0.16\,\mathrm{nm}$, which is also found in the autocorrelation calculation shown in **b**.

distance of these atoms on the line is approximately $x = 1.22\,\mathrm{nm} \pm 0.12\,\mathrm{nm}$[7]. In Fig. 4.35 **c** the line profile of the line point spectroscopy from the STM image Fig. 4.34 **a** is shown, from which an average spacing of the peaks of $x = 1.09\,\mathrm{nm} \pm 0.16\,\mathrm{nm}$ can be obtained. The lattice spacings taken from the autocorrelation thus agree well with the theoretical and topographically determined values within the measurement errors. Thus, it can be concluded that the variations in the spectral weight of the Shiba bands scales with the periodicity of the underlying topographic reconstruction. This modulation can already be seen in the Shiba bands near the coherence peaks.

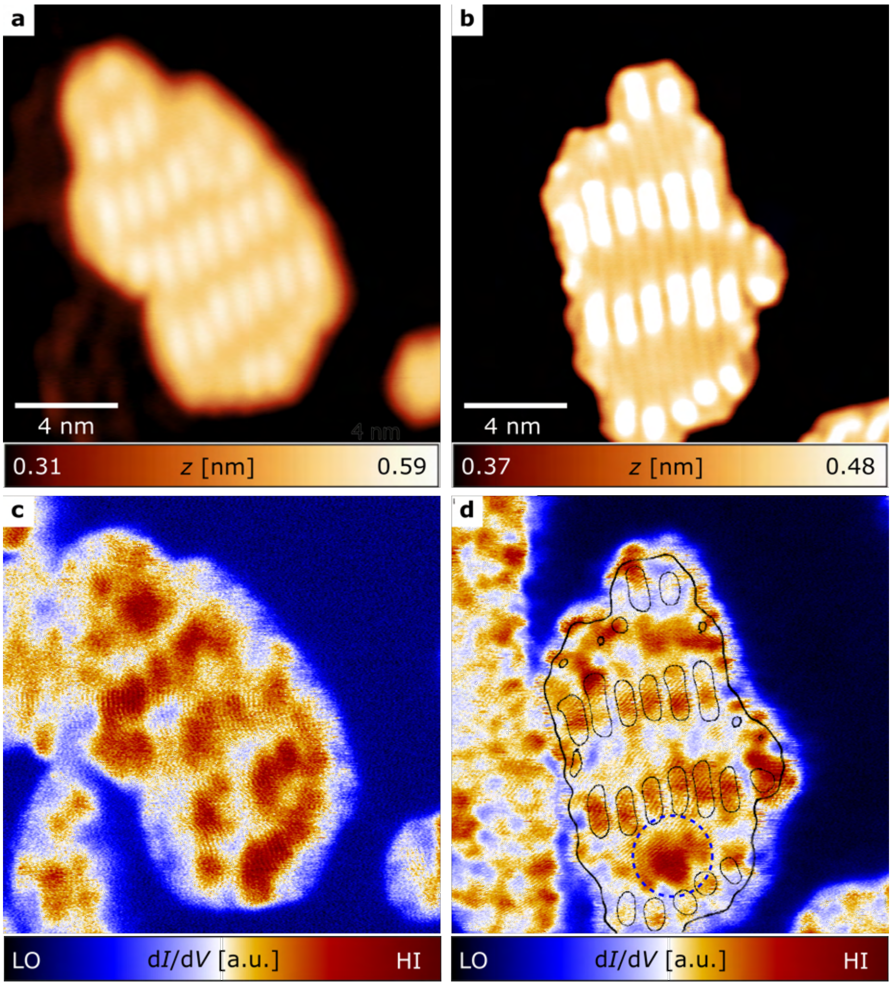

Figure 4.36: Shown in **a** and **b** are STM images of two different Fe type I ML islands with their respective $\mathrm{d}I/\mathrm{d}V$ maps shown in **c** and **d**, taken at Δ_t. In both **c** and **d**, a correlation of the Shiba states with the underlying structure can be seen. In **d**, the contour of the Fe island topography from **b** was also added to better visualize the correlation. Also seen in **d** but not in **c**, is the pronounced increased intensity of the Shiba band which appears over large flat areas (marked by a blue dashed circle in the lower part of the island). However, no edge states can be observed. Measurement parameters for **a** and **c**: $I_{\mathrm{stab}} = 200\,\mathrm{pA}$, $V_{\mathrm{mod}} = 0.1\,\mathrm{mV}$, $f = 1197\,\mathrm{Hz}$ and $T = 4.5\,\mathrm{K}$; **b** and **d**: $I_{\mathrm{stab}} = 400\,\mathrm{pA}$, $V_{\mathrm{mod}} = 0.1\,\mathrm{mV}$, $f = 1197\,\mathrm{Hz}$ and $T = 4.5\,\mathrm{K}$.

The correlation of the Shiba bands with the underlying topographic structure can

---

[7] The standard deviation was calculated using propagation of uncertainty, assuming that the measurement of the long and short axis of the unit cell are independent.

also be observed directly on the $\mathrm{d}I/\mathrm{d}V$ maps in Fig. 4.36 **c** and **d**, which in this case were taken at the energy of the tip gap. The $\mathrm{d}I/\mathrm{d}V$ maps in Fig. 4.36 **c** and **d** show that some of the most pronounced peaks correlate with the structure of the stripes, as can also be seen directly from Fig. 4.36 **d**, where the contour of the topographic image (Fig. 4.36 **b**) has been added as black lines on the $\mathrm{d}I/\mathrm{d}V$ map to illustrate the correlation.

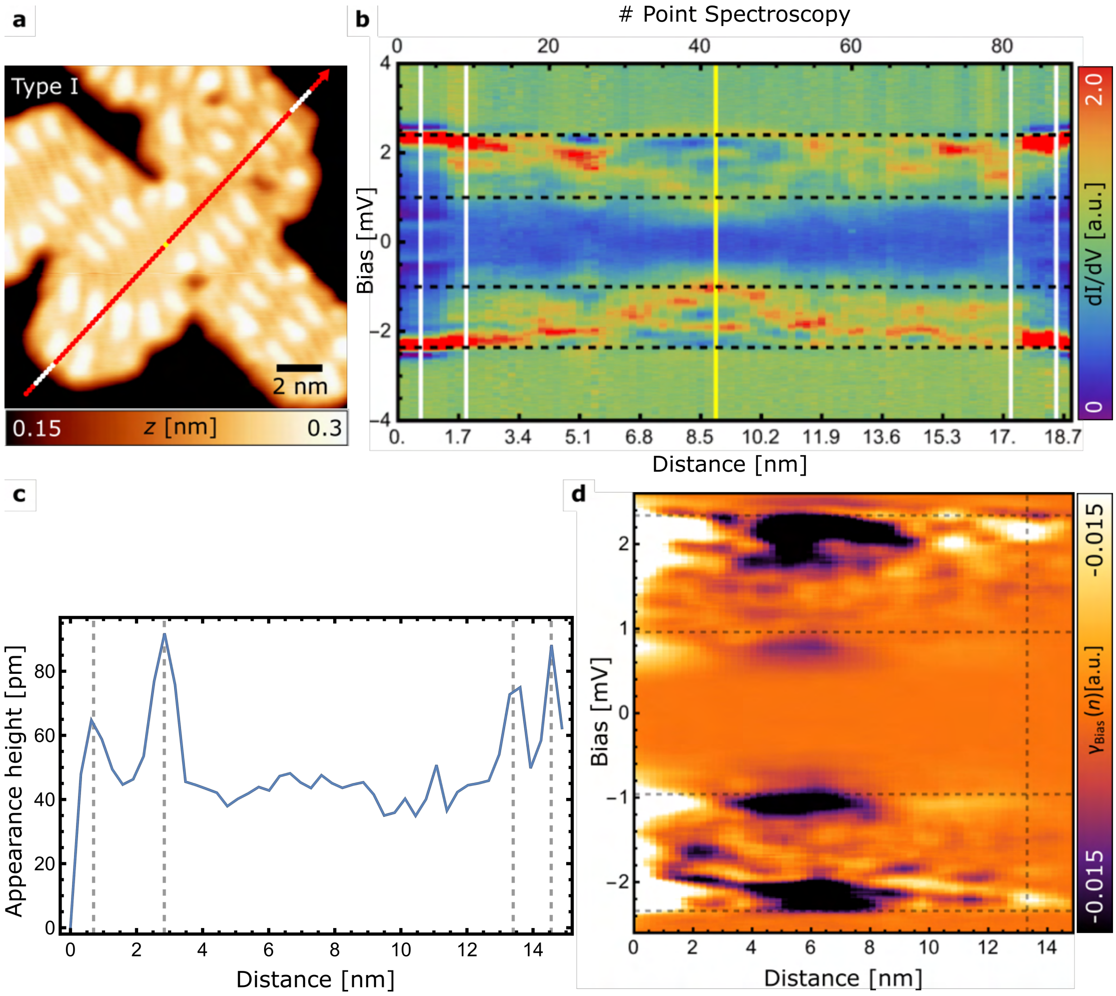

Figure 4.37: Shown in **a** is the topography image of an Fe ML type I with the markings of the point spectroscopies, running along a line from bottom left to top right. The point spectroscopies in the area of the transitions from Nb to Fe and vice versa are marked with white dots and on the island with red dots (except one white dot in the middle; $I = 1\,\mathrm{nA}$, $V = -6\,\mathrm{mV}$, $T = 4.5\,\mathrm{K}$). In **b** all point spectroscopies marked in **a** are plotted, where the transitions from Nb to Fe (and vice versa) are marked with vertical white lines. Gray dashed horizontal lines in the spectra are at $e \cdot V = \pm(\Delta_\mathrm{t} - \Delta_\mathrm{s})$, $e \cdot V = \pm\Delta_\mathrm{t}$ and $e \cdot V = \pm(\Delta_\mathrm{t} + \Delta_\mathrm{s})$ ($I_\mathrm{stab} = 400\,\mathrm{pA}$, $V_\mathrm{mod} = 0.1\,\mathrm{mV}$, $V_\mathrm{stab} = 4\,\mathrm{mV}$, $f = 1197\,\mathrm{Hz}$ and $T = 4.5\,\mathrm{K}$). **c** and **d** show the profile line of the topography image along the point spectroscopy line and the autocorrelation function, respectively, analogous to the Fig. 4.35 **b** and **c**.

Next, looking at a second line of point spectroscopies on another type I Fe island in Fig. 4.37 **a** and **b**, which includes several stripes, this correlation can also be found in the autocorrelation function. Indeed, the autocorrelation calculation in Fig. 4.37 **d** shows a strong minimum at about $\Delta x \approx 6.6\,\mathrm{nm}$ ($V = 2\,\mathrm{mV}$) and a local maximum at $\Delta x \approx 13.3\,\mathrm{nm}$ ($V = 2\,\mathrm{mV}$), indicated with a vertical dashed line. This distance of the

Shiba states scales approximately with the spacing of the stripes along the line spectra that were taken. The profile line can be seen in Fig. 4.37 **c** and shows a mean spacing of approximately 12.3 nm. Furthermore a minimum at $-1.6\,\mathrm{mV}$ can be seen which indicates an anticorrelation of 2.2 nm.
Another interesting effect in the study of the localization of the Shiba states is revealed by a direct comparison of the point spectroscopic measurements from Fig. 4.34 and Fig. 4.37. While in Fig. 4.34 on the flat areas between the stripes no increase Shiba band intensity at $\varDelta_\mathrm{t}$ can be observed, such an increase shows up very intensely in Fig. 4.37 (see Fig. 4.37 **b**, at the vertical yellow line in the plot, with the position on the island being marked with a yellow dot in Fig. 4.37 **a**). As it turned out from surveying several type I Fe islands, particularly wide flat areas must be present on the island for these locations of increased Shiba band intensity to occur. Specifically, the areas must have a minimum spacing of 3 nm between the stripes. This phenomenon can also be observed on the $\mathrm{d}I/\mathrm{d}V$ map in Fig. 4.36 **d** (marked with a blue circle on the lower part of the island) on a different island, which fulfills the condition of a wide flat area. However, since the intensities at $\varDelta_\mathrm{t}$ are strongly asymmetric, these are probably just trivial states, which are bound close to E_F and localized by the disorder potential in the Shiba bands. Also the magnetic measurements do not show any irregularities in the area of the intense peak. Furthermore, zero modes are predicted rather to appear at the edges of the island [87, 99]. So we can assume that the regions of increased Shiba band intensity appearing close to the flat areas are due to topologically trivial localized states in the Shiba band.

Looking at the $\mathrm{d}I/\mathrm{d}V$ maps at Δ_t, another significant result is apparent: no distinct edge states of the islands was found, signifying the absence of any Majorana edge modes (cf. Sec. 2.4.2.2). However, this result is not surprising, since ultimately no gap opening was found either, which is mandatory to obtain a non-trivial topological phase and essential for Majorana states.

4.5.2 Type II Fe Islands and the Shiba Bands

The investigations of the Shiba bands of type II islands show many properties that have already been discussed for type I: First of all, the gap is filled with Shiba bands over the entire island, which can be seen in Fig. 4.38 **b**. Then, in the Fermi energy region (horizontal dashed line at $\pm\varDelta_\mathrm{t}$, i.e. at $V = \pm 1\,\mathrm{mV}$), as for type I, states are present, but no gap opening is observed. If we now look at the coherence peaks $(\pm(\varDelta_\mathrm{t} + \varDelta_\mathrm{s}) = \pm 2.40\,\mathrm{mV})$, it appears that the intensity is less suppressed compared to type I (see also Fig. 4.44 **a** upper panel and Fig. 4.45 **c**). This phenomenon can be an indication that superconductivity is less suppressed for type II relative to type I, which could be because the total magnetization for type II could be lower than for type I (i.e., fewer Cooper pairs are broken up by the magnetic field of type II).

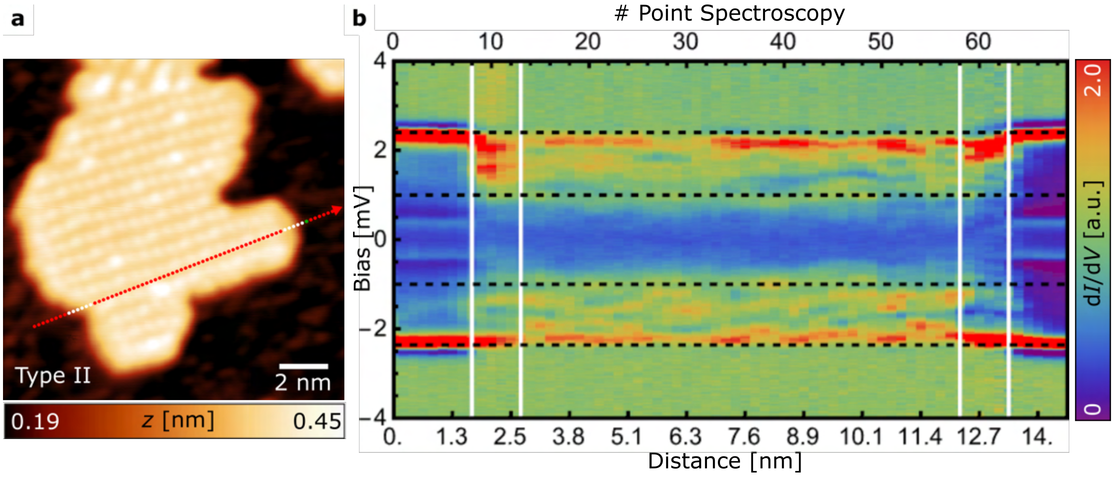

Figure 4.38: **a** STM image of a type II Fe ML, with dots marking the positions where point spectroscopies were taken, along the lines in the direction of the arrow. The point spectroscopies in the area of the transitions from Nb to Fe and vice versa are marked with white dots ($I = 1\,\mathrm{nA}$, $V = -6\,\mathrm{mV}$, $T = 4.5\,\mathrm{K}$). In **b** all point spectroscopies marked in **a** are plotted, where the transitions from Nb to Fe (and vice versa) are marked with vertical white lines. The dashed gray lines in the spectra are at $e \cdot V = \pm\varDelta_\mathrm{t}$ ($\pm 1\,\mathrm{mV}$) and $e \cdot V = \pm(\varDelta_\mathrm{t} + \varDelta_\mathrm{s})$ ($\pm\, 2.40\,\mathrm{mV}$). Measurement parameters: $I_\mathrm{stab} = 400\,\mathrm{pA}$, $V_\mathrm{mod} = 0.1\,\mathrm{mV}$, $f = 1197\,\mathrm{Hz}$, $V_\mathrm{stab} = 4\,\mathrm{mV}$ and $T = 4.5\,\mathrm{K}$.

In Fig. 4.39 **a**, simulation results are shown for the total magnetization as a function of J, for different values of K_z and without an external magnetic field. The total magnetizations for the values of J and K_z from Tab. 4.2, which provide possible parameter values for the islands based on the measured coercivity, are indicated by dots in Fig. 4.44 **a**. For example, the simulations show a total magnetization[8] of 95% for $K_z = -0.5\,\mathrm{meV}$ and $J = 1\,\mathrm{meV}$ (which are possible parameters for type I), 90% for $J = 1\,\mathrm{meV}$ and $K_z = -0.2\,\mathrm{meV}$ (which are possible parameter values for type II) and 77% for $J = 1\,\mathrm{meV}$ and $K_z = -0.05\,\mathrm{meV}$ (which are possible parameter values for type III), so it can be seen that the total magnetization for type II can be indeed lower than for type I. For illustration, in Fig. 4.39 **b-c** exemplary snapshots for the corresponding computed spin configurations are shown with colored cones indicating individual spins in the lattice. However, one should be aware that an increase in the exchange interaction with the conduction electrons of the superconductor usually leads to a shift of the Yu-Shiba-Rusinov states of individual atoms from the coherence peak to the gap region

---

[8] Relative to saturation magnetization respectively.

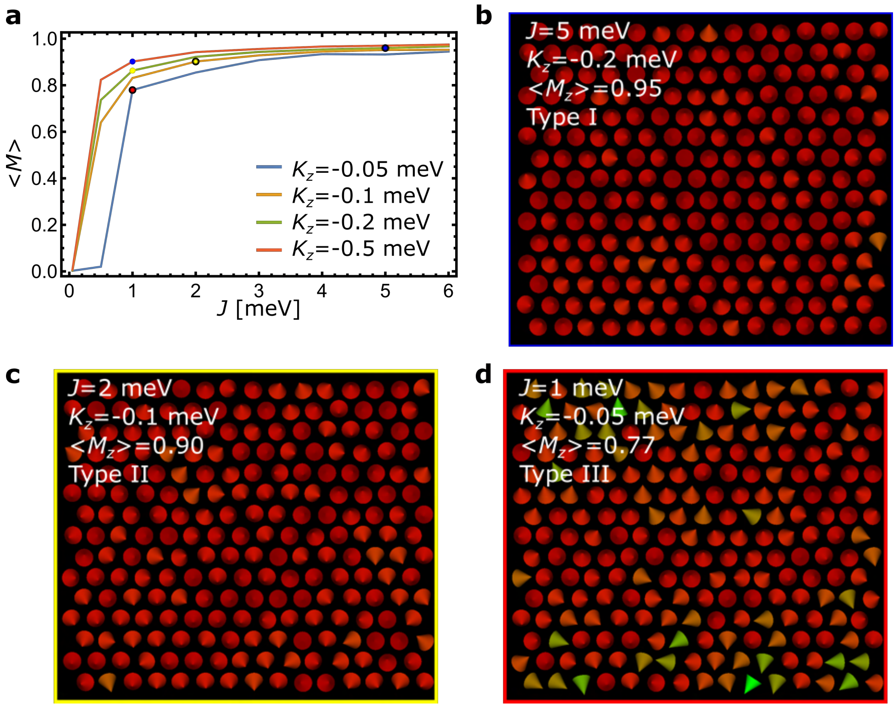

Figure 4.39: Simulations show the total magnetization averaged over the whole lattice (15 × 15 sites), $\langle M \rangle$, as a function of J for different K_z, given inside the plot. No external magnetic field is applied. The dots mark the possible parameter combinations of J and K_z of the different Fe types in Tab. 4.2: blue type I, yellow type II, and red type III with exemplary snapshots for their related calculated spin configuration (dots with black rims) indicating individual spins in the lattice in **b**-**c**.

[142, 143][9]. If this shift of the spectral weight continues towards the coherence peaks on the other side of E_F, then the Shiba states may overlap with the coherence peaks. This overlap may be also possible for weak exchange interactions (see Sec. 2.4.3.1).

Consider, for example, the point spectroscopies in Fig. 4.40, which were taken on pure Nb (blue curve, point spectroscopy no. 70) and on pure Nb, but relatively close to the Fe islands (green curve, point spectroscopy no. 64). The green point spectroscopy curve shows a broadening of the coherence peaks and a shoulder in the neighborhood of $V \approx 2\,\mathrm{mV}$, which is a strong indication that a superposition of the coherence peaks with the Shiba bands is present in this case. Also shown is a point spectroscopy in the middle of the island for comparison (red curve, point spectroscopy no. 35).

The autocorrelation calculations for type II, roughly reflects the periodicity of the reconstruction along the recorded spectroscopy line (see Fig. 4.40 **b**). The minimum value of the autocorrelation was found at $\gamma_\mathrm{min} = -0.0013$, which indicates that the variation of the spectral weight of the Shiba bands over the island is weaker in type II than in type I. However, a correlation of the Shiba bands with the underlying structure was still found, which is very convincing when looking at the two-dimensional $\mathrm{d}I/\mathrm{d}V$ maps, e.g. at Δ_t and within the gap at $V = 1.35\,\mathrm{mV}$, as it is exemplarily shown in Fig. 4.41. As for type I, no edge state is observed in the $\mathrm{d}I/\mathrm{d}V$ map at Δ_t for the type II Fe ML (see Fig. 4.41 **b**).

---

[9] This can also be made plausible by plotting Eq. (2.68) in Sec. 2.4.3.1.

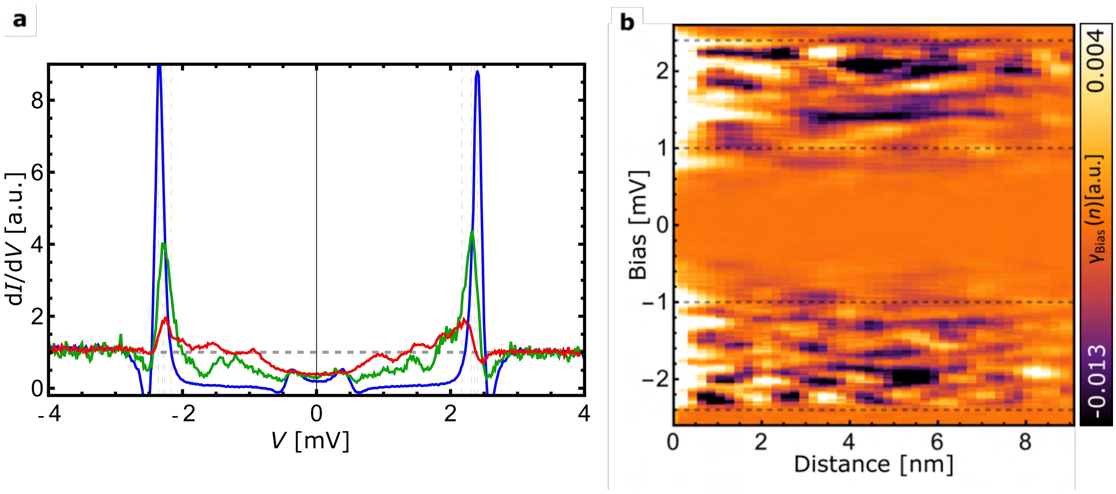

Figure 4.40: **a** Point spectroscopies on pure Nb (blue), measured relatively close to the Fe islands (green, see also green dot in Fig. 4.38 **a**) and on the Fe island (red) are shown. The green point spectroscopy curve shows a broadening of the coherence peaks and a shoulder in the neighborhood of $V \approx 2\,\mathrm{mV}$, which is most likely due to a superposition of the coherence peak with Shiba bands ($I_{\mathrm{stab}} = 400\,\mathrm{pA}$, $V_{\mathrm{mod}} = 0.1\,\mathrm{mV}$, $V_{\mathrm{stab}} = 4\,\mathrm{mV}$ and $T = 4.5\,\mathrm{K}$). **b** shows the autocorrelation function for the data on the island (red dots in Fig. 4.38 **a**).

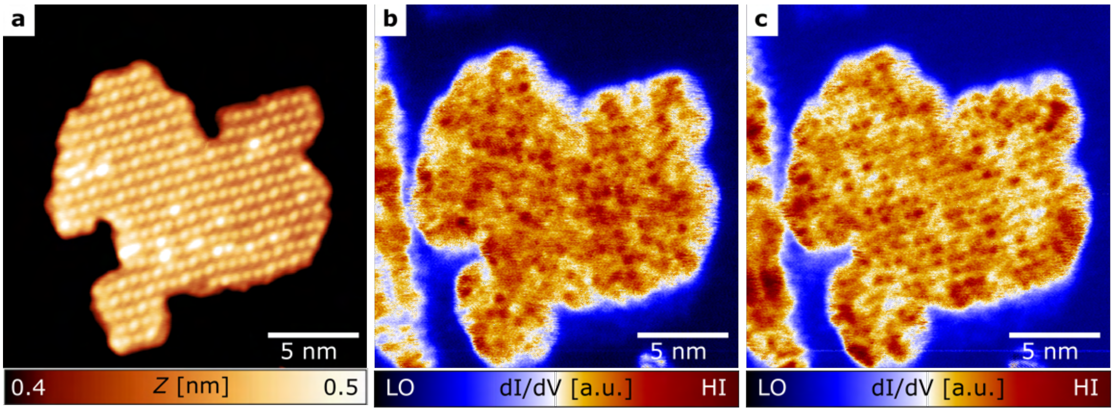

Figure 4.41: **a** STM image of a type II Fe ML island for $I = 400\,\mathrm{pA}$, $V = 4\,\mathrm{mV}$, $T = 4.5\,\mathrm{K}$. In **b** the two-dimensional $\mathrm{d}I/\mathrm{d}V$ map at the tip gap is shown ($I = 400\,\mathrm{pA}$, $V_{\mathrm{mod}} = 0.1\,\mathrm{mV}$, $V = 0.96\,\mathrm{mV}$, $T = 4.5\,\mathrm{K}$). It can be clearly seen that no distinct edge state appears. However, Shiba bands are found across the island with a spatial variation reflecting the underlying topographic structure of the island, which is also evident in **c** ($V = 1.35\,\mathrm{mV}$ $I = 400\,\mathrm{pA}$, $V_{\mathrm{mod}} = 0.1\,\mathrm{mV}$ and $T = 4.5\,\mathrm{K}$).

4.5.3 Type III Fe Islands and the Shiba Bands

The spectroscopic line profiles measured on a type III Fe island, which can be seen in Fig. 4.42 **b** (with the corresponding topography image in Fig. 4.42 **a**), show that Shiba bands fill the entire gap of the superconductor substrate, just as for types I and II. These are also localized close to the Fermi energy, but neither any gap opening nor any edge modes are evident.

However, there are two major differences compared to the other types that can be observed.

Firstly, the coherence peak is visible over the entire island and is not as strongly suppressed as in type I and II. The difference becomes obvious when the point spectroscopies for several measurement points are averaged and the averaged point spectroscopy curves for all three islands are plotted together, as shown in Fig. 4.44 **a**. This fact, that the coherence peaks of the type III Fe islands are relatively strong compared to the coherence peaks of the type I and type II Fe islands, can also be observed in the two-dimensional dI/dV maps taken at the energy of the coherence peak of Nb shown in Fig. 4.45 **c**. Assuming that, as already discussed in Sec. 4.5.2, there is a connection between the suppression of superconductivity and J and K_z (thus also to the coercive field of the islands), the observed trend seems plausible. The simulations for type III in fact give, with a possible combination of $J = 1\,\mathrm{meV}$ and $K_z = -0.05\,\mathrm{meV}$, a total magnetization of 77% (related to the saturation magnetization, see Fig. 4.39). Thus, compared to the other types, it is the lowest value of the total magnetization associated with the lowest suppression of the superconductor. However, it cannot be excluded that there are actually Shiba states on the type III Fe islands at the energy of the coherence peak, so that the actual coherence peak of the niobium appears stronger only due to the positive interference with the Shiba states.

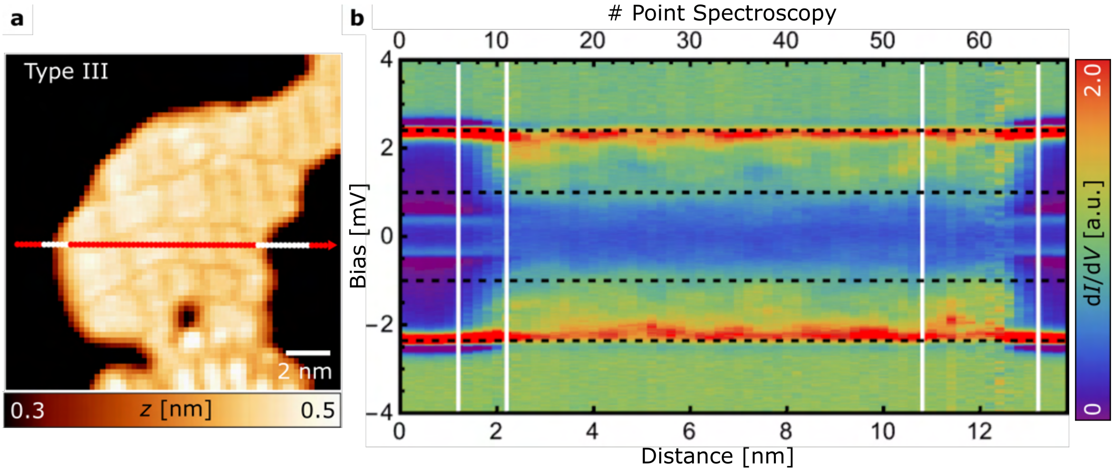

Figure 4.42: **a** STM image of an Fe ML island of type III, with dots marking the position where point spectroscopies were taken, along the lines in the direction of the arrow. The point spectroscopies in the area of the transitions from Nb to Fe and vice versa are marked with white dots ($I = 1\,\mathrm{nA}$, $V = -6\,\mathrm{mV}$, $T = 4.5\,\mathrm{K}$). In **b** all point spectroscopies marked in **a** are plotted, where the transitions from Nb to Fe (and vice versa) are marked by vertical white lines. Gray dashed horizontal lines in the spectra are at $e \cdot V = \pm\Delta_\mathrm{t}$ and $e \cdot V = \pm(\Delta_\mathrm{t} + \Delta_\mathrm{s})$ ($I_\mathrm{stab} = 400\,\mathrm{pA}$, $V_\mathrm{mod} = 0.1\,\mathrm{mV}$, $V_\mathrm{stab} = 4\,\mathrm{mV}$ and $T = 4.5\,\mathrm{K}$).

The second major difference which is noticeable when comparing Fig. 4.42 **b** with the other plots of type I and II (see Fig. 4.37 **b** and Fig. 4.38 **b**) is that the spectral weight for type III islands appears to be lower and more homogeneously distributed. This implies that the Shiba bands in this case are less strongly correlated with the underlying topography and that the potential disorder effect due to the structure is smaller in this case than for type I and II. The dI/dV map taken at Δ_t, which is shown in Fig. 4.43 **b**, support the previous hypothesis: a correlation with the topographic structure is difficult to detect (compared to Fig. 4.41 **b** and **c** and Fig. 4.36 **c** and **d**), if at all then most likely with the reconstruction lines of the island. Autocorrelation calculations also roughly reflect this assumption (see Fig. 4.43 **c**), where a periodicity which most likely correlates with the reconstruction lines can be found. The minimum autocorrelation value for type III is $\gamma_{\min}$ = -0.007, indicating that the variation in the spectral weight of the Shiba bands over the island is weakest for type III ML Fe islands.

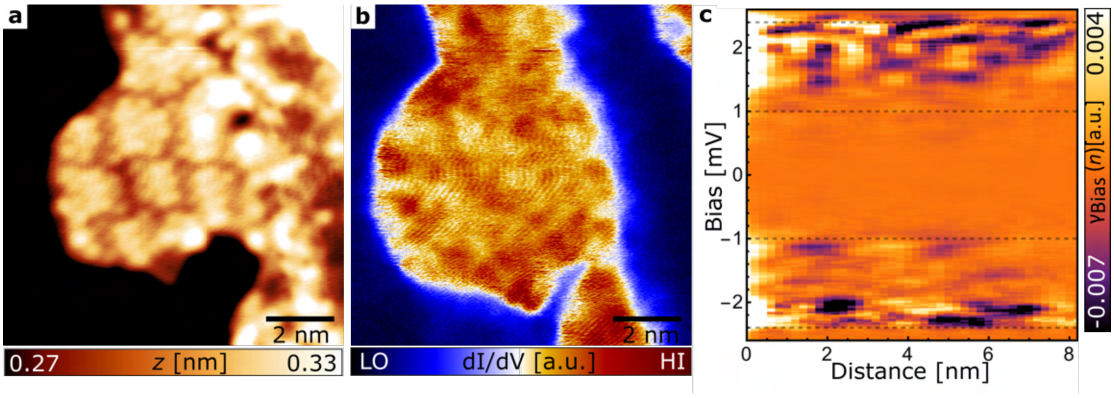

Figure 4.43: **a** STM image of a type III Fe ML island with I = 400 pA, V = 4 mV, T = 4.5 K. In **b** a dI/dV map at the tip gap is shown (I = 400 pA, V_{mod} = 0.1 mV, V = 0.96 mV and T = 4.5 K), on which it can be clearly seen that no distinct edge state appears. Shiba bands are found all over the island. However, at least in this image, a correlation of the lateral variation in Shiba band intensity to the underlying structure cannot clearly be identified. **c** shows the autocorrelation function for the data on the island (red dots in Fig. 4.42 **a**).

The fact, that the spectral weights within the band gap of the three islands are largest for type I, followed by II and III, can be confirmed by looking at the distribution of the dI/dV values of the point spectroscopies. These are shown as a histogram in Fig. 4.44 **b**. For this purpose, only point spectroscopies on the island were considered. Furthermore, the energy range was restricted to be in the range from ± 2 mV to Δ_t. The mean dI/dV value for type I is 1.138, for type II 1.097 and for type III 1.016. This confirms the assumptions made above.

For a comparison of the dI/dV maps (taken at the energy of the tip gap) for the three different island types, Fig. 4.45 **b** can be considered, on which all island types are represented (since the individual dI/dV maps of the different islands have been scaled individually and therefore cannot be used for a direct comparison). Again, it can be clearly seen that none of the islands have a pronounced edge state and that the intensity of the Shiba bands is lowest for type III. Furthermore, dI/dV maps of the coherence peak spectral weight in Fig. 4.45 **c** show that the islands display a negligible inverse proximity effect on the Nb(110) substrate, which can be seen by the immediate recovery of the coherence peak spectral intensity within less than a nm distance to all island edges (Fig. 4.45 **c**, **d**), unlike what was observed for other systems [144].

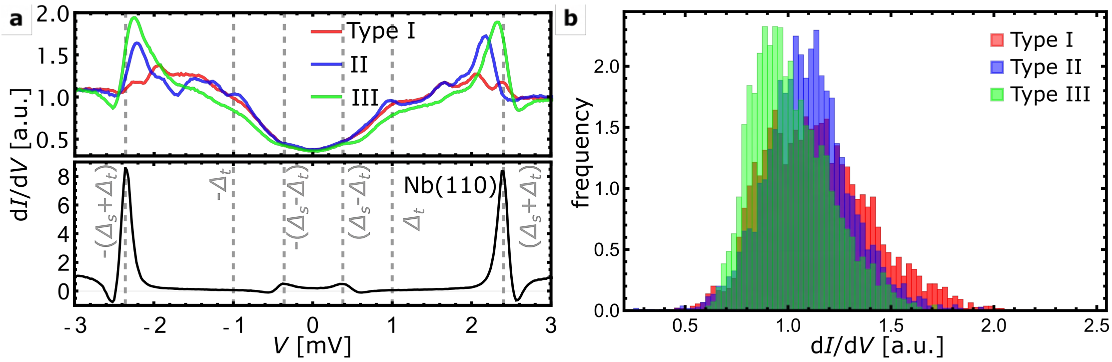

Figure 4.44: **a** Upper panel: Spectra averaged on top of the three islands from the spectroscopic line profiles in Fig. 4.37 **a**, Fig. 4.38 **a** and Fig. 4.42 **a**. Lower panel: Spectrum averaged on an area of the bare Nb(110) surface. Gray dashed vertical lines in the spectra are at $e \cdot V = \pm(\mathit{\Delta}_{\mathrm{t}} - \mathit{\Delta}_{\mathrm{s}})$, $e \cdot V = \pm\mathit{\Delta}_{\mathrm{t}}$ and $e \cdot V = \pm(\mathit{\Delta}_{\mathrm{t}} + \mathit{\Delta}_{\mathrm{s}})$. In **b** the histogram is shown, where only $\mathrm{d}I/\mathrm{d}V$ values within the gap were used, i.e. from $V = -2\,\mathrm{mV}$ to $V = 2\,\mathrm{mV}$, and only the point spectroscopies taken on the island (points close to the edge were also left out). To be specific, point spectroscopies 30-72 were used for type I, 20-62 for type II and 12-54 for type III.

The most important findings of the investigations of the Shiba bands will now be briefly summarized. The coherence peak is increasingly suppressed from type III over type II to type I, i.e. in the order of increasing coercivity. The energy-averaged intensity of the Shiba bands increases from type III to type I, whereas states can be found also near the Fermi energy for all island types, but no gap opening. Autocorrelation calculations and $\mathrm{d}I/\mathrm{d}V$ maps show an association of the lateral variation in the Shiba band intensity with the underlying topographic structure of the islands, where these variations are highest for type I, followed by type II and type III. This is also reflected by the minimum values of the autocorrelation calculation and strengthened by the histograms. Furthermore, no edge states in the entire energy range of the gap of the substrate (see $\mathrm{d}I/\mathrm{d}V$ maps) and thus no evidences for Majorana modes were found.

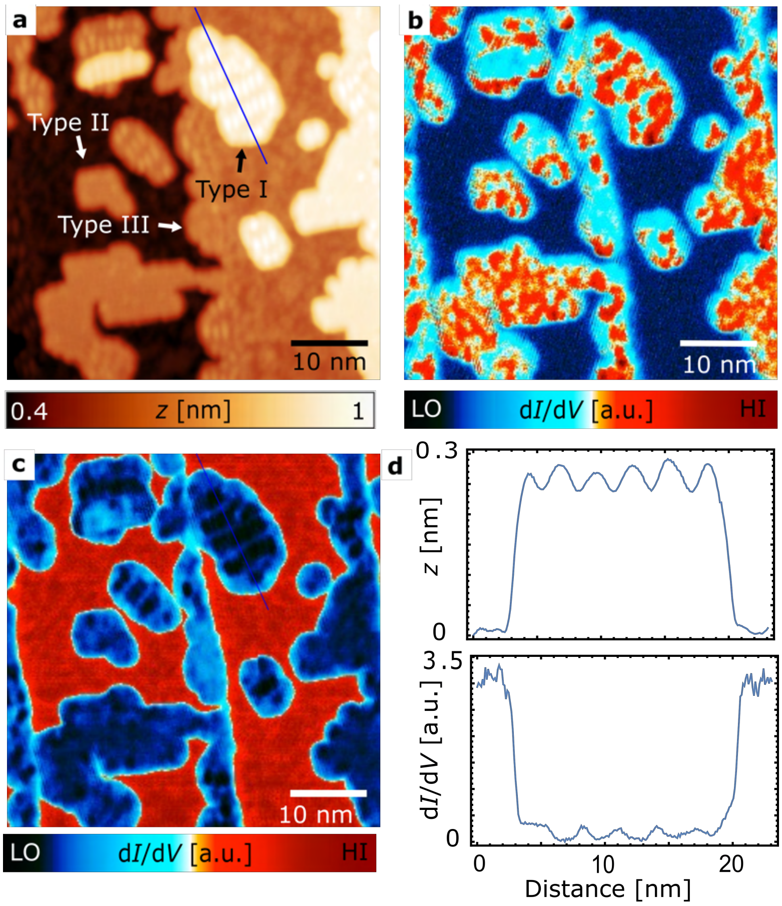

Figure 4.45: **a** Overview STM image of an area with several Fe ML islands of all three types. **b** Fermi energy and **c** Nb(110) coherence peak spectral weights, respectively, taken from spectroscopic grids over the same area recorded by following the tip height from **a** ($e \cdot V = 1\,\text{meV} = \varDelta_\text{t}$ for **b** and $e \cdot V = 2.5\,\text{meV} = \varDelta_\text{t} + \varDelta_\text{s}$ for **c**). **d** Line profiles of the height (top panel) and Nb(110) coherence peak spectral weight (bottom) taken along identical lines across the type I island shown in **a** and **c**, respectively. ($T = 4.5\,\text{K}$, $I = 200\,\text{pA}$, $V = 6\,\text{mV}$, $V_\text{mod} = 0.1\,\text{mV}$ (**a**); $V = 1.13\,\text{mV}$, $V_\text{mod} = 0.1\,\text{mV}$ (**b**); $V = 2.5\,\text{mV}$, $V_\text{mod} = 0.1\,\text{mV}$ (**c**)).

4.5.4 Iron Double Layer and the Shiba Bands

As described in the previous sections, no indications of topologically nontrivial states were found on the Fe monolayers. An indication that different topological phases are present in the system would be a reopening of the gap, which in turn is a prerequisite for Majorana modes, as described in Sec. 2.4.

Fe double layers (as they occasionally occur for this sample) on type I Fe islands can be seen in the overview image of Fig. 4.46 **a**. At the energy of the tip gap, the spectral weight is drastically reduced compared to the states of the underlying first layer. This can be clearly seen in the $\mathrm{d}I/\mathrm{d}V$ map in Fig. 4.46 **b**, where the DL regions are highlighted in red frames. The reduction of the spectral weight of the Shiba bands at Δ_t occurs nearly on the whole area of the double layer (see also Fig. 4.46 **c**, where two of the DL islands are shown enlarged as examples).

Looking now at point spectroscopy measurements on the DL in Fig. 4.47 **b**, the effect of the strongly reduced Shiba states at energies close to Δ_t is also evident. On the other hand, point spectroscopy also shows an increased spectral weight at energies close to the coherence peak compared to spectroscopy on an ML type I island (see Sec. 4.47 **b** red and black curve). Furthermore, it seems that the coherence peaks are more clearly visible and thus less suppressed.

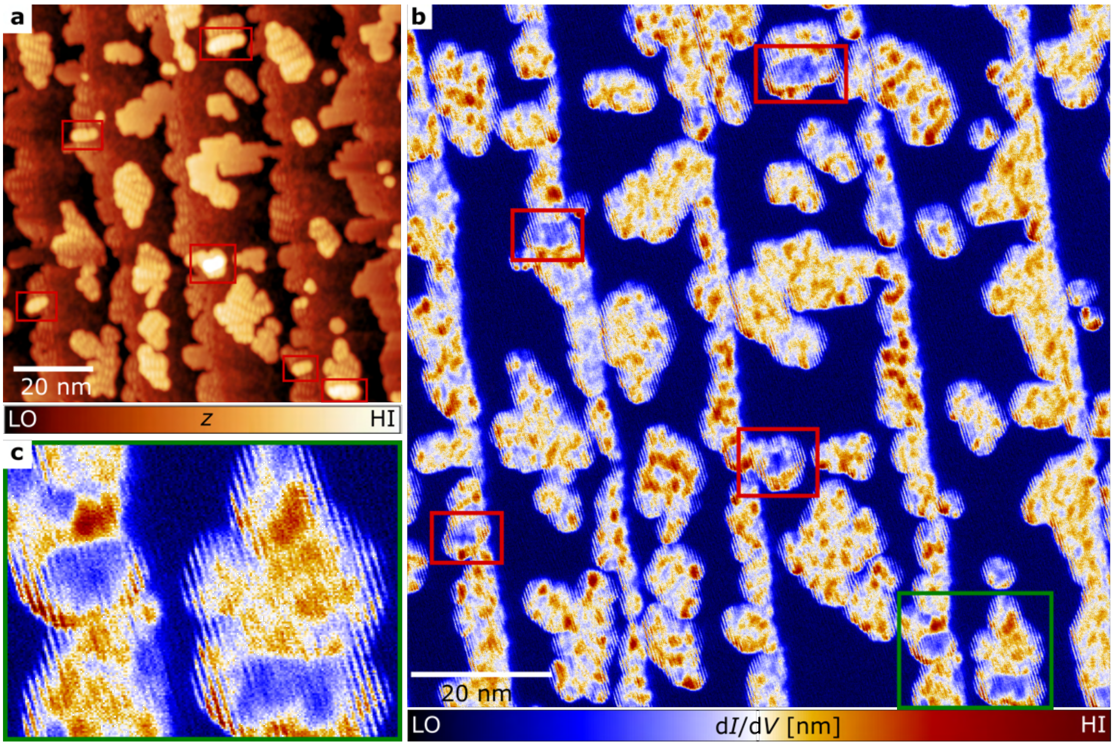

Figure 4.46: **a** STM image of a relatively large area of 200 × 200 nm^2 of the sample together with the simultaneously acquired $\mathrm{d}I/\mathrm{d}V$ map at Δ_t in **b**. Several Fe islands of different types can be seen in **a** and **b**. Of particular interest are the Fe double layers which are outlined in red and green. All DL islands are located on larger monolayer islands. All monolayers show Shiba states at Δ_t, which spread over large areas of the ML. It is striking that the DL, on the other hand, does not show intense spectral weights, but instead almost continuous states on the edges. In **c** an enlargement of an area is shown with two DL Fe islands. Measurement parameters: $T = 4.5\,\mathrm{K}$, $I = 200\,\mathrm{pA}$, $V = 1.13\,\mathrm{mV}$ and $V_\mathrm{mod} = 0.1\,\mathrm{mV}$.

The described effects may seem surprising at first glance, but two obvious explanations

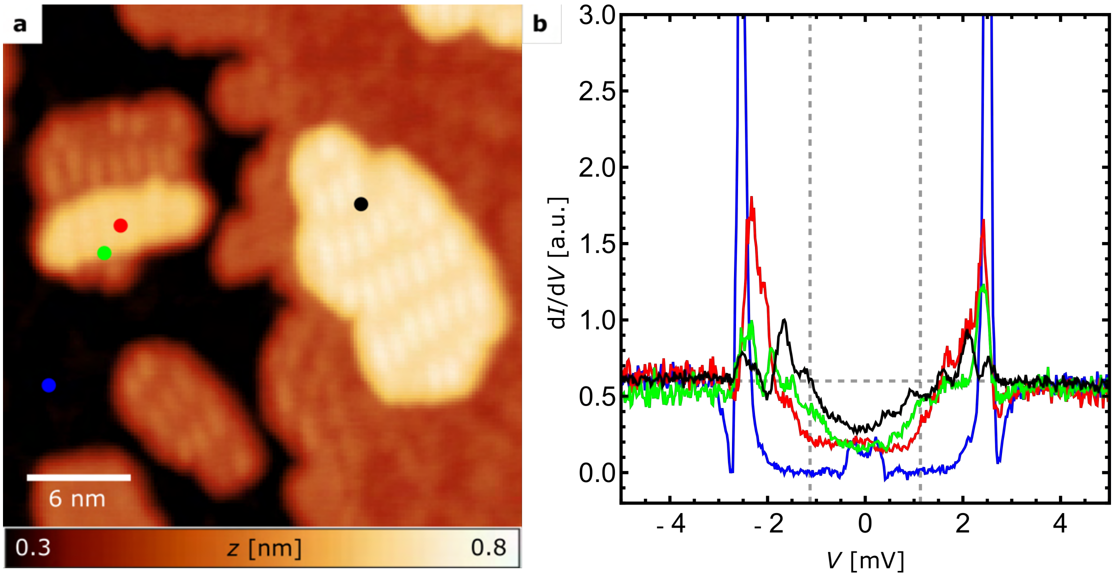

Figure 4.47: Shown in **b** are point spectroscopies measured on niobium (blue), the double layer of Fe (red), the edge of the Fe double layer (green) and on the Fe monolayer island (black) as indicated in **a**. The grey dashed vertical lines in **b** indicate the values $\pm\Delta_t$. The horizontal grey dashed line in **b**, on the other hand, shows the LDOS, as a reference line for evaluating the gap states. Measurement parameters for **a**: $I = 2\,\mathrm{nA}$, $V = 375\,\mathrm{mV}$, $T = 4.5\,\mathrm{K}$ and for **b**: $I_{\mathrm{stab}} = 200\,\mathrm{pA}$, $V_{\mathrm{mod}} = 0.1\,\mathrm{mV}$, $V_{\mathrm{stab}} = 6\,\mathrm{mV}$.

come to mind: As already discussed in Sec. 4.5.2, due to a strong exchange interaction of the substrate electrons with the electrons of the magnetic island, Shiba states or Shiba bands can be shifted towards the coherence peaks and overlap with them. The exchange constant could be different for this system because an additional magnetic layer has been added and thus a higher amount of magnetic neighbouring atoms is present. A larger exchange constant compared to a monolayer would therefore be a plausible explanation for states occurring increasingly at energies close to the coherence peak and further close to the Fermi energy.

In this context, however, it is also important to mention that the topological phase of the system can change when the exchange constant J (see Eq. (2.67)) changes. Thus, it cannot be excluded that the DL is topologically nontrivial and the reduced DOS on the DL is an indication of a reopening of the gap.

In the following, we take a closer look at the edges of the double layers at Δ_t. In Fig. 4.48 **c**, we find states almost on the entire edge. Of course, it is reasonable to assume that at least some of these states originate from the underlying type I monolayer. This becomes apparent when considering the profile lines shown in Fig. 4.48 **b** and **d** for the topographic measurement from Fig. 4.48 **a** and the Fermi level dI/dV map from Fig. 4.48 **c**. The transitions from the double layer to the monolayer are clearly visible in Fig. 4.48 **b** and marked with vertical gray dashed lines. From Fig. 4.48 **d** it is thus evident that possible edge states of the double layer are super-imposed by the states of the monolayer. A point spectroscopic investigation on the edge (see green curve in Fig. 4.47 **b**) reveals characteristics of a gap-like feature, but also asymmetric states in the gap. Compared to the red curve, one can see a higher density of states at E_{F} for the green curve. However, it should be noted that the location where the measurement was made does not completely match the edge state, as can be seen in Fig. 4.48 **c**.

If we consider a profile line where the second layer forms a sharp edge to the niobium, as

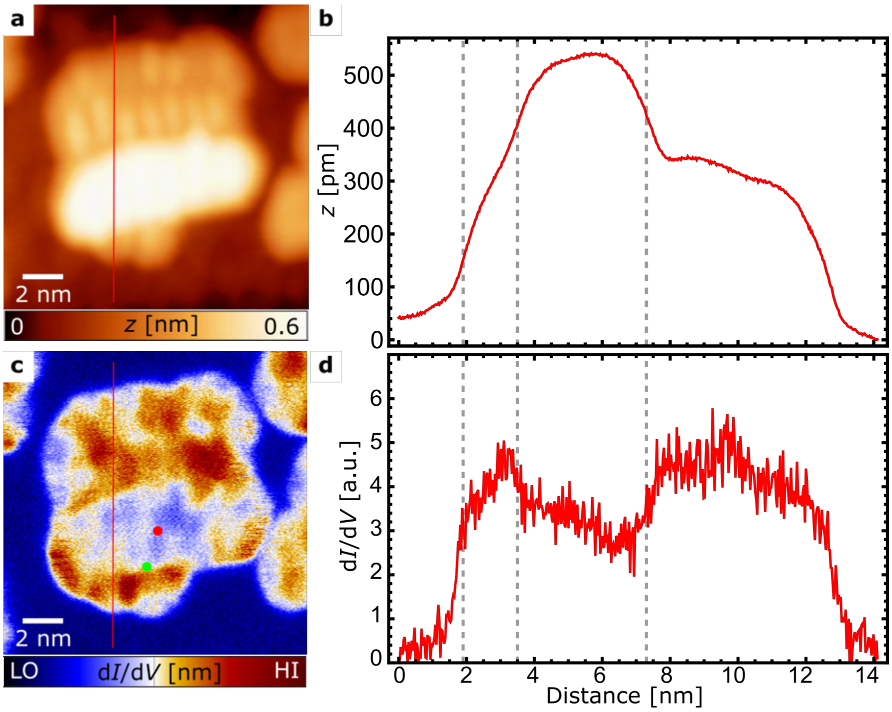

Figure 4.48: **a** STM image of a Fe island with a ML and coverage DL from figure Fig. 4.47. In **c** the corresponding dI/dV map is shown. The red lines shown in **a** and **c** indicate the locations of the topographic and Fermi level spectral weight profile lines shown in **b** and **d**, respectively. Measurement parameters for **a** are $I = 200\,\mathrm{pA}$, $V = 6\,\mathrm{mV}$, $T = 4.5\,\mathrm{K}$ and for **c** $V_{\mathrm{mod}} = 0.1\,\mathrm{mV}$, $V_{\mathrm{stab}} = 6\,\mathrm{mV}$.

shown in Fig. 4.49 **a** and **c**, it is noticeable that a state is localized directly on the edge even though no step to the first layer is present, as can be clearly seen in Fig. 4.49 **d**. It is therefore not obvious whether these edge states result from the underlying monolayer, or indeed come from the DL edge. The findings described here, in particular the fact that the double layer has a significantly lower spectral weight over the entire island than the type I monolayer and that it also shows almost continuous states at the edge, apply not only to the specific Fe island described here, but to all Fe islands found with double layers (see Fig. 4.46 **a**). Whether these are indications of Majorana edge modes on the edge of the DL cannot be clearly determined here. Hence, the edge states of the double layer would be good candidates for further investigations. Unfortunately, point spectroscopy on the edge states (where the double layer has a sharp edge towards the niobium) has not been performed so far, since the interesting features of the DL were notice only recently during the data analysis.

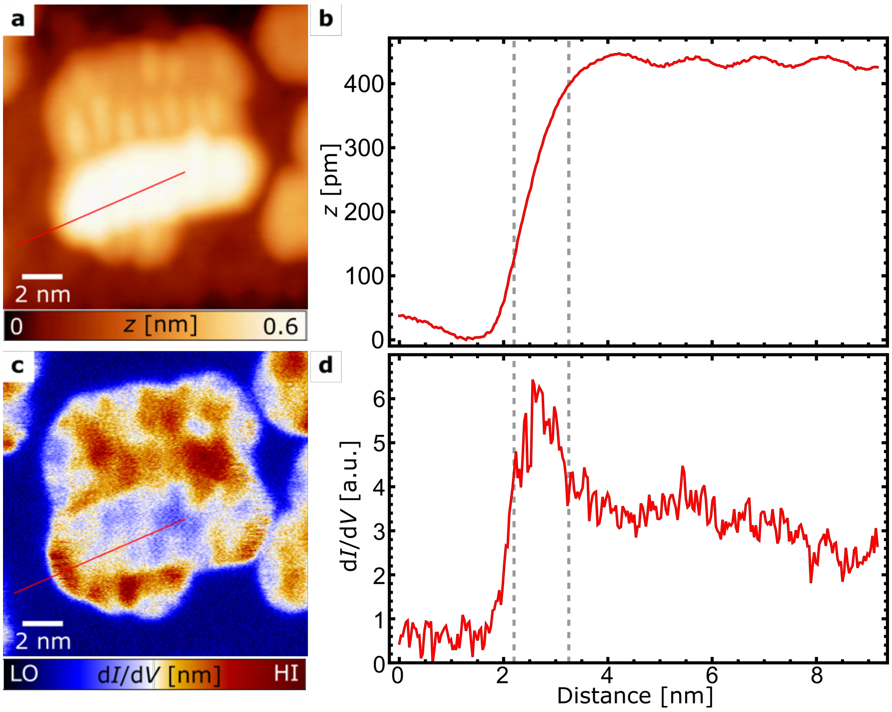

Figure 4.49: In **a** and **c** the same images are shown as in Fig. 4.48, but now the topographic and Fermi level spectral weight line profiles intersect the sharp edge of the Fe double layer next to niobium. In **b** and **d** the profile lines are shown analogous to Fig. 4.48. Measurement parameters for **a** are $I = 200\,\text{pA}$, $V = 6\,\text{mV}$, $T = 4.5\,\text{K}$ and for **c** $V_{\text{mod}} = 0.1\,\text{mV}$, $V_{\text{stab}} = 6\,\text{mV}$.

Chapter 5

Conclusion and Outlook

In the first part of this work, a procedure was developed to produce a clean Nb(111) surface, which was eventually achieved by a suitable treatment with hydrogen. Subsequently, the atomic structure of the clean Nb(111) surface was made visible for the first time via STM. This showed a reconstruction, whose occurrence can be explained theoretically by a premelting of the surface. Deposition of iron onto the cleaned Nb(111) surface subsequently showed the formation of iron clusters instead of monolayers, which is presumably due to the open surface of the reconstruction. In parallel with these investigations, the preparation and investigation of Fe/Nb(110) was started in the He-bath STM system, which proved to be more promising compared to Fe/Nb(111) and was therefore the focus in this thesis. Nevertheless, the Nb(111) surface has the potential to form a new platform for applications in the field of topologically nontrivial states, even though further research is needed to make the surface usable due to its reconstruction.

In the second part Fe/Nb(110) was investigated via STM/STS and SP-STM/SP-STS. For the first time, the atomic resolution of the three different reconstructions of ML Fe/Nb(110) were measured. Furthermore, the electronic and magnetic structure of the different monolayers and of the DL on type I were determined. An out-of-plane ferromagnetic monodomain structure was found for the three types of reconstructions with different coercivities, whereby the DL exhibited the same coercivity as the corresponding ML, which was type I in this case.
Moreover, low-energy STS measurements and $\mathrm{d}I/\mathrm{d}V$ maps showed Shiba bands with disorder for all the reconstructions, probably originating from the potential and magnetic scattering of the substrate electrons at the Fe lattice, which contains inhomogeneity in the topographic and electronic structure. Most likely due to the disorder, no edge states were found on the islands at the Fermi energy (see Chapter 2.4.3.3).
Despite the disorder in the monolayer, however, a significantly lower spectral weight was found over the entire area of the double layers at the Fermi energy, which might indicate the opening of a minigap. On the one hand, this could be due to shifts of Shiba bands to higher energies, and thus indicate a trivial minigap. On the other hand, an opening of a topologically nontrivial minigap of Shiba bands overlapping with E_F may be an alternative explanation. Moreover, the edge of the DL shows nearly continuous states around E_F. Whether there is evidence of Majorana states at the edge of the DL cannot be clearly determined in this work.
The results of this thesis thus provide a valuable contribution to the current discussion in the scientific community and in particular also show the difficulties that can arise when trying to construct an artificial two-dimensional topological superconductor. However,

the results also suggest a number of opportunities for further development, which will be sketched in the following.

First of all, it is obvious to continue the investigation of Fe/Nb(111), since magnetic material deposited on Nb(111) could potentially host magnetic skyrmionic states, due to the threefold symmetry, which itself could host Majorana edge modes. One could therefore first try to develop a method to form thin iron layers on Nb(111), which could possibly be based on a sequence of short flashes, whereby the number of flashes, their duration and temperature have to be explored experimentally. Alternatively, other magnetic materials could be vapor deposited, which might form monolayers on the Nb(111) surface more easily. In addition, there are a number of further studies of Fe on Nb(110) possible. First, measurements on the second layer Fe/Nb(110) should be continued to find further indications whether the edge states are exotic states or not. In this case, point spectroscopies for selected locations of the edge states could already give some information about the nature of the states.

In addition, the investigation of triple and higher layers of Fe would be interesting in order to analyze the correlation between the position of the Shiba bands in the gap, the magnetism and the coercivity.

Since the desired topological states probably did not appear in the measurements due to strong disorder effects, it would be interesting to try to reduce the disorder or to avoid it completely. In principle, this could be done by precise atomic manipulation, which would ideally allow the construction of a wide variety of 2D structures.

Another problem might be that the spin-orbit coupling in the investigated system was too weak to realize a p-wave gap. To investigate this dependence in more detail, intermediate layers of heavy elements could be incorporated. Perhaps Ir or Pt could serve as an intermediate element to enhance spin-orbit coupling and, due to the proximity effect, becoming superconducting. Another possibility to increase the spin-orbit coupling could be to build a cavity in the substrate by atomic manipulation and to embed the magnetic atoms in it.

In conclusion, this thesis shows essential measurements towards the development of an artificial two-dimensional topological superconductor, and, in particular, the difficulties that can arise in this development process. However, the results also show a number of promising opportunities for further developments, which could eventually form the basis for topological qubits.

Appendix A

Appendix

A.1 Magnetic Moment of an Atom

As mentioned in Sec. 2.2.1, we will briefly discuss the magnetic moment $\mathbf{m}$ of an atom in this section, which is quantum-mechanically an observable and fundamentally related to magnetism, since the sum of all magnetic moments per volume in a material is the total magnetization $\mathbf{M}$ [67, p. 4]. The magnetic moment $\mathbf{m}$ of an atom can be written as

$$\mathbf{m} = (\mathbf{m_L} + \mathbf{m_S}) = -\frac{\mu_B}{\hbar}(g_\mathrm{L}\mathbf{L}_\mathrm{tot} + g_S\mathbf{S}_\mathrm{tot}), \tag{A.1}$$

with the g-factors $g_\mathrm{L} \approx 1$, $g_\mathrm{S} \approx 2$ [67, p. 211], the Bohr magneton μ_B, the total orbital angular momentum operator $\mathbf{L}_\mathrm{tot}$ and the total spin operator $\mathbf{S}_\mathrm{tot}$. For a multi-electron system, it is essential to consider the sum over all individual electrons for the total orbital angular momentum and the total spin.

For a single electron, $\mathbf{L}$ is defined as the cross product of the position operator $\mathbf{r}$ and the momentum operator $\mathbf{p} = -i\hbar\nabla$ [145, p.73 ff.], i.e.

$$\mathbf{L} = (\mathbf{r} \times \mathbf{p}) = \begin{pmatrix} L_x \\ L_y \\ L_z \end{pmatrix} = i\hbar \begin{pmatrix} -(y\frac{\partial}{\partial z} - z\frac{\partial}{\partial y}) \\ (x\frac{\partial}{\partial z} - z\frac{\partial}{\partial x}) \\ -(x\frac{\partial}{\partial y} - y\frac{\partial}{\partial x}) \end{pmatrix}. \tag{A.2}$$

The individual components do not commute with each other. However, an arbitrary choice of one component of the operator $\mathbf{L}$ (L_x, L_y or L_z) and the related Casimir operator $\mathbf{L}^2 = L_x^2 + L_y^2 + L_z^2$ form a complete set of commuting observables with respect to the angular momentum. Thus, only one component of $\mathbf{L}$ and $\mathbf{L}^2$ are simultaneously measurable. Accordingly, the observed system is characterized by one component of $\mathbf{L}$ (usually L_z) and $\mathbf{L}^2$. The eigenvalues for L_z are $m_l\hbar$ and $l(l+1)\hbar^2$ for $\mathbf{L}^2$.

The spin operator $\mathbf{S}$ for a single electron is essentially described by the Pauli matrices $\boldsymbol{\sigma} = (\boldsymbol{\sigma}_x, \boldsymbol{\sigma}_y, \boldsymbol{\sigma}_z)$ and is defined as follows [145, p.91 ff.]:

$$\mathbf{S} = \begin{pmatrix} \boldsymbol{S}_x \\ \boldsymbol{S}_y \\ \boldsymbol{S}_z \end{pmatrix} = \frac{1}{2}\hbar \begin{pmatrix} \boldsymbol{\sigma}_x \\ \boldsymbol{\sigma}_y \\ \boldsymbol{\sigma}_z \end{pmatrix} \tag{A.3}$$

with

$$\boldsymbol{\sigma}_x = \begin{pmatrix} 0 & 1 \\ 1 & 0 \end{pmatrix}, \boldsymbol{\sigma}_y = \begin{pmatrix} 0 & -i \\ i & 0 \end{pmatrix}, \boldsymbol{\sigma}_z = \begin{pmatrix} 1 & 0 \\ 0 & -1 \end{pmatrix}. \tag{A.4}$$

Analogous to the orbital angular momentum, the individual components of the spin operator do not commute with each other, but a Casimir operator, $\mathbf{S}^2$, exists here as well. The eigenvalues are $m_s\hbar$ for S_z and $s(s+1)\hbar^2$ for $\mathbf{S}^2$. Combining both operators **L** and **S** (Russell-Saunders or LS coupling, see Fig. A.1 for a classical picture), we obtain the total angular momentum operator **J** [1]

$$\mathbf{J} = \mathbf{L} + \mathbf{S}. \tag{A.5}$$

Thus with the norm $\sqrt{\mathbf{J}^2} = \sqrt{J(J+1)}$ the length of the total magnetic moment **m** of an electron with the Landé-factor g_J [67, p. 210] can be described as

$$m = -g_J \mu_B \sqrt{J(J+1)}. \tag{A.6}$$

It should be mentioned here that if the spin-orbit coupling (see Sec. 2.2.1) can be neglected (e.g. for systems with light nuclei), **S** and **L** individually commute with the corresponding Hamilton operator [64, p. 25]. However, if the spin-orbit coupling cannot be neglected, then only **J** commutes with the Hamiltonian, i.e., only the total angular momentum is then a conserved quantity of the system, but not **L** or **S**. All eigenvalues of **S** and **L** form a multiplet, and the ground state of this multiplet can be determined by Hund's empirical rules [147, 148].

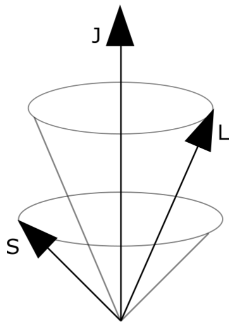

Figure A.1: Image of total angular momentum after H. Wolf [146].

A.2 Topology in Condensed Matter Physics

In this section, we briefly review the discovery and use of topological properties of solids. Until the 1980s it was thought that phase transitions of condensed matter can be described completely by symmetry breaking. However, it turned out that this was no longer possible with the quantum Hall effect (QHE) [149] discovered by von Klitzing. A new possibility of characterization had to be found. It turned out that with the help of topology such newly found properties could be described.

Topology is a field in mathematics, which deals with the classification of geometrical objects, mathematically defined as topological spaces [150, p.84]. The first obvious question is how such a classification can look like and how to judge whether two geometrical objects or topological spaces are topologically equivalent?

Two geometric objects are called topologically equivalent if one object can be transformed into the other under continuous deformation (homeomorphism [150, p.89]). For example, a cup can be transformed into a torus by stretching and compressing without closing the hole (handle of the cup). Or, considered from another perspective, one finds

---

[1] Matematically, these are of course two operators acting in different spaces. The total angular momentum operator must therefore be defined (strictly speaking) via the tensor product: $\mathbf{J} = \mathbf{L} \otimes \mathbb{1} + \mathbb{1} \otimes \mathbf{S}$. For the sake of simplicity, however, we use the usual notation (A.5).

closed paths on the surface of a torus, some of which pass through the hole of the torus (or handle in the case of the cup) and some others do not. If the torus is now deformed to a sphere, the hole must be closed and no more closed paths through the hole can be found. The geometric object has thus lost a topological property (the possibility of finding closed paths through a hole) and therefore the sphere and the torus are not topologically equivalent. Such a classification by a topological property is called *topological invariant* [75, p.933]. The next questions a solid state physicist now has to ask are: How can this mathematical concept of topology be transferred to solid state physics? What are the geometric structures or the topological spaces here and what are the continuous transformations? And, by which topological invariants can such spaces be distinguished and identified?

In 2016, Thouless, Haldane, and Kosterlitz won the Nobel Prize in Physics by successfully applying this mathematical concept of topology to physics. The Nobel Prize was awarded "*for theoretical discoveries of topological phase transitions and topological phases of matter*". In the next section we will briefly address how this concept is transferred to solid state physics.

A.3 Continuous Transformations, Topological Invariants and Classification of Topological States in Solid State Physics

As explained in the previous section, it is of interest how to apply the mathematical concept of topology concretely to solid-state physics. The analogies are the following: In solid state physics, the sum of the valence bands of a material in a phase exhibits a topological property. If we want to know whether two phases are topologically equivalent, a slow adiabatic change of the system by the Hamilton operator from one phase to the other must be possible. And with a suitable topological invariant (for example the Chern number), it is then possible to distinguish between different topological states.

So, first consider the time-dependent Hamilton operator $\mathbf{H}(\mathbf{R}(t))$, where $\mathbf{R}(t)$ are external parameters. At each time t a corresponding eigenvector $|\Psi_m(t)\rangle$ can be evolved, where m is the band index, or more figuratively, the eigenvector can be thought of as moving slowly, adiabatically in the parameter space (holonomy, see Fig. A.2). Now, if there is no degeneracy of the states, it is possible to obtain a dynamical phase $\phi_m(t)$ and a geometrical phase (also called Berry phase) $\gamma_m(t)$ of the final state [75, 87]:

$$|\Psi_m(\mathbf{R}(t_0)\rangle \rightarrow e^{i(\phi_m(t)+\gamma_m(t))}\, |\Psi_m(\mathbf{R}(t_0+T))\rangle \tag{A.7}$$

Here, analogous to the example with the torus described above, we are interested in closed paths in the parameter space such that $\mathbf{R}(t_0+T) = \mathbf{R}(t_0)$ holds. It can then be shown that the geometric phase, which can be written as follows using the Mead-Berry vector potential $\mathbf{A}_m(\mathbf{R}) = i\,\langle\Psi_m[\mathbf{R}(t)]|\nabla_\mathbf{R}|\Psi_m[\mathbf{R}(t)]\rangle$, is independent in time:

$$\gamma_m = \oint_\Gamma \mathbf{A}_m(\mathbf{R})d\mathbf{R}. \tag{A.8}$$

Thus, as just mentioned, γ_m, unlike the dynamic phase $\phi_m(t)$, is independent in time and depends only on the geometry of the parameter space and the path Γ. It is therefore called geometric or Berry phase. Furthermore, the closed path integral can be transformed by Stokes' theorem via the Berry flow $\mathbf{F}_m = \nabla_\mathbf{R} \times \mathbf{A}_m(\mathbf{R})$ into a surface integral

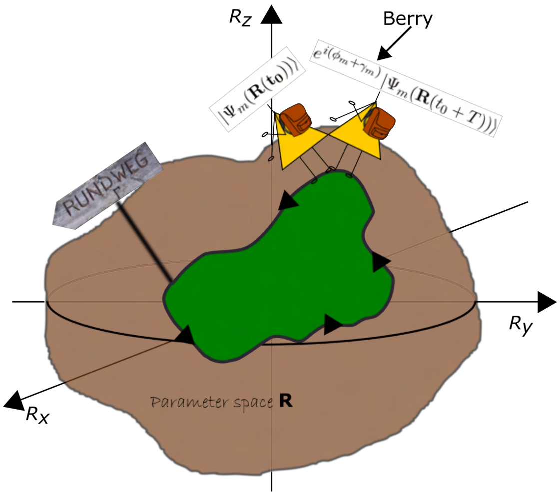

Figure A.2: An eigenvector moves along a closed path Γ in the parameter space $\mathbf{R}$ and picks up a dynamic and geometric phase. Inspired by [75].

with the surface S and the normal vector $\mathbf{n}$ on the surface:

$$\gamma_m = \oint_\Gamma \mathbf{A}_m(\mathbf{R})d\mathbf{R} = \int_S \mathbf{F}_m \cdot \mathbf{n}\ d^2R. \tag{A.9}$$

If the surface S is a closed manifold, then the integral shrinks to a multiple of 2π and we obtain Chern's theorem

$$C_m = \frac{1}{2\pi}\int_S \mathbf{F}_m(\mathbf{R}) \cdot \mathbf{n} d^2R. \tag{A.10}$$

Looking specifically at solid state physics, the Brillouin zone (BZ) can be considered as a parameter space, where integration over closed paths then corresponds to integration over a Brillouin zone. The eigenvectors are represented by Bloch wave functions, with the lattice periodic functions $u_m(\mathbf{k})$ being the basis functions, so the vector potential now gives $\mathbf{A}_m(\mathbf{k}) = i\,\langle u_m(\mathbf{k})|\nabla_{\mathbf{k}}|u_m(\mathbf{k})|u_m(\mathbf{k})|\nabla_{\mathbf{k}}|u_m(\mathbf{k})\rangle$. The sum C_m over all valence bands gives the total Chern number C, which represents a topological invariant in solid state physics and where different numbers for different topological phases can then be found and characterized,

$$C = \sum_{m=1}^{N} C_m = \frac{1}{2\pi}\sum_{m=1}^{N}\int_{BZ} \mathbf{F}_m(\mathbf{k}) \cdot \mathbf{n} d^2k. \tag{A.11}$$

Consider now a so-called topological insulator, which has a topology that can be characterized by the Chern number C=1 (the mathematical analog, i.e. the geometric structure in this case, is a torus). Now consider a second insulator which has a different topological structure that is characterized by the topological invariant C=0 (analogue to the mathematical geometrical structure of a sphere), whereas this insulator can also be simply vacuum or air. When these two different topological structures are brought into contact, at the boundary layer a special case arises where one must transition from the C=1 state to the other C=0 state. This transformation cannot happen adiabatically continuously, which in turn means that the band gap (hole in the torus) that exists in the volume must be closed at the surface. Accordingly, the topological insulator exhibits conducting states at its surface but not in its interior.

Similar to the topological insulator just described, superconductors can also be topological, i.e. have phases that have at least two different topological spaces. In the case of a topological p-wave SC, the topologically non-trivial phase is the p-wave SC with a p-wave Δ, while the trivial phase is the s-wave SC with an s-wave Δ.

A.4 Methods

A.4.1 Determination of the lattice spacing

In this work, two methods were used to determine the lattice site spacings from the experimental measurement data, which are described in more detail below.

A.4.1.1 Distance Measurement in Fourier Space via the program WSxM

The measured constant-current STM images were transformed with the program WSxM [151] into the Fourier space in which the resonance peaks can be investigated. An STM image of a hexagonal grid is shown as an example in Fig. A.3 **a** and the corresponding two-dimensional fast Fourier transform (2D FFT) image in Fig. A.3 **b**. From the intensity of the peaks along the origin line in the Fourier space the periodicity in the real space can be derived directly. This is due to the fact that the peaks originate from the constructive interference of the planar waves corresponding to the lattice phases[2] (see, e.g., [152]). Accordingly, when evaluating the resonance peaks (shown in Fig. A.3 **b**), the lattice geometry along the respective lattice directions must be taken into account. The coordinates of the peaks in the Fourier image are then obtained for a hexagonal lattice as a function of the lattice constant a as $\mathbf{k}_1 = (0, \frac{1}{\sqrt{3}a})$, $\mathbf{k}_2 = (\frac{1}{2a}, \frac{1}{2\sqrt{3}a})$ and $\mathbf{k}_3 = (\frac{1}{a}, 0)$. With the values for the peaks taken from the Fourier image, the following results are obtained for the lattice constants $a_1 = 0.41\,\mathrm{nm}$, $a_2 = 0.42\,\mathrm{nm}$ and $a_3 = 0.43\,\mathrm{nm}$, which reflect the lattice constants for the underlying lattice.

A.4.1.2 Distance Measurement in Real Space via MATLAB

For the measurement of the lattice spacing in real space, a program was written in MATLAB for this work, which simplifies and partially automates the evaluation. After the STM images have been loaded into MATLAB [153], the program can then be used to manually draw a straight line on the image. Using a predefined function (improfile), three profile lines are then extracted from the image, namely exactly along the straight line, as well as shifted by one pixel each. Fig. A.4 **a** shows an example of an STM image, where the blue line was drawn by hand and the red and green lines were calculated by parallel shifting of the blue line by one pixel each. This procedure was done for all measurable atomic rows in the image. After the profile lines are extracted from the topography images, the three parallel profile lines are averaged to reduce noise. Then the MatlLab function "findpeaks" is used to determine the position of the local maxima (see the blue triangles in Fig. A.4 **b**, indicating the peaks found by the program), which are then used to calculate the distances to the nearest neighbors. Finally, the mean value and the standard deviation are calculated from all distances determined in this way. This standardized evaluation method made it possible to measure and average up to 200 atomic distances per lattice direction and image them within a manageable

---

[2] For example, if $f(x)$ describes the position function of an atom with the Fourier transform $\tilde{f}(k)$ and one builds a lattice with it ($\sum_n f(x+na)$ with the lattice constant a), then the Fourier transform of it is $\tilde{f}(k)\sum_n e^{-2\pi i n a k}$

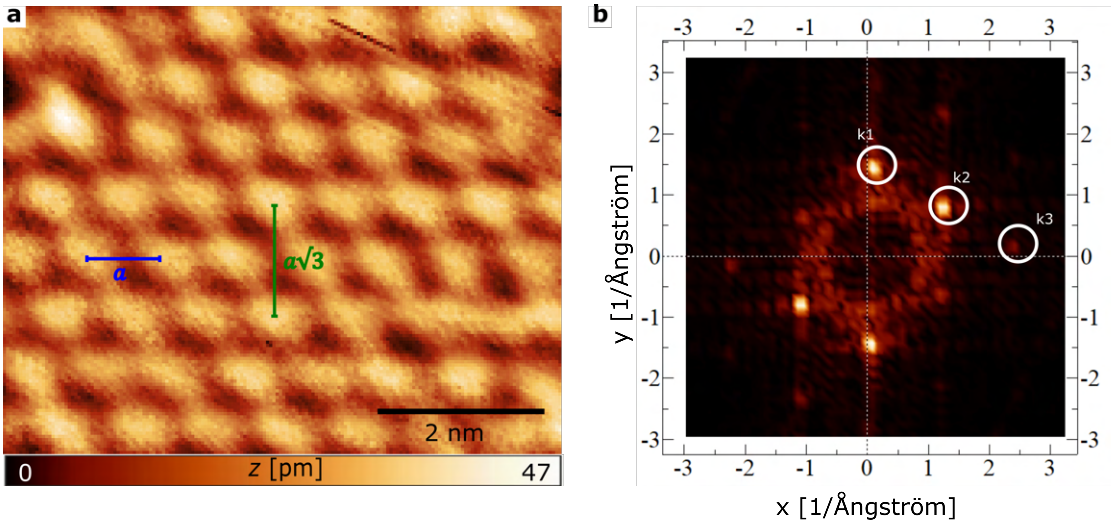

Figure A.3: In **a**, the hexagonal super-lattice of Nb(111) is shown in an STM topography image. Note, that the spacings of the atomic positions in the x and y directions are different, which must be taken into account when relating the k-vectors from the FFT in **b** to lattice constants.

amount of time.

A.4.2 Shifting of Maps and Extracting Data for the Hysteresis Loop

For the systematic and pixel-precise analysis of the measurement data, scripts were written in MATLAB and Mathematica for this work, using the library NanoLib [153] to load the data into MATLAB. In the following, some of the computational techniques will be explained. The evaluation of the magnetic measurement data was mainly performed with MATLAB, while Mathematica was primarily used for the visualization of the results.

Since it can happen that images of the same measurement region (taken one after the other) are shifted against each other or are slightly distorted (e.g. due to a slowly drifting or creeping scanner), it is often necessary to first check the images of a measurement series for the equality of the recorded region and, if necessary, to shift them against each other.

To extract the hysteresis curve from the $\mathrm{d}I/\mathrm{d}V$ maps, the maps of a closed magnetic loop were therefore first shifted relative to the first image in the loop so that they lie on top of each other. Fig. A.5 shows an example of the procedure. The pixel-precise displacement of an image **B** (relative to an image **A**) in x- and y-direction was calculated using the cross-correlation matrix $\mathbf{C} = \mathbf{A} * \mathbf{B}$ [3]. The resulting shifts $[x_{\text{offset}}, y_{\text{offset}}] = \max(\mathbf{C})$ do not reflect the actual shifts in some cases (the cross-correlation fails e.g. if there is too much "noise" due to the presence of hydrogen in the image), but they provide a good starting point to finally shift the images against each other manually. Therefore, a program was written in MATLAB, which first calculates the required shift based on the cross correlation and then allows a pixel-accurate manual shift through a graphical interface.

---

[3] Note, that to do this, the images **A** and **B** must of course be represented in their matrix form, where the matrix elements are given by the pixel values (gray values) of the images.

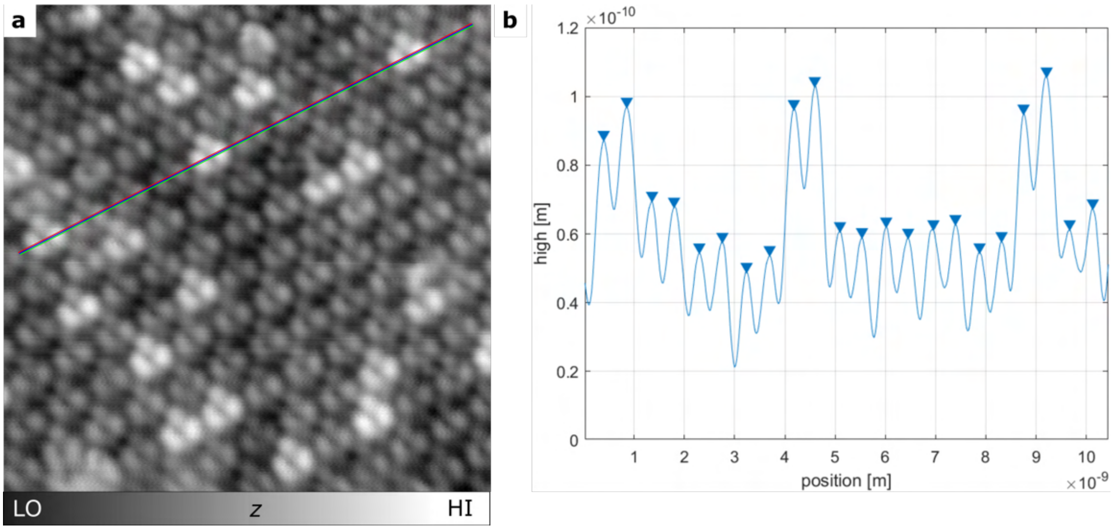

Figure A.4: In **a**, an atomic resolution STM image of Nb(111) is shown as an example, in which the three profile lines can be seen, which were averaged and plotted in **b**. In addition, the positions of the peaks, indicated by the blue triangles, were determined in order to calculate the distances between atomic sites.

After all the images had been shifted according to the first image, an area of interest was defined (drawn) on the first image (area outlined in blue in Fig. A.5). Exactly from this area of interest, the dI/dV data were extracted for all dI/dV maps of the loop, averaged for each map and plotted against the B-field at which the corresponding dI/dV map was recorded.

A.4.3 Spin asymmetry maps

In order to enhance the spin-resolved contrast obtained in the individual dI/dV maps $(\mathrm{d}I/\mathrm{d}V)_{ij}^{B_{z1}}$ and $(\mathrm{d}I/\mathrm{d}V)_{ij}^{B_{z2}}$ measured at different magnetic fields B_{z_1} and B_{z_2}, spin asymmetry maps were calculated by

$$\mathrm{asym}_{ij} = \frac{(\mathrm{d}I/\mathrm{d}V)_{ij}^{B_{z1}} - (\mathrm{d}I/\mathrm{d}V)_{ij}^{B_{z2}}}{(\mathrm{d}I/\mathrm{d}V)_{ij}^{B_{z1}} + (\mathrm{d}I/\mathrm{d}V)_{ij}^{B_{z2}}}. \tag{A.12}$$

Considering equation (2.19), equation (A.12) can now be simplified to:

$$\mathrm{asym}(V, \mathbf{r}_0) = P_t(E_\mathrm{F})P_s(E_\mathrm{F} + eV, \mathbf{r}_0). \tag{A.13}$$

With constant spin polarization of the tip, the spin asymmetry maps thus directly reflect the spin polarization of the sample at the location of the apex atom of the tip.
Here, as well, the dI/dV maps used for the calculation were shifted against each other, using the MATLAB script described in Sec. A.4.2.

A.4.4 Autocorrelation

For the analysis of the Shiba bands in Sec. 4.5, the autocorrelation of the dI/dV signal was calculated using a program written in Mathematica. The autocorrelation is intended to provide information about whether periodicities that are not readily apparent can be

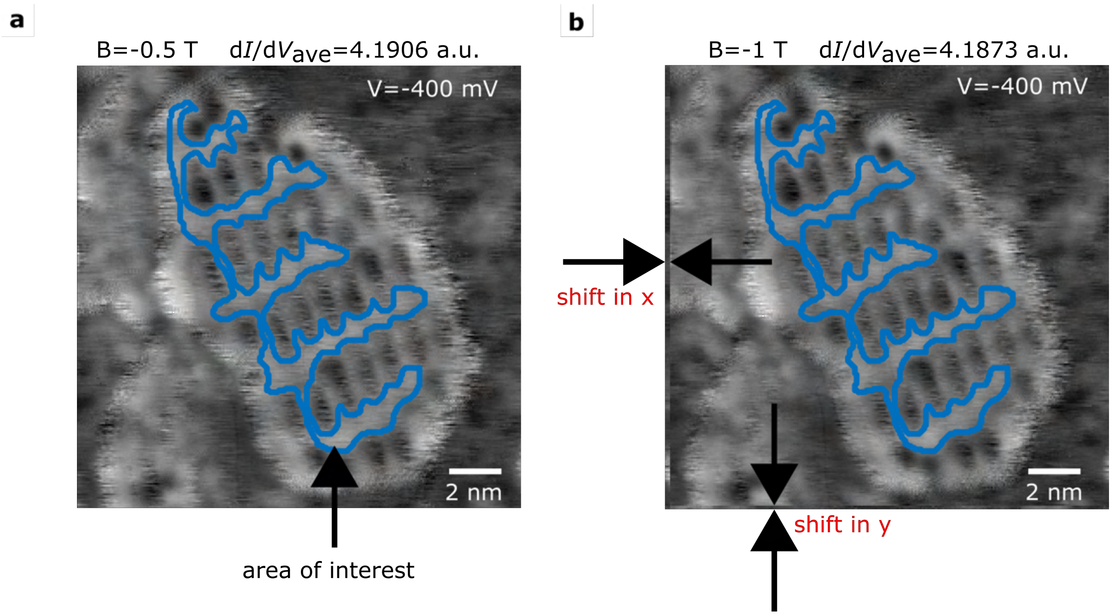

Figure A.5: In **a** the first $\mathrm{d}I/\mathrm{d}V$ map of the loop at $B = -0.5\,\mathrm{T}$ can be seen on which the area of interest was drawn, while in **b** the second $\mathrm{d}I/\mathrm{d}V$ map shifted relative to the first image can be seen.

found in images without long-range order. In addition, the strength of the correlation should be reflected in the band intensities of the different structures.
The autocorrelation functions of the spectroscopic line profiles shown in Sec. 4.5 were calculated by

$$\gamma_{V_{\mathrm{bias}}}(n) = \frac{1}{N}\sum_{i=1}^{N-n}\left((\mathrm{d}I/\mathrm{d}V)_{i+n} - \overline{(\mathrm{d}I/\mathrm{d}V)}\right)\left((\mathrm{d}I/\mathrm{d}V)_{i} - \overline{(\mathrm{d}I/\mathrm{d}V)}\right), \tag{A.14}$$

where $(\mathrm{d}I/\mathrm{d}V)_i$ is the differential tunneling conductance value (at point i of the spectroscopic line profile), $\overline{(\mathrm{d}I/\mathrm{d}V)}$ is the differential tunneling conductance averaged along the spectroscopic line profile, N is the total number of analyzed points along the spectroscopic line profile and n is the discrete (spatial) displacement factor.

A.5 Supporting Data

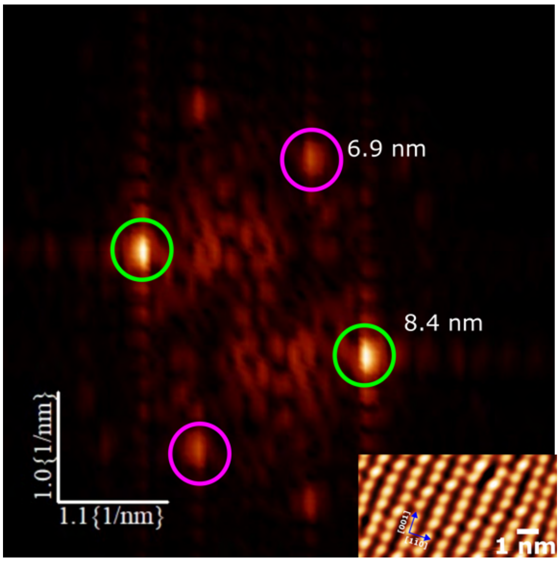

Figure A.6: Shown here is the FFT (see appendix A.4.1.1) of a type II Fe ML region (STM insert bottom right), which also yielded distances of 0.65 nm in the [001] direction and 0.82 nm in the [1$\bar{1}$0] direction.

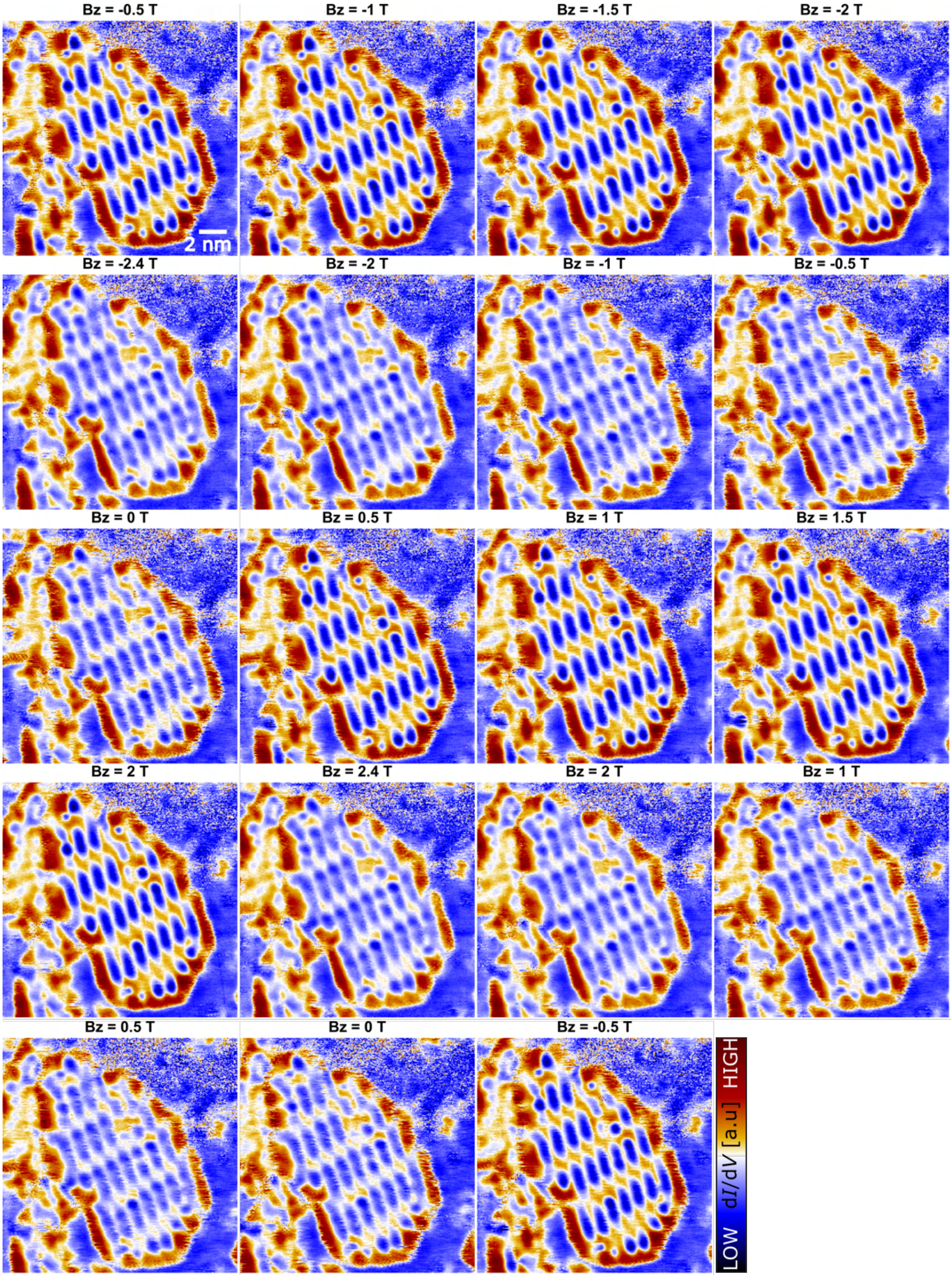

Figure A.7: As an example, a complete spin-resolved dI/dV map loop is shown here, from which the data for the hysteresis loops were extracted. The measurement starts at $B = -0.5\,\mathrm{T}$, goes down to $B = -2.4\,\mathrm{T}$, then up to $B = 2.4\,\mathrm{T}$ and ends again at $B = -0.5\,\mathrm{T}$. The magnetic field at which the maps were taken is written above each map. Measurement parameters are: $I = 1\,\mathrm{nA}$, $V = 400\,\mathrm{mV}$, $V_{\mathrm{mod}} = 10\,\mathrm{mV}$, $f = 1197\,\mathrm{Hz}$, $T = 4.5\,\mathrm{K}$ and $B_z = -0.5\,\mathrm{T}$.

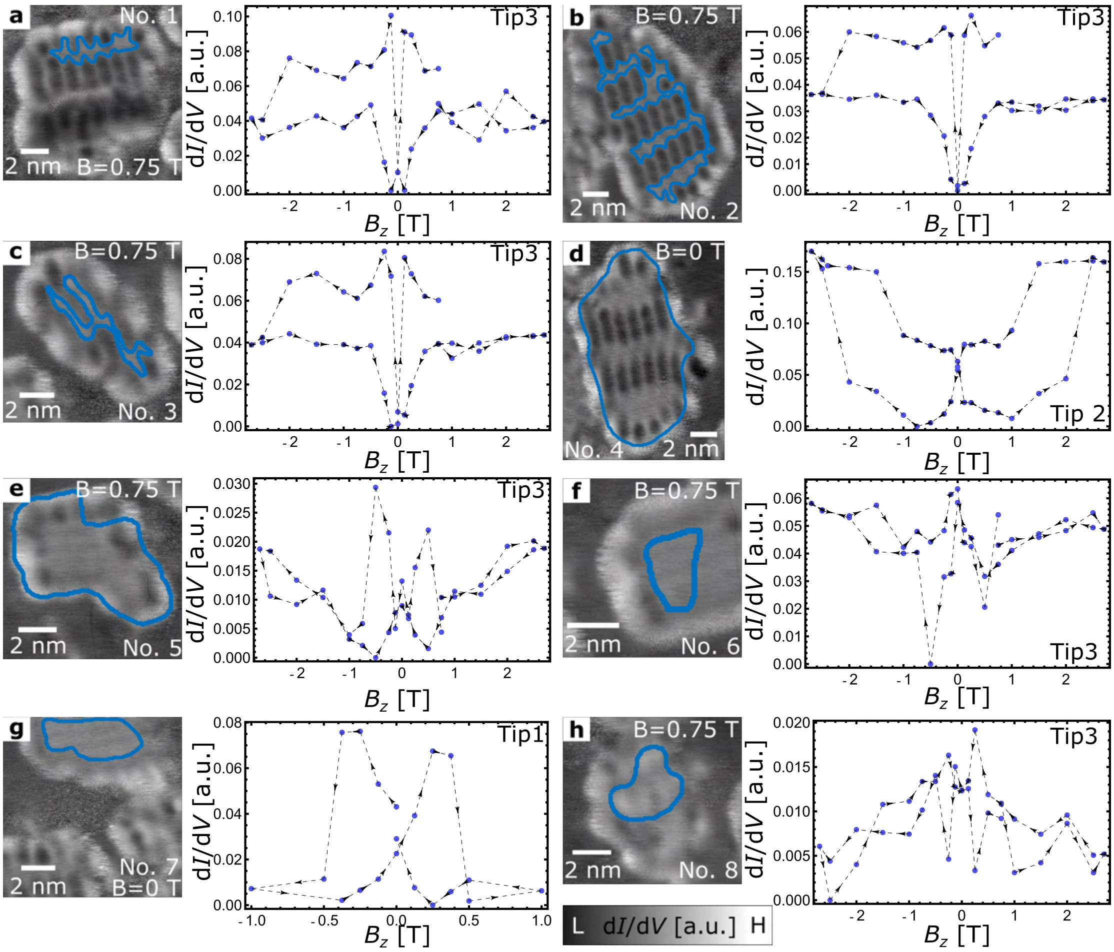

Figure A.8: Spin-resolved dI/dV maps of the different islands for which hysteresis loops have been measured. For tip 3 it should be noted that the loops were not finished. In order to simulate a complete loop one might mirror the data points at the y-axis. Measurement parameters are: $I = 1\,\mathrm{nA}$, $V_{\mathrm{mod}} = 10\,\mathrm{mV}$, $f = 1197\,\mathrm{Hz}$ and $T = 4.5\,\mathrm{K}$.

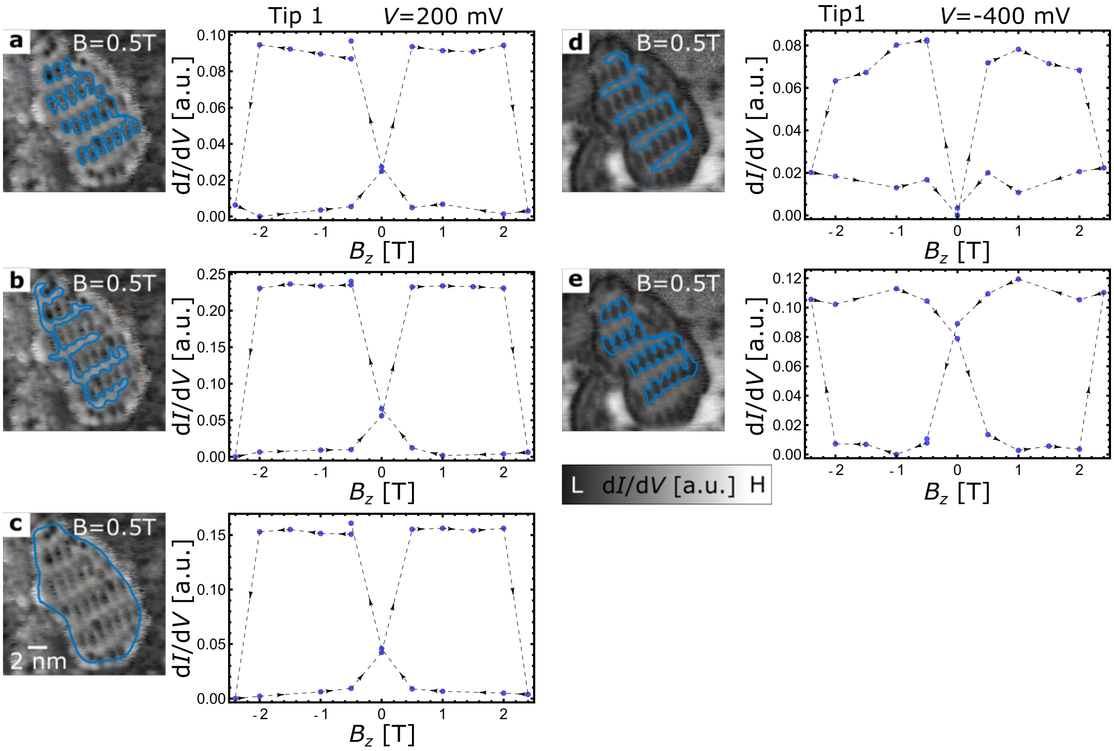

Figure A.9: Further magnetic hysteresis loops of Fe ML Type I at $V = 200\,\mathrm{mV}$ **a-c** and $V = -400\,\mathrm{mV}$ **d-e**. The measurements at $V = 200\,\mathrm{mV}$ show the same behaviour as at $V = 400\,\mathrm{mV}$, while no spin inversion is seen at $V = 200\,\mathrm{mV}$. Measurement parameters are: $I = 1\,\mathrm{nA}$, $V_{\mathrm{mod}} = 10\,\mathrm{mV}$, $f = 1197\,\mathrm{Hz}$ and $T = 4.5\,\mathrm{K}$..

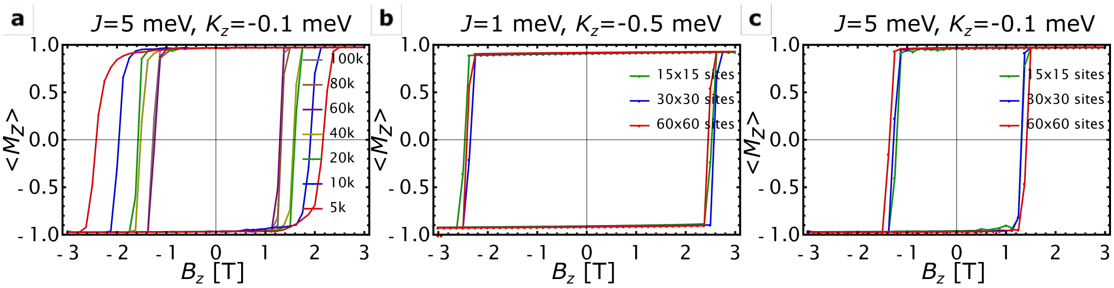

Figure A.10: Simulations with different step sizes are shown in **a**. It is noticeable that the switching behaviour of the magnetization of the island remains the same with a step size of 60k or more. However, with decreasing step sizes, the apparent coercivity increases. In other words, with low step sizes, the island does not have enough time to switch its magnetization by statistical processes, such that with a very small step size, the applied magnetic field changes during the switching process, which can also be seen in the characteristic curvature of the hysteresis curve. In **b** and **c** the simulation results with different island sizes, at different values of J_1 and K_z are shown. It can be seen that to a good approximation the switching behaviour is size-independent.

Bibliography

[1] T. D. Ladd, F. Jelezko, R. Laflamme, Y. Nakamura, C. Monroe and J. L. O'Brien, *Quantum computers*, Nature **464** (2010), no. 7285 45–53.

[2] M. A. Nielsen and I. L. Chuang, *Quantum Computation and Quantum Information: 10th Anniversary Edition.* Cambridge University Press, 2010.

[3] L. Alchieri, D. Badalotti, P. Bonardi and S. Bianco, *An introduction to quantum machine learning: from quantum logic to quantum deep learning*, Quantum Machine Intelligence **3** (2021) 1–30.

[4] H.-Y. Huang, M. Broughton, M. Mohseni, R. Babbush, S. Boixo, H. Neven and J. R. McClean, *Power of data in quantum machine learning*, Nature communications **12** (2021), no. 1 2631.

[5] Y. Cao, J. Romero and A. Aspuru-Guzik, *Potential of quantum computing for drug discovery*, IBM Journal of Research and Development **62** (2018), no. 6 6:1–6:20. doi:10.1147/JRD.2018.2888987.

[6] K. Batra, K. M. Zorn, D. H. Foil, E. Minerali, V. O. Gawriljuk, T. R. Lane and S. Ekins, *Quantum Machine Learning Algorithms for Drug Discovery Applications*, Journal of Chemical Information and Modeling **61** (2021), no. 6 2641–2647. doi:10.1021/acs.jcim.1c00166.

[7] S. Lloyd, *Universal Quantum Simulators*, Science **273** (1996), no. 5278 1073–1078.

[8] P. Ball, *First 100-Qubit Quantum Computer enters Crowded Race*, Nature **599** (November, 2021) 542.

[9] C. Psaroudaki and C. Panagopoulos, *Skyrmion Qubits: A New Class of Quantum Logic Elements Based on Nanoscale Magnetization*, Phys. Rev. Lett. **127** (Aug, 2021) 067201. doi:10.1103/PhysRevLett.127.067201.

[10] A. Kitaev, *Fault-tolerant quantum computation by anyons*, Annals of Physics **303** (jan, 2003) 2–30. doi:10.1016/S0003-4916(02)00018-0.

[11] M. H. Freedman, *Quantum computation and the localization of modular functors*, Foundations of Computational Mathematics **1** (2001), no. 2 183–204.

[12] B. Field and T. Simula, *Introduction to topological quantum computation with non-Abelian anyons*, Quantum Science and Technology **3** (jul, 2018) 045004. doi:10.1088/2058-9565/aacad2.

[13] F. von Oppen, Y. Peng and F. Pientka, *Topological Superconducting Phases in One Dimension: Lecture Notes of the Les Houches Summer School.* Oxford Univ. Press, 2014.

[14] J. Alicea, *New directions in the pursuit of Majorana fermions in solid state systems*, Reports on Progress in Physics **75** (jun, 2012) 076501. doi:10.1088/0034-4885/75/7/076501.

[15] F. Wilczek, *Majorana returns*, Nature Physics **5** (2009), no. 9 614–618.

[16] C. Beenakker, *Search for Majorana Fermions in Superconductors*, Annual Review of Condensed Matter Physics **4** (2013), no. 1 113–136. doi:10.1146/annurev-conmatphys-030212-184337 [`arXiv:https://doi.org/10.1146/annurev-conmatphys-030212-184337`].

[17] S. Das Sarma, C. Nayak and S. Tewari, *Proposal to stabilize and detect half-quantum vortices in strontium ruthenate thin films: Non-Abelian braiding statistics of vortices in a $p_x + ip_y$ superconductor*, Phys. Rev. B **73** (Jun, 2006) 220502. doi:10.1103/PhysRevB.73.220502.

[18] V. Mourik, K. Zuo, S. M. Frolov, S. R. Plissard, E. P. A. M. Bakkers and L. P. Kouwenhoven, *Signatures of Majorana Fermions in Hybrid Superconductor-Semiconductor Nanowire Devices*, Science **336** (2012), no. 6084 1003–1007. doi:10.1126/science.1222360 [`arXiv:https://www.science.org/doi/pdf/10.1126/science.1222360`].

[19] J. Alicea, *Majorana fermions in a tunable semiconductor device*, Phys. Rev. B **81** (Mar, 2010) 125318. doi:10.1103/PhysRevB.81.125318.

[20] S. M. Albrecht, A. P. Higginbotham, M. Madsen, F. Kuemmeth, T. S. Jespersen, J. Nygård, P. Krogstrup and C. Marcus, *Exponential protection of zero modes in Majorana islands*, Nature **531** (2016), no. 7593 206–209.

[21] S. Nadj-Perge, I. K. Drozdov, J. Li, H. Chen, S. Jeon, J. Seo, A. H. MacDonald, B. A. Bernevig and A. Yazdani, *Observation of Majorana fermions in ferromagnetic atomic chains on a superconductor*, Science **346** (2014), no. 6209 602–607.

[22] S. Jeon, Y. Xie, J. Li, Z. Wang, B. A. Bernevig and A. Yazdani, *Distinguishing a Majorana zero mode using spin-resolved measurements*, Science **358** (2017), no. 6364 772–776. doi:10.1126/science.aan3670 [`arXiv:https://www.science.org/doi/pdf/10.1126/science.aan3670`].

[23] H. Kim, A. Palacio-Morales, T. Posske, L. Rózsa, K. Palotás, L. Szunyogh, M. Thorwart and R. Wiesendanger, *Toward tailoring Majorana bound states in artificially constructed magnetic atom chains on elemental superconductors*, Science Advances **4** (2018), no. 5 eaar5251. doi:10.1126/sciadv.aar5251 [`arXiv:https://www.science.org/doi/pdf/10.1126/sciadv.aar5251`].

[24] M. Ruby, B. W. Heinrich, J. I. Pascual and K. J. Franke, *Experimental Demonstration of a Two-Band Superconducting State for Lead Using Scanning Tunneling Spectroscopy*, Phys. Rev. Lett. **114** (Apr, 2015) 157001. doi:10.1103/PhysRevLett.114.157001.

[25] D. Wang, L. Kong, P. Fan, H. Chen, S. Zhu, W. Liu, L. Cao, Y. Sun, S. Du, J. Schneeloch, R. Zhong, G. Gu, L. Fu, H. Ding and H.-J. Gao, *Evidence for Majorana bound states in an iron-based superconductor*, Science **362** (2018), no. 6412 333–335. doi:10.1126/science.aao1797 [`arXiv:https://www.science.org/doi/pdf/10.1126/science.aao1797`].

[26] Q. Liu, C. Chen, T. Zhang, R. Peng, Y.-J. Yan, C.-H.-P. Wen, X. Lou, Y.-L. Huang, J.-P. Tian, X.-L. Dong, G.-W. Wang, W.-C. Bao, Q.-H. Wang, Z.-P. Yin, Z.-X. Zhao and D.-L. Feng, *Robust and Clean Majorana Zero Mode in the Vortex Core of High-Temperature Superconductor* $(\mathrm{Li}_{0.84}\mathrm{Fe}_{0.16})\mathrm{OHFeSe}$, Phys. Rev. X **8** (Dec, 2018) 041056. doi:10.1103/PhysRevX.8.041056.

[27] L. Kong, S. Zhu, M. Papaj, H. Chen, L. Cao, H. Isobe, Y. Xing, W. Liu, D. Wang, P. Fan *et. al.*, *Half-integer level shift of vortex bound states in an iron-based superconductor*, Nature Physics **15** (2019), no. 11 1181–1187.

[28] J. Röntynen and T. Ojanen, *Chern mosaic: Topology of chiral superconductivity on ferromagnetic adatom lattices*, Phys. Rev. B **93** (Mar, 2016) 094521. doi:10.1103/PhysRevB.93.094521.

[29] J. Li, T. Neupert, Z. Wang, A. H. Macdonald, A. Yazdani and B. A. Bernevig, *Two-dimensional chiral topological superconductivity in Shiba lattices*, Nature Communications **7** (2016) 1–7. doi:10.1038/ncomms12297.

[30] S. Rachel, E. Mascot, S. Cocklin, M. Vojta and D. K. Morr, *Quantized charge transport in chiral Majorana edge modes*, Phys. Rev. B **96** (Nov, 2017) 205131. doi:10.1103/PhysRevB.96.205131.

[31] S. Nakosai, Y. Tanaka and N. Nagaosa, *Two-dimensional p-wave superconducting states with magnetic moments on a conventional s-wave superconductor*, Phys. Rev. B **88** (Nov, 2013) 180503. doi:10.1103/PhysRevB.88.180503.

[32] W. Chen and A. P. Schnyder, *Majorana edge states in superconductor-noncollinear magnet interfaces*, Phys. Rev. B **92** (Dec, 2015) 214502. doi:10.1103/PhysRevB.92.214502.

[33] A. O. Zlotnikov, M. S. Shustin and A. D. Fedoseev, *Aspects of Topological Superconductivity in 2D Systems: Noncollinear Magnetism, Skyrmions, and Higher-order Topology*, Journal of Superconductivity and Novel Magnetism **34** (2021), no. 12 3053–3088.

[34] S. S. Pershoguba, S. Nakosai and A. V. Balatsky, *Skyrmion-induced bound states in a superconductor*, Phys. Rev. B **94** (Aug, 2016) 064513. doi:10.1103/PhysRevB.94.064513.

[35] G. Yang, P. Stano, J. Klinovaja and D. Loss, *Majorana bound states in magnetic skyrmions*, Phys. Rev. B **93** (Jun, 2016) 224505. doi:10.1103/PhysRevB.93.224505.

[36] N. Mohanta, S. Okamoto and E. Dagotto, *Skyrmion control of Majorana states in planar Josephson junctions*, Communications Physics **4** (2021), no. 1 163.

[37] E. Mascot, J. Bedow, M. Graham, S. Rachel and D. K. Morr, *Topological superconductivity in skyrmion lattices*, npj Quantum Materials **6** (2021), no. 1 6.

[38] A. Palacio-Morales, E. Mascot, S. Cocklin, H. Kim, S. Rachel, D. K. Morr and R. Wiesendanger, *Atomic-scale interface engineering of Majorana edge modes in a 2D magnet-superconductor hybrid system*, Science Advances **5** (2019), no. 7 eaav6600. doi:10.1126/sciadv.aav6600 [`arXiv:https://www.science.org/doi/pdf/10.1126/sciadv.aav6600`].

[39] H. Zhang, C.-X. Liu, S. Gazibegovic, D. Xu, J. A. Logan, G. Wang, N. van Loo, J. D. Bommer, M. W. de Moor, D. Car *et. al.*, *Retraction note: Quantized majorana conductance*, Nature **591** (2021), no. 7851 E30–E30.

[40] P. Yu, J. Chen, M. Gomanko, G. Badawy, E. Bakkers, K. Zuo, V. Mourik and S. Frolov, *Non-Majorana states yield nearly quantized conductance in proximatized nanowires*, Nature Physics **17** (2021), no. 4 482–488.

[41] H. Pan, W. S. Cole, J. D. Sau and S. Das Sarma, *Generic quantized zero-bias conductance peaks in superconductor-semiconductor hybrid structures*, Phys. Rev. B **101** (Jan, 2020) 024506. doi:10.1103/PhysRevB.101.024506.

[42] S. Frolov, *Quantum computing's reproducibility crisis: Majorana fermions*, 2021.

[43] P. Beck, L. Schneider, L. Rózsa, K. Palotás, A. Lászlóffy, L. Szunyogh, J. Wiebe and R. Wiesendanger, *Spin-orbit coupling induced splitting of Yu-Shiba-Rusinov states in antiferromagnetic dimers*, Nature Communications **12** (2021), no. 1 2040.

[44] L. Schneider, P. Beck, T. Posske, D. Crawford, E. Mascot, S. Rachel, R. Wiesendanger and J. Wiebe, *Topological Shiba bands in artificial spin chains on superconductors*, Nature Physics **17** (2021), no. 8 943–948.

[45] L. Schneider, P. Beck, J. Neuhaus-Steinmetz, L. Rózsa, T. Posske, J. Wiebe and R. Wiesendanger, *Precursors of Majorana modes and their length-dependent energy oscillations probed at both ends of atomic Shiba chains*, Nature Nanotechnology **17** (2022) 384–389.

[46] G. Binnig, C. F. Quate and C. Gerber, *Atomic Force Microscope*, Phys. Rev. Lett. **56** (Mar, 1986) 930–933. doi:10.1103/PhysRevLett.56.930.

[47] E. A. Ash and G. Nicholls, *Super-resolution Aperture Scanning Microscope*, Nature **237** (1972) 510–512. doi:10.1038/237510a0.

[48] G. Binnig, H. Rohrer, C. Gerber and E. Weibel, *Surface Studies by Scanning Tunneling Microscopy*, Phys. Rev. Lett. **49** (Jul, 1982) 57–61. doi:10.1103/PhysRevLett.49.57.

[49] R. Wiesendanger, *Spin mapping at the nanoscale and atomic scale*, Rev. Mod. Phys. **81** (Nov, 2009) 1495–1550. doi:10.1103/RevModPhys.81.1495.

[50] C. J. Chen. Oxford University Press, 2007. doi:10.1093/acprof:oso/9780199211500.001.0001.

[51] R. Wiesendanger, *Scanning Probe Microscopy and Spectroscopy: Methods and Applications.* Cambridge University Press, 1994.

[52] J. Bardeen, *Tunnelling from a Many-Particle Point of View*, Phys. Rev. Lett. **6** (Jan, 1961) 57–59. doi:10.1103/PhysRevLett.6.57.

[53] R. Wiesendanger, *Spin mapping at the nanoscale and atomic scale*, Reviews of Modern Physics **81** (2009), no. 4 1495.

[54] J. Tersoff and D. R. Hamann, *Theory and Application for the Scanning Tunneling Microscope*, Phys. Rev. Lett. **50** (Jun, 1983) 1998–2001. doi:10.1103/PhysRevLett.50.1998.

[55] R. Hamers, *Atomic-resolution surface spectroscopy with the scanning tunneling microscope*, Annual Review of Physical Chemistry **40** (1989), no. 1 531–559.

[56] E. C. Stoner, *Collective electron ferromagnetism*, Proceedings of the Royal Society of London. Series A. Mathematical and Physical Sciences **165** (1938), no. 922 372–414. doi:10.1098/rspa.1938.0066 [`arXiv:https://royalsocietypublishing.org/doi/pdf/10.1098/rspa.1938.0066`].

[57] D. Wortmann, S. Heinze, P. Kurz, G. Bihlmayer and S. Blügel, *Resolving Complex Atomic-Scale Spin Structures by Spin-Polarized Scanning Tunneling Microscopy*, Phys. Rev. Lett. **86** (Apr, 2001) 4132–4135. doi:10.1103/PhysRevLett.86.4132.

[58] M. Julliere, *Tunneling between ferromagnetic films*, Physics Letters A **54** (1975), no. 3 225–226. doi:https://doi.org/10.1016/0375-9601(75)90174-7.

[59] R. Wiesendanger, H.-J. Güntherodt, G. Güntherodt, R. J. Gambino and R. Ruf, *Observation of vacuum tunneling of spin-polarized electrons with the scanning tunneling microscope*, Phys. Rev. Lett. **65** (Jul, 1990) 247–250. doi:10.1103/PhysRevLett.65.247.

[60] S. H. Pan, E. W. Hudson and J. C. Davis, *Vacuum tunneling of superconducting quasiparticles from atomically sharp scanning tunneling microscope tips*, Applied Physics Letters **73** (1998), no. 20 2992–2994. doi:10.1063/1.122654 [`arXiv:https://doi.org/10.1063/1.122654`].

[61] M. Tinkham, *Introduction to Superconductivity.* Dover Publications, Inc., 1996.

[62] B. Josephson, *Possible new effects in superconductive tunnelling*, Physics Letters **1** (1962), no. 7 251–253. doi:https://doi.org/10.1016/0031-9163(62)91369-0.

[63] B. D. Josephson, *The discovery of tunnelling supercurrents*, Rev. Mod. Phys. **46** (Apr, 1974) 251–254. doi:10.1103/RevModPhys.46.251.

[64] W. Nolting and A. Ramakanth, *Quantum Theory of Magnetism.* Springer, Berlin, Heidelberg, 2009.

[65] J. Hubbard and B. H. Flowers, *Electron correlations in narrow energy bands*, Proceedings of the Royal Society of London. Series A. Mathematical and Physical Sciences **276** (1963), no. 1365 238–257. doi:10.1098/rspa.1963.0204 [`arXiv:https://royalsocietypublishing.org/doi/pdf/10.1098/rspa.1963.0204`].

[66] Y. A. Bychkov and E. I. Rashba, *Oscillatory effects and the magnetic susceptibility of carriers in inversion layers*, Journal of Physics C: Solid State Physics **17** (nov, 1984) 6039. doi:10.1088/0022-3719/17/33/015.

[67] S. Blundell, *Magnetism in Condensed Matter.* Oxford University Press, 2003.

[68] G. Czycholl, *Theoretische Festkörperphysik Band 2.* Springer Spektrum, 2017.

[69] W. Heisenberg, *Zur Theorie des Ferromagnetismus*, Zeitschrift für Physik **49** (Mai, 1928) 619–636.

[70] S. Blügel, *C 1 Reduced Dimensions I : Magnetic Moment and Magnetic Structure.* Forschungszentrum Jülich, 2005.

[71] F. Delgado, S. Loth, M. Zielinski and J. Fernández-Rossier, *The emergence of classical behaviour in magnetic adatoms*, Europhysics Letters **109** (mar, 2015) 57001. doi:10.1209/0295-5075/109/57001.

[72] A. Belabbes, G. Bihlmayer, F. Bechstedt, S. Blügel and A. Manchon, *Hund's Rule-Driven Dzyaloshinskii-Moriya Interaction at* $3d-5d$ *Interfaces*, Phys. Rev. Lett. **117** (Dec, 2016) 247202. doi:10.1103/PhysRevLett.117.247202.

[73] H. Kamerlingh Onnes, *The Superconductivity of Mercury*, Commun. Phys. Lab. Univ. Leiden **120-124** (1911).

[74] W. Meissner and R. Ochsenfeld, *Ein neuer Effekt bei Eintritt der Supraleitfähigkeit*, Naturwissenschaften **21** (Nov, 1933) 787–788. doi:10.1007/BF01504252.

[75] R. Gross and A. Marx, *Festkörperphysik.* Oldenbourg Wissenschaftsverlag, 2018.

[76] F. London, H. London and F. A. Lindemann, *The electromagnetic equations of the supraconductor*, Proceedings of the Royal Society of London. Series A - Mathematical and Physical Sciences **149** (1935), no. 866 71–88. doi:10.1098/rspa.1935.0048 [`arXiv:https://royalsocietypublishing.org/doi/pdf/10.1098/rspa.1935.0048`].

[77] J. Bardeen, L. N. Cooper and J. R. Schrieffer, *Theory of Superconductivity*, Phys. Rev. **108** (Dec, 1957) 1175–1204. doi:10.1103/PhysRev.108.1175.

[78] L. N. Cooper, *Bound Electron Pairs in a Degenerate Fermi Gas*, Phys. Rev. **104** (Nov, 1956) 1189–1190. doi:10.1103/PhysRev.104.1189.

[79] H. Fröhlich, *Interaction of electrons with lattice vibrations*, Proceedings of the Royal Society of London. Series A. Mathematical and Physical Sciences **215** (1952), no. 1122 291–298. doi:10.1098/rspa.1952.0212 [`arXiv:https://royalsocietypublishing.org/doi/pdf/10.1098/rspa.1952.0212`].

[80] J. Bardeen and D. Pines, *Electron-Phonon Interaction in Metals*, Phys. Rev. **99** (Aug, 1955) 1140–1150. doi:10.1103/PhysRev.99.1140.

[81] N. N. Bogoljubov, *On a new method in the theory of superconductivity*, Il Nuovo Cimento (1955-1965) **7** (March, 1958) 794–805. doi:10.1007/BF02745585.

[82] J. G. Valatin, *Comments on the theory of superconductivity*, Il Nuovo Cimento (1955-1965) **7** (March, 1958) 843–857. doi:10.1007/BF02745589.

[83] R. C. Dynes, V. Narayanamurti and J. P. Garno, *Direct Measurement of Quasiparticle-Lifetime Broadening in a Strong-Coupled Superconductor*, Phys. Rev. Lett. **41** (Nov, 1978) 1509–1512. doi:10.1103/PhysRevLett.41.1509.

[84] E. Majorana, *Teoria simmetrica dell'elettrone e del positrone*, Il Nuovo Cimento (1924-1942) **14** (1937), no. 4 171–184.

[85] B. A. Bernevig, *Topological Insulators and Topological Superconductors.* Princeton University Press, 2013.

[86] A. Y. Kitaev, *Unpaired Majorana fermions in quantum wires*, Physics-Uspekhi **44** (oct, 2001) 131–136. doi:10.1070/1063-7869/44/10s/s29.

[87] J. Röntynen, *Topological superconductivity in magnetic adatom lattices.* Aalto University publication series DOCTORAL DISSERTATIONS, 2016.

[88] L. Fu and C. L. Kane, *Superconducting Proximity Effect and Majorana Fermions at the Surface of a Topological Insulator*, Phys. Rev. Lett. **100** (Mar, 2008) 096407. doi:10.1103/PhysRevLett.100.096407.

[89] L. Fu and C. L. Kane, *Josephson current and noise at a superconductor/quantum-spin-Hall-insulator/superconductor junction*, Phys. Rev. B **79** (Apr, 2009) 161408. doi:10.1103/PhysRevB.79.161408.

[90] A. I. Buzdin, *Proximity effects in superconductor-ferromagnet heterostructures*, Rev. Mod. Phys. **77** (Sep, 2005) 935–976. doi:10.1103/RevModPhys.77.935.

[91] S. D. Sarma, M. Freedman and C. Nayak, *Majorana zero modes and topological quantum computation*, npj Quantum Information **1** (2015), no. 1 1–13.

[92] M. Leijnse and K. Flensberg, *Introduction to topological superconductivity and Majorana fermions*, Semiconductor Science and Technology **27** (nov, 2012) 124003. doi:10.1088/0268-1242/27/12/124003.

[93] S. Loth, S. Baumann, C. P. Lutz, D. M. Eigler and A. J. Heinrich, *Bistability in Atomic-Scale Antiferromagnets*, Science **335** (2012), no. 6065 196–199. doi:10.1126/science.1214131 [`arXiv:https://www.science.org/doi/pdf/10.1126/science.1214131`].

[94] M. Menzel, A. Kubetzka, K. von Bergmann and R. Wiesendanger, *Parity Effects in 120° Spin Spirals*, Phys. Rev. Lett. **112** (Jan, 2014) 047204. doi:10.1103/PhysRevLett.112.047204.

[95] A. V. Balatsky, I. Vekhter and J.-X. Zhu, *Impurity-induced states in conventional and unconventional superconductors*, Rev. Mod. Phys. **78** (May, 2006) 373–433. doi:10.1103/RevModPhys.78.373.

[96] L. Yu, *Bound state in superconductors with paramagnetic impurities*, Acta Physica Sinica **21** (Aug, 1965) 75.

[97] H. Shiba, *Classical Spins in Superconductors*, Progress of Theoretical Physics **40** (09, 1968) 435–451. doi:10.1143/PTP.40.435 [`arXiv:https://academic.oup.com/ptp/article-pdf/40/3/435/5185550/40-3-435.pdf`].

[98] A. Rusinov, *Superconductivity near a paramagnetic impurity*, Eksp. Teor. Fiz **9** (1968) 146.

[99] J. Röntynen and T. Ojanen, *Topological Superconductivity and High Chern Numbers in 2D Ferromagnetic Shiba Lattices*, Phys. Rev. Lett. **114** (Jun, 2015) 236803. doi:10.1103/PhysRevLett.114.236803.

[100] Y. Kim, M. Cheng, B. Bauer, R. M. Lutchyn and S. Das Sarma, *Helical order in one-dimensional magnetic atom chains and possible emergence of Majorana bound states*, Phys. Rev. B **90** (Aug, 2014) 060401. doi:10.1103/PhysRevB.90.060401.

[101] H.-Y. Hui, J. D. Sau and S. Das Sarma, *Bulk disorder in the superconductor affects proximity-induced topological superconductivity*, Phys. Rev. B **92** (Nov, 2015) 174512. doi:10.1103/PhysRevB.92.174512.

[102] O. A. Awoga, K. Björnson and A. M. Black-Schaffer, *Disorder robustness and protection of Majorana bound states in ferromagnetic chains on conventional superconductors*, Phys. Rev. B **95** (May, 2017) 184511. doi:10.1103/PhysRevB.95.184511.

[103] E. Mascot, C. Agrahar, S. Rachel and D. K. Morr, *Stability of disordered topological superconducting phases in magnet-superconductor hybrid systems*, Phys. Rev. B **100** (Dec, 2019) 235102. doi:10.1103/PhysRevB.100.235102.

[104] Y. Lu, P. Virtanen and T. T. Heikkilä, *Effect of disorder on Majorana localization in topological superconductors: A quasiclassical approach*, Phys. Rev. B **102** (Dec, 2020) 224510. doi:10.1103/PhysRevB.102.224510.

[105] C. Christian, E. F. Dumitrescu and G. B. Halász, *Robustness of vortex-bound Majorana zero modes against correlated disorder*, Phys. Rev. B **104** (Jul, 2021) L020505. doi:10.1103/PhysRevB.104.L020505.

[106] A. Weststöm, K. Pöyhönen and T. Ojanen, *Topological superconductivity and anti-Shiba states in disordered chains of magnetic adatoms*, Phys. Rev. B **94** (Sep, 2016) 104519. doi:10.1103/PhysRevB.94.104519.

[107] G. H. S. Kuck, J. Wienhausen and R. Wiesendanger, *A versatile variable-temperature scanning tunneling microscope for molecular growth*, Rev. Sci. Instrum. **79** (2008) doi:10.1063/1.2972971.

[108] J. J. Goedecke, *Metalation and Polymerization of 5,5'-Dibromosalophene adsorbed on Au(111) and Co-intercalated Graphene.* Universität Hamburg, 2018.

[109] L. Cornils, *STM investigations of superconductor hybrid systems: magnetic adatoms and chains on superconductors to thin superconducting films on topological insulators.* Universität Hamburg, 2019.

[110] S. H. P. Chr. Wittnevena, R. Dombrowski and R. Wiesendanger, *A low-temperature ultrahigh-vacuum scanning tunneling microscope with rotatable magnetic field*, Rev. Sci. Instrum. **68** (1997) doi:10.1063/1.1148031.

[111] J. Wiebe, L. Zhou and R. Wiesendanger, *Atomic magnetism revealed by spin-resolved scanning tunnelling spectroscopy*, Journal of Physics D: Applied Physics **44** (nov, 2011) 464009. doi:10.1088/0022-3727/44/46/464009.

[112] N. Wiberg, *Lehrbuch der Anorganischen Chemie.* De Gruyter, 2008.

[113] M. Bahte, *Materialuntersuchungen an supraleitenden Niob-Proben mit Magnetisierungs- und Suszeptibilitätsmessungen.* Universität Hamburg, 1998.

[114] “MaTeck.” `https://mateck.com/index.php`. Accessed: 2022-05-23.

[115] A. B. Odobesko, S. Haldar, S. Wilfert, J. Hagen, J. Jung, N. Schmidt, P. Sessi, M. Vogt, S. Heinze and M. Bode, *Preparation and electronic properties of clean superconducting Nb(110) surfaces*, Phys. Rev. B **99** (Mar, 2019) 115437. doi:10.1103/PhysRevB.99.115437.

[116] C. Coupeau, J. Durinck, M. Drouet, B. Douat, J. Bonneville, J. Colin and J. Grilhé, *Atomic reconstruction of niobium (111) surfaces*, Surface Science **632** (2015) 60–63. doi:https://doi.org/10.1016/j.susc.2014.09.011.

[117] T. Haas, *A study of the niobium (110) surface using low energy electron diffraction techniques*, Surface Science **5** (1966), no. 3 345–358. doi:https://doi.org/10.1016/0039-6028(66)90033-1.

[118] A. S. Razinkin, E. V. Shalaeva and M. V. Kuznetsov, *Photoelectron spectroscopy and diffraction of NbOx/Nb(110) surface*, The Physics of Metals and Metallography **106** (2008) doi:10.1134/S0031918X08070089.

[119] I. Arfaoui, J. Cousty and C. Guillot, *A model of the NbO nanocrystals tiling a Nb(110) surface annealed in UHV*, Surface Science **557** (2004), no. 1 119–128. doi:https://doi.org/10.1016/j.susc.2004.03.025.

[120] J. J. Goedecke, M. Bazarnik and R. Wiesendanger, *Preparation and STM study of clean Nb(111) surfaces*, `arXiv:2302.04550[cond-mat.supr-con]`.

[121] J. J. Goedecke, L. Schneider, Y. Ma, K. T. That, D. Wang, J. Wiebe and R. Wiesendanger, *Correlation of Magnetism and Disordered Shiba Bands in Fe Monolayer Islands on Nb(110)*, ACS Nano **16** (2022), no. 9 14066–14074. doi:10.1021/acsnano.2c03965 [`arXiv:https://doi.org/10.1021/acsnano.2c03965`]. PMID: 36001503.

[122] Q. Ma, P. Ryan, J. W. Freeland and R. A. Rosenberg, *Thermal effect on the oxides on Nb(100) studied by synchrotron-radiation x-ray photoelectron spectroscopy*, Journal of Applied Physics **96** (2004), no. 12 7675–7680. doi:10.1063/1.1809774 [`arXiv:https://doi.org/10.1063/1.1809774`].

[123] K. Zhussupbekov, K. Walshe, K. Bozhko, A. Ionov, K. Fleischer, E. Norton, A. Zhussupbekova, V. Semenov, I. Shvets, B. Walls, *Oxidation of Nb(110): atomic structure of the NbO layer and its influence on further oxidation*, Scientific Reports **10** (2020) 3794. doi:https://doi.org/10.1038/s41598-020-60508-2.

[124] M. Delheusy, A. Stierle, N. Kasper, R. P. Kurta, A. Vlad, H. Dosch, C. Antoine, A. Resta, E. Lundgren and J. Andersen, *X-ray investigation of subsurface interstitial oxygen at Nb/oxide interfaces*, Applied Physics Letters **92** (2008), no. 10 101911. doi:10.1063/1.2889474 [`arXiv:https://doi.org/10.1063/1.2889474`].

[125] T. Madey, C.-H. Nien, K. Pelhos, J. Kolodziej, I. Abdelrehim and H.-S. Tao, *Faceting induced by ultrathin metal films: structure, electronic properties and reactivity*, Surface Science **438** (1999), no. 1 191–206. doi:https://doi.org/10.1016/S0039-6028(99)00570-1.

[126] C. Z. Dong, S. M. Shivaprasad, K. Song and T. E. Madey, *Platinum-induced morphology and reactivity changes on W(111)*, The Journal of Chemical Physics **99** (1993), no. 11 9172–9181. doi:10.1063/1.465532 [`arXiv:https://doi.org/10.1063/1.465532`].

[127] Bailar, J. C., Emeleus, H. J., Nyholm, R., Trotman-Dickenson, A. F., *Comprehensive Inorganic Chemistry.* Pergamon Press, 2009.

[128] F. Ullmann, *Ullmann's Encyclopedia of Industrial Chemistry.* Wiley-VCH Verlag, 2000.

[129] R. Becker, *Gmelin Handbuch der Anorganischen Chemie.* Springer Berlin, Heidelberg, 1978.

[130] X. Yang, W. Hu and X. Yuan, *Melting mechanisms of Nb(111) plane with molecular dynamics simulations*, Physics Letters A **365** (2007), no. 1 161–165. doi:https://doi.org/10.1016/j.physleta.2006.12.068.

[131] A. Mougin, S. Andrieu, C. Dufour and K. Dumesnil, *Epitaxial growth of Fe on Nb(110)*, Surface Science **518** (2002), no. 3 175–182. doi:https://doi.org/10.1016/S0039-6028(02)02084-8.

[132] C. Wolf, *Initial Growth and Interdiffusion of Nb/Fe(110) and Fe/Nb(110) studied by Scanning Tunnelling Microscopy.* PhD thesis, Ruhr-Universität Bochum, 2006.

[133] C. Wolf and U. Köhler, *Intermixing at the interface of the system Nb/Fe(110) investigated by STM*, Surface Science **523** (2003), no. 3 L59–L64. doi:https://doi.org/10.1016/S0039-6028(02)02461-5.

[134] C. Wolf and U. Köhler, *Growth and intermixing of Nb on Fe(110) and Fe on Nb(110)*, Thin Solid Films **500** (2006), no. 1 347–355. doi:https://doi.org/10.1016/j.tsf.2005.11.039.

[135] U. Köhler, C. Jensen, C. Wolf, A. Schindler, L. Brendel and D. Wolf, *Investigation of homoepitaxial growth on bcc surfaces with STM and kinetic Monte Carlo simulation*, Surface Science **454-456** (2000) 676–680. doi:https://doi.org/10.1016/S0039-6028(00)00151-5.

[136] L. Zhou, F. Meier, J. Wiebe and R. Wiesendanger, *Inversion of spin polarization above individual magnetic adatoms*, Phys. Rev. B **82** (Jul, 2010) 012409. doi:10.1103/PhysRevB.82.012409.

[137] M. Bode, M. Heide, K. von Bergmann, P. Ferriani, S. Heinze, G. Bihlmayer, A. Kubetzka, O. Pietzsch, S. Blügel and R. Wiesendanger, *Chiral magnetic order at surfaces driven by inversion asymmetry*, Nature **447** (2007), no. 7141 190–193.

[138] K. Doi, E. Minamitani, S. Yamamoto, R. Arafune, Y. Yoshida, S. Watanabe and Y. Hasegawa, *Electronic and magnetic effects of a stacking fault in cobalt nanoscale islands on the Ag(111) surface*, Phys. Rev. B **92** (Aug, 2015) 064421. doi:10.1103/PhysRevB.92.064421.

[139] J. Hagemeister, D. Iaia, E. Y. Vedmedenko, K. von Bergmann, A. Kubetzka and R. Wiesendanger, *Skyrmions at the Edge: Confinement Effects in Fe/Ir(111)*, Phys. Rev. Lett. **117** (2016) 207202.

[140] J. Hagemeister, "MONTECRYSTAL."
`https://github.com/JHagemeister/MonteCrystal`, accessed 2020-01-12.

[141] J. Röntynen and T. Ojanen, *Topological Superconductivity and High Chern Numbers in 2D Ferromagnetic Shiba Lattices*, Phys. Rev. Lett. **114** (Jun, 2015) 236803. doi:10.1103/PhysRevLett.114.236803.

[142] L. Schneider, M. Steinbrecher, L. Rózsa, J. Bouaziz, K. Palotás, M. dos Santos Dias, S. Lounis, J. Wiebe and R. Wiesendanger, *Magnetism and in-gap states of 3d transition metal atoms on superconducting Re*, npj Quantum Materials **4** (2019), no. 1 42.

[143] F. Küster, A. M. Montero, F. S. M. Guimarães, S. Brinker, S. Lounis, S. S. P. Parkin and P. Sessi, *Correlating Josephson supercurrents and Shiba states in quantum spins unconventionally coupled to superconductors*, Nature Communications **12** (2021), no. 1 1108.

[144] L. Mougel, P. M. Buhl, Q. Li, A. Müller, H.-H. Yang, M. Verstraete, P. Simon, B. Dupé and W. Wulfhekel, *The role of band matching in the proximity effect between a superconductor and a normal metal*, arXiv:2203.01393 (2022) [`arXiv:2203.01393[cond-mat.mes-hall]`].

[145] T. Mayer-Kuckuk, *Atomphysik.* Teubner, Stuttgart, 1985.

[146] H. W. H. Haken, *Atom- und Quantenphysik*, p. 355. Springer Berlin Heidelberg, Berlin, Heidelberg, 1993.

[147] F. Hund, *Zur Deutung der Molekelspektren. I*, Zeitschrift für Physik **40** (Sept, 1927) 742–764. doi:10.1007/BF01400234.

[148] F. Hund, *Zur Deutung der Molekelspektren. II*, Zeitschrift für Physik **42** (Feb, 1927) 93–120. doi:10.1007/BF01397124.

[149] K. von Klitzing, *The quantized Hall effect*, Rev. Mod. Phys. **58** (Jul, 1986) 519–531. doi:10.1103/RevModPhys.58.519.

[150] M. Nakahara, *Differentialgeometrie, Topologie und Physik.* Springer, Berlin, Heidelberg, 2015.

[151] I. Horcas, R. Fernández, J. Gomez-Rodriguez, J. Colchero, J. Gómez-Herrero and A. Baro, *WSXM: A software for scanning probe microscopy and a tool for nanotechnology*, Review of scientific instruments **78** (2007), no. 1 013705.

[152] R. N. Bracewell, *The Fourier transform and its applications.* McGraw Hill Higher Education, 1986.

[153] Q. Peter, L. G. D. Pietro and D. A. Zanin, *MATLAB Library for Nanonis based files: NanoLib*, Jan., 2017.

List of Publications

Articles

Preparation and STM study of clean Nb(111) surfaces
J. J. Goedecke, M. Bazarnik and R. Wiesendanger
arXiv [cond-mat.supr-con] **2302.04550** , (2023).

Correlation of magnetism and disordered Shiba bands in Fe monolayer islands on Nb(110)
J. J. Goedecke, L. Schneider, Y. Ma, K. Ton That, D. Wang, J. Wiebe and R. Wiesendanger
ACS Nano **16**, 14066 (2022).

In Situ Synthesis of Metal–Salophene Complexes on Intercalated Graphene
M. Elsebach, E. Sierda, J. Goedecke, L. Bignardi, M. Hermanowicz, M. Rohde, R. Wiesendanger and M. Bazarnik
J. Phys. Chem. C **124**, 4279 (2020).

Contributed talks

Metalation and Polymerization of 5,5'-Dibromosalophene on Co-intercalated Graphene
J. Goedecke, M. Elsebach, M. Rohde, E. Sierda, M. Bazarnik, and R. Wiesendanger
DPG Spring meeting, Regensburg, 2019.

Posters

Electronic structure of porphyrin-nanographene on Au(111) by STM/STS
J. Goedecke, M. Elsebach, A. Narita, K. Müllen, C. Qiang, M. Bazarnik and R. Wiesendanger
8th International Conference on Scanning Probe Spectroscopy, Hamburg 2019

Danksagung

Als erstes möchte ich mich herzlich bei Prof. Wiesendanger bedanken. Vielen Dank, dass Sie es mir ermöglicht haben, meine Doktorarbeit in Ihrer Gruppe zu schreiben, und dass Sie mich zu dem spannenden Thema der Majorana- und Shiba-Physik geführt haben. Darüber hinaus haben Sie mich während meiner gesamten Doktorarbeit begleitet und mich auch in schwierigen Phasen unterstützt und motiviert.
Mein besonderer Dank geht an Dr. habil. Jens Wiebe. Danke, Jens, für deine Betreuung und Unterstützung, die für mich sehr wichtig war, besonders in der letzten Phase meiner Arbeit. Außerdem war deine Tür immer offen für mich und unsere Diskussionen haben mir sehr geholfen meine Verwirrungen zu entwirren.
Darüber hinaus möchte ich mich bei Dr. Maciej Bazarnik bedanken, der mich in der ersten Phase meiner Promotion in das Labor 014 eingeführt hat und mir stets mit technischer Unterstützung zur Seite stand.

Von besonderem Wert war für mich der Austausch und die Unterstützung meiner Kollegen und Freunde. Daher ein großes Dankeschön an Jonas Spethmann, Lucas Schneider, Khai Thât-Tôn, Phillip Beck und alle anderen in der Gruppe. Außerdem möchte ich mich bei meinem guten Freund Andrey Saveliev bedanken, der meine Arbeit auf Rechtschreibung korrigiert hat, danke Dru!
Die Arbeit wäre außerdem ohne den technischen Support nicht möglich gewesen, daher gilt mein Dank dem Helium-Team und der mechanischen Werkstatt!

In meinem Privatleben hat mich meine Familie unterstützt, daher möchte ich diese Gelegenheit nutzen, um mich bei meinen Eltern zu bedanken. Bei meinem Vater, der immer an mich geglaubt hat und der als studierter Physiker natürlich unglaublich interessiert daran war, was ich im Labor gemacht habe, und bei meiner liebevollen Mutter, die mich immer unterstützt hat. Darüber hinaus möchte ich auch meiner lieben Schwiegermutter Christel Goedecke und meinen Geschwistern Mario Weber und Kannika Inala für die Unterstützung danken.

Schließlich möchte ich einem ganz besonderen Menschen in meinem Leben danken – meinem Ehemann Yasar Goedecke. Danke, dass du mich immer unterstützt und an mich glaubst.

Eidesstattliche Erklärung

Hiermit versichere ich an Eides statt, die vorliegende Dissertationsschrift selbst verfasst und keine anderen als die angegebenen Hilfsmittel und Quellen benutzt zu haben. Die Dissertation wurde in der vorgelegten oder einer ähnlichen Form nicht schon einmal in einem früheren Promotionsverfahren angenommen oder als ungenügend beurteilt.

Hamburg, den 09.05.2023

Julia Jirapon Goedecke